

Optical Spectroscopy of Mn-doped Perovskite Nanocrystals

ISBN: 978-94-6380-193-5

Printed by: ProefschriftMaken || www.proefschriftmaken.nl

Optical Spectroscopy of Mn-doped Perovskite Nanocrystals

Optische spectroscopie van Mn-gedoteerde perovskiet
nanokristallen

(met een samenvatting in het Nederlands)

Proefschrift

ter verkrijging van de graad van doctor aan de Universiteit Utrecht op gezag
van de rector magnificus, prof.dr. H.R.B.M. Kummeling, ingevolge het
besluit van het college voor promoties in het openbaar te verdedigen op
woensdag 16 januari 2019 des ochtends te 10.30 uur

door

Kunyuan Xu

geboren op 9 November 1990 te Liaoning, China

Promotor:

Prof. dr. A. Meijerink

This work presented in this thesis was supported by China Scholarship Council-Utrecht University PhD Program (Program: 201404910557).

Table of Contents

1. Introduction	1
2. Facile One-Pot Synthesis of CsPbX₃ (X=Cl, Br, I) Perovskite Nanocrystals	31
3. Efficient and Stable Luminescence from Mn²⁺ in Core and Core-Isocrystalline Shell CsPbCl₃ Perovskite Nanocrystals	45
4. Tuning Exciton-Mn²⁺ Energy Transfer in Mixed Halide Perovskite Nanocrystals	69
5. Long-lived Dark Exciton Emission in Mn-doped CsPbCl₃ Perovskite Nanocrystals	93
6. Summary	109
Samenvatting in het Nederlands	117
List of Publications	125
Acknowledgement	126
About the Author	127

Chapter 1

Introduction

1.1 Introduction

The rapid development of nanotechnology has a great impact on our society. Nanomaterials are at the basis of nanotechnology. The fabrication of nanomaterials is enabled by an ever-increasing control over the design, creation and characterization of materials, even down to the atomic level. This was predicted by Richard Feynman in his visionary lecture of 1959 where he said “There’s plenty of room at the bottom, the principles of physics, as far as I can see, do not speak against the possibility of maneuvering things atom by atom, put the atoms down where the chemist says, and so you make the substance”. Since then fascinating properties originating from nanomaterials have been discovered and have resulted in breakthrough technologies. The research presented in this thesis focuses on the perovskite semiconductor nanomaterials. This is new class of materials that has emerged recently and has generated substantial excitement owing to their promising properties and performance.

1.1.1 Size-dependent Optical Properties of Quantum Dots (QDs)

Semiconductor nanocrystals (NCs) also known as quantum dots (QDs), are inorganic nanomaterials which exhibit unique size-tunable optical and electrical properties due to confinement of the exciton¹⁻³. The width of the bandgap of semiconductor nanocrystals is no longer a fixed gap determined by the chemical composition and crystal structure of a material but instead has become tunable by changing parameters, such as size and shape^{2,4,5}. The progressive reduction of size of QDs results in continuously increasing of the band gap because of quantum confinement. This leads to a blue shift of absorption and emission and is illustrated in Figure 1.1.

For a spherical QD of radius R the lowest exciton energy is determined by the fundamental band gap of bulk material and confinement energy of electrons and hole (E_{1s}^e, E_{1s}^h) and Coulomb interaction (J_{e-h}):

$$E_g^{NC} = E_g^0 + E_{1s}^e + E_{1s}^h - J_{e-h} = E_g^0 + \frac{\hbar^2 \chi_{nl}^2}{2m_e^* R^2} + \frac{\hbar^2 \chi_{nl}^2}{2m_h^* R^2} - 1.79 \frac{e^2}{4\pi\epsilon\epsilon_0 R} \quad (1.1)$$

The above equation for the bandgap of quantum dots (E_g^{NC}) reflects the combined effects of the periodical potential of the lattice, the Coulomb interaction of the electron-hole pair (J_{e-h}) and quantum confinement effects (E_{1s}^e for the electron and E_{1s}^h for the hole)².

Chapter 1

The periodical potential is caused by the regular arrangement of atoms in the semiconductor and gives the semiconductor properties such as the bandgap (E_g^0 for the bulk semiconductor). To model the behavior electrons (holes) under the influence of the periodical potential, an effective mass of the electrons (m_e^*) and holes (m_h^*) is introduced that is often smaller than the rest mass of an electron. The widening of the bandgap by confinement of the electron and hole depends on the effective masses and the size R of the quantum dot. The energies of discrete levels for the electron and hole in QDs are further determined by the root of the Bessel functions χ_{nl} where n and l are the quantum numbers describing the wave functions, with the 1S ($n=1, l=0$) being the lowest energy state.

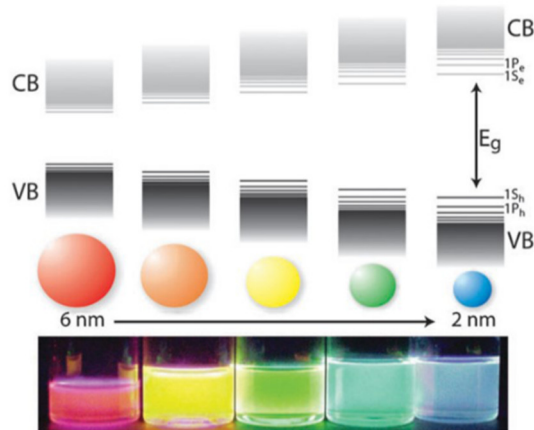


Figure 1.1 Size dependent band structure of QDs and blue shift of QD emission with the decreasing QD size (Adapted from Ref. 1 with permission)

In a semiconductor, under excitation by light, photons can be absorbed of energies equal to or higher than the bandgap. Absorption of a photon promotes one of the electrons from the filled valence band to the empty conduction band and leaves a quasi-particle, i.e. a hole behind. The combination of electron and hole, attracted through by Coulomb interaction, forms an exciton. The annihilation of an exciton is accompanied by emission of photon with an energy equal or slightly lower than the band gap. This phenomenon is known as luminescence.

Chapter 1

In a QD the excited electron and hole are confined which leads to a widening of the energy gap (as shown in Eq. 1.1) and thus a blue shift of the emission and absorption onset. Quantum confinement is the origin of size dependent properties of QDs and can be observed when the size of semiconductor is comparable to or smaller than the characteristic Bohr radius of the exciton in the bulk semiconductor. The exciton Bohr radius varies for different semiconductors and typically ranges from 1 to 50 nm⁴. In the strong confinement regime, where the size of the crystal is smaller than the Bohr radius of both electron and hole, the quantum confinement is most prominent and dominates over the Coulomb interaction. In this regime, the motion of electron and hole can be treated separately and both exhibit a discrete atomic-like energy level structure with 1S, 1P, 1D, 2S, 2P etc. energy levels. The Coulomb interaction is considered as a perturbation (this is the case that Equation 1.1 described).

The motion of the electron and hole in the weak confinement regime (size of crystal ~2 times the Bohr radius) differs from the strong confinement regime. The electron and hole are strongly coupled through Coulomb interaction and move as a unit (exciton). It also has discrete energy levels under the influence of quantum confinement. In the regime in between, the motion of electrons and holes are determined by the interplay of quantum confinement and Coulomb interaction.

1.1.2 Evolution of Energy States from Molecules to QDs

The description of quantum confinement effects and energy level structure of QDs presented above is known as the top-down approach, starting from the band structure of bulk semiconductors and including confinement effects as perturbations. An alternative model to explain the unique size-dependent properties of QDs describes the evolution of the energy level structure by considering linear combinations of atomic orbitals (LCAO). This is known as the bottom-up approach¹. When isolated atoms are brought into close proximity to form a cluster, a set of molecular orbitals is formed on the basis of atomic orbitals of constituent atoms. Half of the molecular orbitals are lower-energy bonding orbitals, which are preferably filled with electrons before the higher-energy anti-bonding orbitals are filled. When the cluster is small, discrete molecular orbitals with well-defined energies are separated by energy gaps. In molecular orbital theory, the highest occupied molecular orbitals are referred to as HOMO and the lowest unoccupied molecular orbitals

Chapter 1

are called LUMO. The energy separation between HOMO and LUMO is the HOMO-LUMO gap. When an increasing number of atoms are brought together to form a larger cluster, the number of molecular orbitals increases further, which reduces the HOMO-LUMO gap. QDs form the transition between large molecular clusters and bulk semiconductors. In molecular clusters, there are discrete energy HOMO and LUMO levels while in bulk semiconductors there is a continuum of closely spaced energy levels in the valence band (VB) and conduction band (CB). In the intermediate size regime of QDs there is a near continuum of states in the middle of the VB and CB but discrete states emerge at the band edges where the density of states (DOS) in the bulk material is low. The states are labelled by quantum numbers n and l as outlined above, giving rise to $1S_h, 1P_h, 1D_h, 2S_h$ etc. levels at the top of the valence band and $1S_e, 1P_e, 1D_e, 2S_e$ etc. levels at the bottom of the conduction band. These two energy bands are separated by an energy gap called band gap.

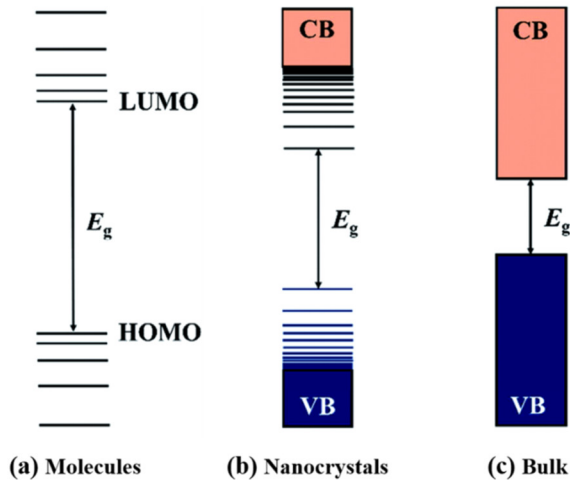


Figure 1.2 Bottom up approach to explain the energy level structure and band gap evolution of QDs with size. The energy level structure of QDs forms a transition between localized discrete energy levels in molecules and a continuum of delocalized states in the bulk (Reproduced from Ref. 3 with permission)

Chapter 1

The bottom up approach provides a clear physical image on how the band gap evolves with the number of the atoms (size) and explains the transition from discrete energy states at smaller sizes to a continuum of energy closely spaced energy levels in bulk material. Figure 1.2 schematically illustrates the evolution of DOS with the change of the number of the constituent atoms.

In the discussion above, only the case of small spherical nanocrystals has been considered. However, not only the size but also shape has a prominent role in the energy level structure and the DOS^{5,6}. By reducing size in certain dimensions, quantum confinement can be achieved in one-, two- or all three dimensions, as schematically shown in Figure 1.3. In a bulk solid the DOS is high and forms a continuous band of energy levels with a DOS that is proportional to $E^{1/2}$ at the band edges. For the situation that the exciton is confined in one direction only (2D nanoplatelet) the DOS follows a staircase like function. With the transition from to a 1D nanowire there is a switch from a step-like DOS to an $E^{1/2}$ dependent DOS. Finally, for 0D QDs, the exciton is subjected to three-dimensional confinement and characterized discrete states in the DOS which is the origin of the fascinating size dependent optical and electrical properties of QDs. The evolution of DOS as a function of dimensionality is illustrated in the Figure 1.3.

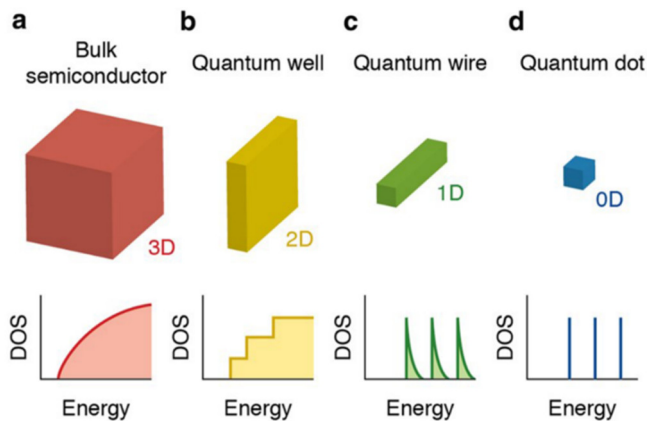


Figure 1.3. Evolution of DOS upon the changing of dimensionality of confinement in semiconductors from 3D to 0D (Reproduced with permission from Ref. 5).

1.1.3 Surface Chemistry of QDs

Due to the large surface to volume ratio in nanocrystals, the surface associated electronic states (surface states) have a strong influence on the properties (e.g. catalytic, electronic and optical) of QDs⁷⁻¹⁰. Therefore, surface engineering of QDs is of fundamental importance for their application. In the present context the impact of surface chemistry on the luminescence properties of QDs is relevant. The large surface to volume ratio of QDs leads to a large fraction of ions residing on the surface. For those surface ions, the lack of neighboring ions leads to unsaturated bonds, which are commonly known as dangling bonds. Ideally, the dangling bonds are passivated by capping molecules. The presence of dangling bonds can give rise to trapping of an electron or hole at the surface. The spatial separation of surface trapped electron (hole) from the remaining delocalized hole (electron) in the QD can result in trap emission or non-radiative recombination and thus decrease the emission intensity¹¹. Radiative recombination of the trapped charge carrier gives rise to broad trap state emission bands, which can be dominant over the narrow band-edge emission in QDs with poor surface passivation.

Commonly ligands which serve for surface passivation are simultaneously involved in the growth process in the colloidal synthesis approach. In a typical colloidal synthesis, the nucleation and growth of QDs is regulated with organic passivation ligands (surfactants) which can bind to the surface and in this manner control the addition of new units to the growing NCs. Stronger binding ligands or lower reaction temperatures will lead to slower growth and thus smaller QDs. In addition, the ligands play a crucial role in allowing for stable dispersions of QDs in a solvent of similar polarity as the ligands. They offer structural integrity and contribute to high photoluminescence quantum yields of QDs through passivation of surface states and removing all surface states energetically from the forbidden gap.

Despite the attractiveness of organic ligand for passivating QDs, the long organic tail also has disadvantages. It hampers inter-particle charge transport, which seriously hinders application of QDs in devices where a high conductivity is required, e.g. in solar cells^{12,13}. Effective surface passivation can also be achieved by inorganic surfactants which helps to overcome the inefficient charge-transport. The organic capping ligand can be replaced by a large variety of inorganic capping ligands e.g. metal chalcogenide complexes (MCCs)¹³,

Chapter 1

(S^{2-} , HS^- , Se^{2-} , SCN^-)¹⁴⁻¹⁸, halides¹⁹⁻²¹ and perovskite^{12, 22, 23}. All these ligands have been successfully applied to replace long-chain organic ligands on NCs, while preserving the NCs' morphological feature, size dispersity and PL QY. The application of halide ligands is most relevant to this thesis and will therefore be introduced. Lead chalcogenide NCs (PbS, PbSe) are promising for developing new solar cells, IR photon-detectors and lasers. However, the commonly synthesized organic ligand capped PbS/PbSe NCs are oxygen sensitive which limits their application. It was demonstrated by Pietryga *et al.* that chloride passivation can substantially enhance the oxygen stability of PbSe QDs²⁰. The lead chloride passivated PbSe were obtained by using Cl_2 to selectively etch away surface Se ion and form a thin $PbCl_2$ passivation layer. The resulting Pb-Cl terminated PbSe NCs show not only higher resistance towards oxidation but also have an increased photoluminescence quantum yield (PL QY). The enhanced PL QY further confirms the beneficial effect of halide passivation, which can be ascribed to the reduction of the number of surface traps after halide passivation. Similarly, an in situ halide passivation approach has been developed for PbS and PbSe by using $PbCl_2$ instead of PbO as lead precursor²¹. A halide passivated surface is formed during the synthesis. An illustration is shown in Figure 1.4.

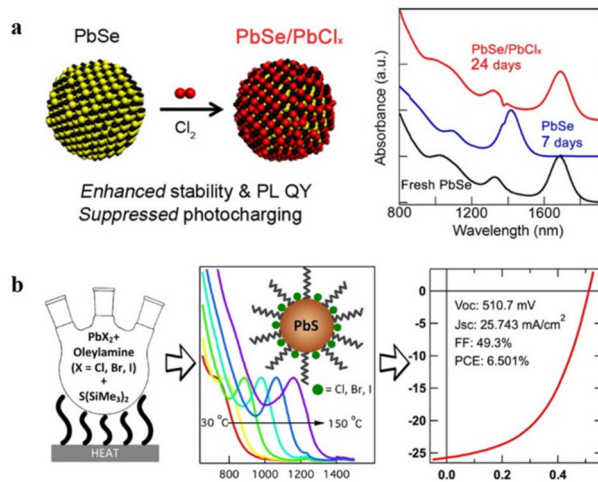


Figure 1.4. Illustration of halide passivation of PbS and PbSe QDs (adapted from Refs. 20, 21 with permission)

1.2 Perovskite Nanocrystals

Lead halide perovskite nanocrystals (NCs) have recently emerged as a promising class of materials for various optoelectronic applications (LEDs, lasers, solar cells, photon detectors)²⁴⁻²⁹. Their large compositional flexibility, defect tolerant energy band structure and versatile solution processibility create possibilities to achieve brighter LEDs, more efficient solar cell and low threshold lasers. All these applications rely on the in-depth understanding of the structure-property relationship, material synthesis and device design. The following discussion will mostly focus on the synthesis of the nanocrystals with an emphasis on further functionalization through manganese doping.

1.2.1 Crystal Structure of Perovskites.

Halide perovskites form an extended family of compounds^{30,31}. They can all be described by a general formula of ABX_3 , where “A” is large monovalent cation that can be either organic (e.g. MA: methylammonium, FA: formamidinium) or inorganic (e.g. Cs^+ , K^+), “B” is divalent metal cation usually from group IV (e.g. lead, tin), and “X” is a halide anion ($X=Cl, Br, I$). For bulk perovskites, neighboring $[BX_6]$ octahedra are corner shared and connected to form an infinite 3D network with “A” residing in a 12-coordinated cavity formed by eight $[BX_6]$ octahedra. “A” functions as a structure template and plays a critical role in determining the stability of the perovskite structure. The perovskite structure can also be viewed as a cubic close packing of the large cations “A” and anions “X” with smaller cations “B” occupying octahedral cavities.

The discovery of $CsPbX_3$ ($X=Cl, Br, I$) perovskites by Moller dates back to 1958^{33,34}. Their structural and tunable photoconductive properties through varying the halide composition were investigated later. The stability of $CsPbX_3$ in the perovskite crystal structure can be predicted by a geometric criterion, the tolerance factor t , which predicts the likelihood of the combination of cations and anion to form the perovskite structure. It is proposed that to form an ideal cubic perovskite structure, the ionic radii of cations and anion must satisfy the following relation (Goldschmidt’s rule):

$$0.8 \leq t = \frac{(r_A+r_X)}{\sqrt{2}(r_B+r_X)} \leq 1 \quad (1.2)$$

where r_A , r_B and r_X are the respective ionic radii of the ions in the ABX_3 formula and t is

Chapter 1

the tolerance factor. In case of CsPbX_3 ($X=\text{Cl, Br, I}$), the rule indicates that all three halide ions are capable of forming the perovskite structure. However, the large size of iodide makes the perovskite structure hard to sustain and non-perovskite structures can frequently be found with iodide-based compounds (e. g. an orthorhombic phase with edge sharing of $[\text{PbI}_6]$, known as the “yellow phase”).

Due to the high flexibility of the B-X-B bond, the ideal cubic perovskite structure can be easily distorted when subjected to internal or external stimuli (e.g. pressure, temperature, etc.) and orthorhombic or tetragonal phases can form (see Figure 1.5). An internal stimulus can be changing the size of “A” position ions, which will affect the structural stability by steric and Coulombic interactions. A higher degree of $[\text{BX}_6]$ distortion affects the interaction between neighboring Pb-ions and reduces the character of p-orbital of Pb to the conduction band (vide infra), leading to a lower degree of spin-orbit splitting. As a result, the band gap is increased. In response to external stimuli, such as the temperature, the $[\text{BX}_6]$ octahedron can tilt and this results in a series of lower symmetry phases of distorted perovskites. For instance, with decreasing temperature, the cubic phase can transform to a tetragonal phase and subsequently an orthorhombic phase at well-defined and material-specific temperatures. Upon tilting of the octahedron the perovskites retain their basic 3D architecture but it strongly modifies the energy band structure and consequently optical and electronic properties. Also surface effects play a dominant role in determining the equilibrium phase when the size of the crystallites is smaller than 100 nm. For example, the orthorhombic phase for CsPbI_3 can be obtained at lower temperature ($< 200\text{ }^\circ\text{C}$) and remains in its orthorhombic phase at room temperature. This is ascribed to the large surface energy which contributes to enhance the stability of the orthorhombic phase.³⁵ Although a general acceptance on basic assignments of perovskite NCs’ phase is reached, further research is needed on the role of the large surface to volume ratio and the presence of defects in NCs on the relative phase stability^{25,36}.

1.2.2 Optical Properties CsPbX_3 ($X= \text{Cl, Br and I}$) NCs

Early research on CsPbX_3 bulk crystals provided insight in the band structure of this semiconductor which forms the basis for the optical properties of the CsPbX_3 NCs. The first optical absorption and luminescence studies on CsPbCl_3 and CsPbBr_3 date back to the 1970s^{37,38}. For CsPbBr_3 an absorption onset was measured at 2.4 eV (around 520 nm) and

Chapter 1

for CsPbCl₃ around 3 eV (around 415 nm). Band structure calculations were done to provide insight in the conduction and valence band states. Based on an LCAO model a good agreement between the calculated and experimental bandgap was obtained. The valence band is formed by the filled halogen p orbitals (3p for Cl⁻ and 4p for Br⁻) and the filled 6s orbital of Pb²⁺. The conduction band arises from the interaction between 6p orbitals of Pb²⁺ in the simple cubic lead-sublattice. The semiconductor is a direct bandgap material with a direct transition at the R-point in the Brillouin zone.

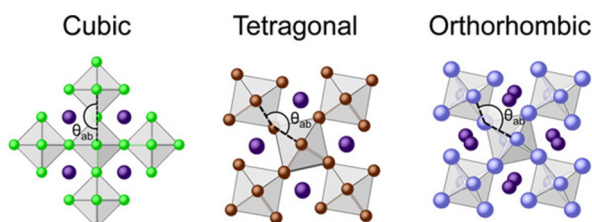


Figure 1.5 Different 3D polymorphs of CsPbBr₃ (Adapted from Ref. 36 with permission)

The first observation of quantum confinement effects predates the recent excitement concerning the optical and electrical properties of perovskite NCs by almost two decades. Already in 1995 quantum confinement effects in the optical properties (luminescence and absorption) were reported for NCs of CsPbCl₃ that form upon doping CsCl with Pb²⁺ ³⁹⁻⁴¹. The position of the excitonic absorption peak was shown to shift to higher energies (shorter wavelengths, from ~415 nm to 405 nm) for smaller CsPbCl₃ NCs in the CsCl matrix. The size was controlled through the annealing procedure. The exciton emission was shown to be efficient with a short sub-ns life time at cryogenic temperatures.

A strong increase in research on the luminescence of CsPbX₃ NCs was triggered by a pioneering publication of Kovalenko et al ³⁵. A new colloidal synthesis method (vide infra) was reported yielding highly luminescent CsPbX₃ NCs. The emission color is tunable over the full spectral region by varying the chemical composition through anion exchange. Exchange of Cl⁻ by Br⁻ in CsPbCl_{1-x}Br_x shifts the emission from the violet to the green spectral region and subsequent anion exchange of Br⁻ by I⁻ in CsPbBr_{1-x}I_x can shift the

emission to the deep red region. Quantum yields exceeding 90% have been realized. This makes these NCs highly promising for opto-electronic applications. Variation of the emission color in the perovskite NCs is not realized via size variation as is common for the II-VI (e.g. CdSe) and III-V (e.g. InP) QDs. The size of the perovskite NCs is typically around 10 nm and is similar to or larger than that of the exciton Bohr radius in these materials (varying from 2.5 nm in CsPbCl₃ to 6 nm in CsPbI₃). The synthesis of smaller CsPbX₃ NCs is challenging and thus color tuning through variation of the chemical composition is favored over tuning by size variation.

The life time of the exciton emission is short, in the ns range at room temperature. This is about an order of magnitude faster than the 10-30 ns for CdSe and CdTe QDs. For application in high brightness light sources this shorter life time can be advantageous. Upon cooling to cryogenic temperatures even faster, sub-ns, life times are observed. This has been explained by inverted dark-bright state splitting. Typically, in QDs the lowest energy exciton state has a spin-forbidden transition to the ground state and population of the lowest exciton state (known as ‘dark’ state) gives rise to a lengthening of the exciton emission life time below 50 K. In this thesis we will address the apparent dark-bright state inversion in CsPbX₃ NCs in **Chapter 5**.

1.2.3 Synthesis of Perovskite NCs

The formation of nanocrystals during a colloidal synthesis often involves two phases separated in time which are associated with a nucleation and a growth process. These processes can be adequately modeled by the La Mer mechanism⁴². In the La Mer mechanism, a fast accumulation of monomers in the reaction medium is the prerequisite for nucleation to take place. Once the critical concentration of monomers is reached, the nucleation is initiated. During this period, only the crystallites larger than the critical size are stable and these will serve as seeds for further crystal growth. The critical size is determined by thermodynamics and can be calculated by equation 1.3⁴².

$$r_{crit} = \frac{-2\gamma}{\Delta G_v} = \frac{2\gamma v}{k_B T \ln S} \quad (1.3)$$

where γ is surface tension and ΔG_v is the Gibbs free energy for the bulk crystal. The ΔG_v can be related to the solution’s over-saturation S , the molar volume of the crystallite v and temperature T (k_B is Boltzmann constant).

Chapter 1

Following a burst of nucleation the oversaturation is reduced and shifts the reaction conditions towards growth of the seed crystals. To achieve a uniform size distributing, it is key to separate the nucleation and growth in time. The renowned paper published by Bawendi *et al.* in 1993 introduced a hot-injection method which provided a reliable synthesis method for a wide variety of colloidal nanocrystals⁴³. In that protocol, nucleation is initiated by injection of reactive precursors and is separated in time from the subsequent NCs' growth. The method allows remarkable size control for a wide range of sizes through variations in concentration, types of ligand, injection temperature and growth duration.

The pioneering work by the Kovalenko group in 2015 resulted in preparation of colloidal CsPbX₃ (X=Cl, Br, I) nanocrystals by a hot-injection method³⁵. In a typical synthesis, lead halide is dissolved in a high boiling solvent, i.e. octadecene, with surface ligands, i.e. oleic acid and oleylamine, at elevated temperature (150~200 °C). The strong interaction of the lead cation and oleate anion results a stable complex. In a separate flask, cesium carbonate is heated in octadecene with oleic acid, which eventually results in cesiumoleate dissolved in octadecene. The swift injection of the cesium precursor into the lead halide precursor solution leads to a burst nucleation of CsPbX₃ (X=Cl, Br, I) nanocrystals. The reaction is quenched after a few seconds by rapid cooling using an ice bath. Nearly monodisperse CsPbX₃ (X=Cl, Br, I) nanocubes can be precipitated out of crude solution by centrifuging. The size of nanocrystals is mainly determined by the ligand concentration and can be slightly modified by the synthesis temperature.

Besides the hot-injection method requiring two separate precursors as previously mentioned, a non-injection method (one-pot synthesis) with all precursors in one flask has also been used to yield high quality CsPbX₃ (X=Cl, Br, I) nanocrystals. The successful application of a one-pot synthesis provides a promising strategy to scale up the synthesis of CsPbX₃ (X=Cl, Br, I) nanocrystals⁴⁴⁻⁴⁶. Several other synthesis approaches have been employed for the preparation of highly luminescent CsPbX₃ nanocrystals. For example, the ligand assisted reprecipitation method (LARP) at room temperature under ambient conditions, whereby a rapid injection of CsPbX₃ (i.e. CsX, PbX₂, X=Cl, Br, I) precursors in a good solvent such as DMF or DMSO, into a poor solvent e. g. toluene or chloroform is done in the presence of coordinating ligands. The room temperature LARP method is promising for scaling up production without sacrificing optical properties of nanocrystals⁴⁷⁻⁴⁹. An ultrasonication method has also been proven successful for the synthesis of high quality CsPbX₃ NCs⁵⁰.

Chapter 1

Various sizes of perovskite NCs (even down to 2.5 nm) have been realized by using porous silica as a template. The size can be controlled by the template, providing a practical method to study stronger quantum confinement effects in perovskite NCs^{51, 52}.

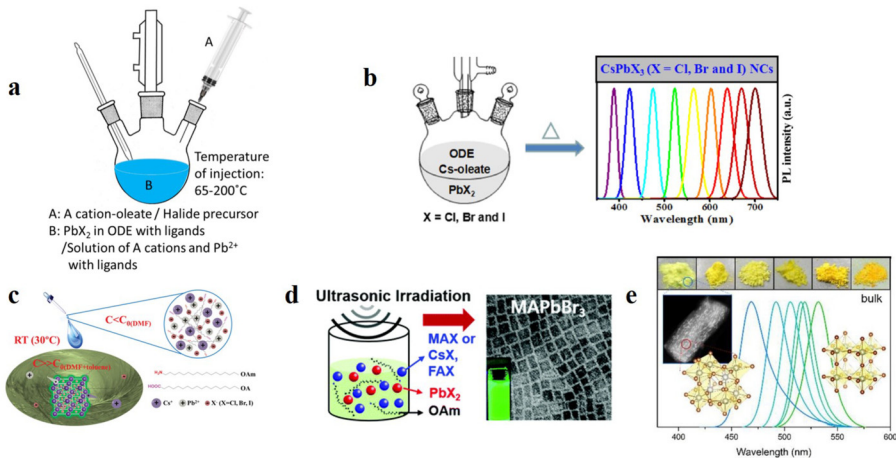


Figure 1.6. Illustration of different synthesis methods of CsPbX₃ NCs (a) hot-injection method. (b) one-pot synthesis method (c) ligand assisted precipitation method (d) ultrasonication method (e) meso-porous silica template method (adapted from Refs. 53, 46, 47, 50, 52 with permission)

1.3 Synthesis of Doped Perovskite NCs

During the past decades, doping of II-VI semiconductors has been an area of extensive study. Doping QDs with luminescent ions allows further control over the optical properties and has opened new routes to further extend the application of luminescent nanocrystals⁵⁴⁻⁵⁶. Excitation in the strong and broad absorption band of the QD is followed by energy transfer (ET) to the luminescent dopant ion inside the QD and characteristic emission from the dopant is observed. Transition metal doped QDs, for instance Cu⁺ and Mn²⁺ doped ZnSe or ZnS, broaden the achievable spectral range for luminescence. The fact that these QDs do not contain toxic heavy metals such as Cd or Pb make these doped QDs promising as green

Chapter 1

alternatives for lighting applications^{56,57}. Furthermore, the emission of the dopant is shifted to longer wavelengths and is not resonant with the strong exciton absorption. This is important in luminescent solar concentrators. Reabsorption poses a problem for traditional (undoped) QDs where exciton emission is resonant with the strong exciton absorption and repeated reabsorption results in a strong decrease of efficiency⁵⁸.

The possibility of doping of lead halide perovskite NCs has only been realized very recently but already has developed to an active research area⁵⁹⁻⁶³. The fast development of doped perovskite NCs is not only motivated by the prospect of combining the attractive properties of perovskite nanocrystals (e.g. high PL QY) with dopant ions (e.g. bright sub-bandgap emission and magnetism) but also by the potentially useful and interesting new photo-magneto properties originating from exciton-Mn²⁺ interaction. The synthesis of doped nanocrystals has long been considered as a challenge. Doping of nanocrystals is often more difficult than doping their bulk crystalline counterparts. The intrinsic difficulty of doping of nanocrystals is usually explained from a kinetic perspective. A large difference in chemical properties can exist between dopant ions and host matrix ions which leads to a low compatibility and thus incorporation of the dopant in the host matrix NCs⁶⁴.

Many methods have been applied to grow high-quality Mn²⁺ doped nanocrystals⁵⁴. The successful synthesis of Mn²⁺-doped perovskite nanocrystals was first reported by Klimov *et al.*⁵⁹ and Son *et al.*⁶⁰. Bright Mn²⁺-doped CsPbCl₃ NCs can be achieved by a simple adaption of the procedure of undoped perovskite NCs. Mn²⁺-doped CsPbCl₃ nanocrystals can be obtained by injection of a cesium precursor into a manganese-lead halide precursor solution at 190 °C. The resulting product shows bright Mn²⁺ emission at 600 nm originated from 3d⁵ intraconfigurational Mn²⁺ transition (⁴T₁ → ⁶A₁). Several room temperature synthesis approaches have also been developed^{61,62,65}. Nag *et al.*⁶¹ reported Mn²⁺-doped CsPbCl₃ nanoplatelets with a method similar to that for the undoped counterpart. 20 % PL QY of Mn²⁺ emission can be achieved with only 0.8 at% of dopant concentration. Another method was reported by Meijerink *et al.*⁶². In a clear toluene solution of metal precursors (Cs⁺, Pb²⁺ and Mn²⁺) with surface ligands (oleic acid, oleylamine), the fast injection of concentrated hydrochloric acid protonates the metal-ligand complex and yields a large amount of active metal monomers. The subsequent crystallization of CsPbCl₃ nanocrystals and incorporation of Mn²⁺ ions is facilitated by excess chlorine ions in the reaction medium. The favorable influence of a high concentration of anions is also observed in the synthesis

Chapter 1

of Mn^{2+} -doped CsPbBr_3 NCs ⁶⁶. The underlying mechanism is that the high chemical potential of the dopant created by a high anion concentrations provides a driving force for the dopant ion to be incorporated into the host NCs. Highly Mn-doped samples have also been achieved by a ligand assisted precipitation method ⁶⁵, achieving a highest dopant concentration of ~ 38 at.%. Figure 1.7 summarizes the different synthesis approaches.

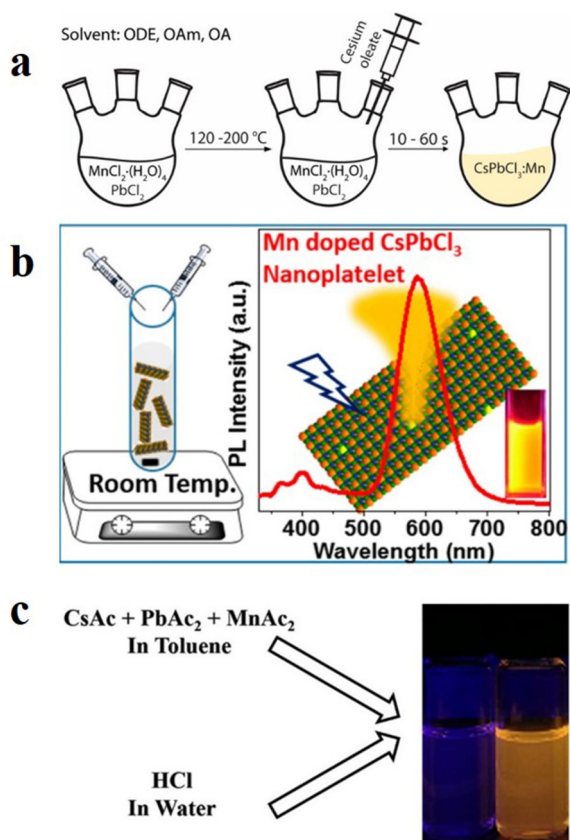


Figure 1.7. Schematic representation of different synthesis methods for Mn-doped perovskite NCs (adapted from Refs. 60, 61, 62 with permission)

1.4 Optical Properties of Mn²⁺ Doped CsPbCl₃ NCs

Successful incorporation of luminescent dopant ions in quantum dots provides additional flexibility in tuning the luminescence properties. A widely used dopant is Mn²⁺ and the change in luminescence depends on the exciton-Mn²⁺ interaction. The electron configuration of Mn²⁺ is 3d⁵. The partly filled 3d shell is the origin of the intriguing optical and magnetic properties of Mn²⁺. The energy level structure of the Mn²⁺ dopant depends strongly on the crystal field at the crystallographic site where Mn²⁺ substitutes and the covalency of the host. The optical properties can be understood using a so-called Tanabe-Sugano diagram. In Figure 1.8 the Tanabe-Sugano diagram for the 3d⁵ configuration is depicted. The energy of different electronic states that arise by the crystal field splitting of free ion states (denoted by term symbols) are labelled according to their symmetry properties that correspond to the irreducible representations in the symmetry group for the point symmetry of the site on which the transition metal ion substitutes. For Mn²⁺ substituting on an octahedral site, the crystal field levels are labelled A₁ or A₂ for singly (orbital) degenerate states, E for a doubly degenerate state and T₁ and T₂ for triply degenerate states. The number in the left upper corner denotes the spin degeneracy (2S+1 where S is total spin angular momentum). The energy of the crystal field levels is plotted as a function of the crystal field splitting Δ in a Tanabe-Sugano diagram.

The crystal field splitting depends on the nature of the ligands (coordinating anions) surrounding the Mn²⁺ ion. A higher charge and/or smaller distances results in a larger crystal field splitting. The energy and crystal splitting are both divided by the Racah parameter B to scale the diagram for universal applicability. The Racah parameter depends on the covalency of the host. For increasing host covalency the 3d electrons become more delocalized over the ligands and this reduces the inter-electron repulsion for the 3d⁵ electrons and results in a smaller energy separation between the energy levels. This is known as the nephelauxetic effect ('cloud expanding' effect). For a specific local environment for Mn²⁺ in a host lattice the values for Δ and B are fixed and the energy level scheme can be found as a vertical line at a specific value for Δ/B . For example, for $\Delta/B = 1.5$ the ground state of Mn²⁺ is ⁶A₁, the first excited state is ⁴T₁ followed by ⁴T₂ and many more excited states. In the absorption spectrum transition to the different excited states can be assigned using the Tanabe-Sugano diagram.

Chapter 1

Emission occurs from the lowest excited state, in this case ${}^4T_1 \rightarrow {}^6A_1$ emission. The emission is spin forbidden as S changes from $1\frac{1}{2}$ in the excited state to $2\frac{1}{2}$ in the ground state. The spin forbidden character results in long lived (emission lifetime on the scale of ms) Mn^{2+} emission. The spin-forbidden character can be partly relaxed by the spin-orbit coupling which is more prominent for heavier atoms. Note that also all absorption transitions are spin forbidden (the 6A_1 ground state is the only state with $S=2\frac{1}{2}$) and this results in weak absorption bands and lines. All transitions within the $3d^5$ configuration are also parity forbidden since the electron configuration in ground and excited state are the same ($3d^5$) and thus no change in dipole moment is induced during the optical transition. The shape of the absorption and emission lines depends on the slope of the excited states relative to the ground state.

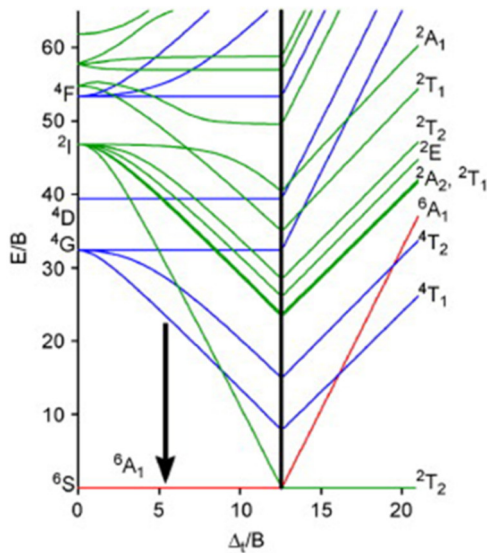


Figure 1.8. Tanabe-Sugano diagram showing the energy levels for a transition metal ion with the $3d^5$ configuration, e.g. Mn^{2+} (Reprinted from Ref. 67 with permission).

Step slopes result in broad bands and transitions to excited states that are parallel to the ground state appear as sharp(er) lines in the absorption spectrum. The reason is that the

Chapter 1

crystal field splitting Δ is not constant because of vibrations (distance variations) of the Mn-ligands. For excited states with a sloping line, variations in Δ will result in a different energy for the transition and thus broadening of the absorption or emission band.

The emission spectrum of Mn^{2+} doped CsPbCl_3 NCs, shows in addition to the sharp exciton emission line around 410 nm a broad emission band of Mn^{2+} , located around 590 nm originating from the ${}^4\text{T}_1 \rightarrow {}^6\text{A}_1$ transition. Increasing the dopant concentration can suppress the exciton emission by enhanced exciton-dopant energy transfer. For $\text{CsPbCl}_3:\text{Mn}^{2+}$ the exciton-to- Mn^{2+} energy transfer is relatively inefficient and complete quenching the exciton emission is not achieved, even at Mn^{2+} concentrations as high as 50 at.%. Clearly, the energy transfer rate is lower in Mn^{2+} -doped CsPbCl_3 perovskite NCs than in Mn^{2+} -doped II-VI semiconductor NCs. This has been explained by the ionic nature of the CsPbCl_3 NCs. Several groups have studied the exciton-to- Mn^{2+} energy transfer dynamics with different methods. Son et al.⁶³ measured an energy transfer time of ~ 380 ps using transient absorption spectroscopy. This is more than an order of magnitude slower than in Mn^{2+} -doped II-VI NCs⁶⁸. Similar energy transfer times were determined from low temperature time resolved spectroscopy⁶⁹. Confinement of the exciton wavefunction can contribute to enhanced energy transfer and an increase of the Mn^{2+} emission intensity. For example, a lower Mn^{2+} dopant concentration in CsPbCl_3 nanoplates (0.8 at.%, 20%) can result in a comparable Mn^{2+} PL QY to highly doped CsPbCl_3 nanocubes (9.6 at.%, 27%). Tuning the anion composition in the host matrix can also affect the relative Mn^{2+} emission intensity and is investigated in **Chapter 4** of this thesis.

Next to 3d transition metal ions, also lanthanide ions (Ln^{3+}) are promising as luminescent dopants in QDs. Because of differences in chemical properties and charge (lanthanides are trivalent) doping Ln^{3+} in QDs has been challenging. Especially in II-VI QDs such as CdSe in spite of considerable effort only Ln-doping in a surface layer has been realized. In II-VI QDs exclusively four-coordinated cation sites are available and lanthanide ions require coordination numbers of six or higher. In CsPbX_3 the six coordinated Pb-site is promising for doping with Ln^{3+} ions. Recently, the Yb^{3+} -doped CsPbCl_3 NCs have been synthesized, manifesting a close to 200% PL QY of Yb^{3+} NIR emission⁷⁰. In contrast to isovalent ion (Mn^{2+}) doping, the aliovalent doping (Yb^{3+}) is proposed to result in the formation of locally charge neutral Yb^{3+} -Vacancy²⁻- Yb^{3+} complexes which can efficiently trap the exciton energy. Subsequently, the localized exciton can transfer its energy to excite two Yb^{3+} ions and that

each emits an infrared photon. This quantum cutting process gives rise to the above-unity PL QYs.

1.6 Outline of this thesis

In the field perovskite nanocrystals new synthesis strategies for doped and undoped NCs are required to realize stable and efficiently luminescent NCs. This thesis starts by exploring new synthesis strategies of perovskite nanocrystals and Mn^{2+} -doped perovskite nanocrystals, followed by the systematic study on the evolution of exciton- Mn^{2+} energy transfer processes and exciton structure as a function of temperature and composition of the NCs. The aim of this thesis is to provide further insight into the synthesis and the optical properties of Mn^{2+} -doped perovskite nanocrystals.

In **Chapter 2** a facile and fast one-pot room temperature synthesis method of CsPbX_3 ($X=\text{Cl, Br, I}$) NCs is reported. In toluene, strong luminescent CsPbX_3 NCs are obtained within 10 min by addition of a small volume of a concentrated HX ($X= \text{Cl, Br}$ and I) solution to a clear Cs^+ and Pb^{2+} precursor solution. By varying the halide composition in the NCs almost the full visible range (violet to red) can be covered by highly efficient CsPbX_3 NCs. The NCs have improved stability in the presence of water and the origin of enhanced stability of NCs is ascribed to the formation of a stable ligand shell because of the high halide concentration.

The following chapters all discuss Mn-doped perovskite NCs. In **Chapter 3** a room temperature method for Mn^{2+} doping into CsPbCl_3 NCs is developed. By addition of a small amount of concentrated HCl acid to a clear solution containing Mn^{2+} , Cs^+ and Pb^{2+} precursors, Mn^{2+} doped CsPbCl_3 NCs with strong orange luminescence of Mn^{2+} at ~ 600 nm is obtained. Mn^{2+} doped CsPbCl_3 NCs show the characteristic cubic phase crystal structure very similar to the undoped counterpart, indicating that the nucleation and growth mechanism are not significantly modified for the doping concentrations realized (0.1 at.% - 2.1 at.%). To enhance the Mn^{2+} emission intensity and to improve the stability of the doped NCs, isocrystalline shell growth was applied. Growth of an undoped CsPbCl_3 shell greatly enhances the emission intensity of Mn^{2+} and results in lengthening the radiative lifetime of the Mn^{2+} emission to 1.4 ms. The core-shell NCs also show superior thermal stability and no thermal degradation up to at least 110 °C which is important in applications.

Chapter 1

Doping nanocrystals (NCs) with luminescent activators provides additional color tunability through energy transfer (ET) from the exciton to the dopant. In CsPbCl₃ perovskite NCs the exciton-to-activator ET has also been observed but is much less efficient than in II-VI semiconductor NCs. In **Chapter 4** we investigate the evolution of the exciton-to-Mn²⁺ ET efficiency as function of composition (Br/Cl ratio) and temperature in CsPbCl_{3-x}Br_x: Mn²⁺ NCs. The results show a strong dependence of the transfer efficiency on Br⁻ content. An initial fast increase in the relative Mn²⁺ emission intensity with increasing Br⁻ content is followed by a decrease for higher Br⁻ contents. The results are explained by a reduced exciton decay rate and faster exciton-to-Mn²⁺ ET upon Br⁻ substitution. Further addition of Br⁻ and narrowing of the host bandgap makes back transfer from Mn²⁺ to the CsPbCl_{3-x}Br_x host possible and leads to a reduction in Mn²⁺ emission. Temperature dependent measurements provide support for the role of back transfer as the highest Mn²⁺-to-exciton emission intensity ratio is reached at higher Br⁻ content at 4.2 K where thermally activated back transfer is suppressed. With the present results it is possible to pinpoint the position of the Mn²⁺ excited state relative to the CsPbCl_{3-x}Br_x host band states and predict the temperature and composition dependent optical properties of Mn²⁺-doped halide perovskite NCs.

The unusual temperature dependence of exciton emission decay in CsPbX₃ perovskite NCs attracts considerable attention. The room temperature lifetime is much shorter than in traditional quantum dots (QDs) which is beneficial for potential applications. Upon cooling extremely short (sub-ns) lifetimes are observed below 20 K which has been explained by an inverted bright-dark state splitting. In **Chapter 5** the temperature dependence of exciton lifetimes is investigated for CsPbCl₃ NCs doped with 0 to 41% Mn²⁺. The exciton emission lifetime increases upon cooling from 300 to 75 K. Upon further cooling a strong and fast sub-ns decay component develops. However, the decay is strongly bi-exponential and also a weak slow decay component is observed with a ~40-50 ns life time below 20 K. The slow component has a much stronger relative intensity in Mn-doped NCs compared to undoped CsPbCl₃ NCs. The temperature dependence of the slow decay component resembles that of CdSe and PbSe QDs with an activation energy of ~19 meV for the dark-bright state splitting. Based on our observations an alternative explanation is proposed for the fast sub-ns exciton decay time in CsPbX₃ NCs. Slow bright-dark state relaxation at cryogenic temperatures gives rise to almost exclusively bright state emission. Incorporation of Mn²⁺

Chapter 1

or high magnetic fields enhances the bright-dark state relaxation and allow for the observation of the long-lived dark state emission at cryogenic temperatures.

References

1. Mello Donega, C. de, Synthesis and Properties of Colloidal Heteronanocrystals. *Chem. Soc. Rev.*, 2011, 40, 1512-1546.
2. Pietryga, J. M.; Park, Y. S.; Lim, J.; Fidler, A. F.; Bae, W. K.; Brovelli, S.; Klimov, V. I., Spectroscopic and Device Aspects of Nanocrystal Quantum Dots. *Chem. Rev.*, 2016, 116, 10513-10622.
3. Chang, J.; Waclawik, E. R., Colloidal Semiconductor Nanocrystals: Controlled Synthesis and Surface Chemistry in Organic Media. *RSC Adv.*, 2014, 4, 23505-23527.
4. Alivisatos, A. P., Perspectives on the Physical Chemistry of Semiconductor Nanocrystals. *J. Phys. Chem.*, 100, 31, 13226-13239.
5. Rabouw, F. T.; Mello Donega, C. de, Excited-state Dynamics in Colloidal Semiconductor Nanocrystals. *Top. Curr. Chem.*, 2016, 374, 58.
6. Roduner, E., Size Matters: Why Nanomaterials Are Different. *Chem. Soc. Rev.*, 2006, 35, 583-592.
7. Kilina, S. V.; Tamukong, P. K.; Kilin, D. S., Surface Chemistry of Semiconducting Quantum Dots: Theoretical Perspectives. *Acc. Chem. Res.*, 2016, 49, 2127-2135.
8. Giansante, C., Surface Chemistry Control of Colloidal Quantum Dot Band Gap. *J. Phys. Chem. C*, 2018, 122, 18110-18116.
9. Hines, D. A.; Kamat, P. V., Recent Advances in Quantum Dot Surface Chemistry. *ACS Appl. Mater. Interfaces.*, 2014, 6, 3041-3057.
10. Boles, M. A.; Ling, D.; Hyeon, T.; Talapin, D. V., the Surface Science of Nanocrystals. *Nat. Mater.*, 2016, 15, 141-153.
11. Wuister, S. F.; Mello Donega, C. de; Meijerink, A., Influence of Thiol Capping on the Exciton Luminescence and Decay Kinetics of CdTe and CdSe Quantum Dots. *J. Phys. Chem. B*, 2004, 108, 17393-17397.
12. Dirin, D. N.; Dreyfuss, S.; Bodnarchuk, M. I.; Nedelcu, G.; Papagiorgis, P.; Itskos, G.; Kovalenko, M. V., Lead Halide Perovskites and Other Metal Halide Complexes As Inorganic Capping Ligands for Colloidal Nanocrystals. *J. Am. Chem. Soc.*, 2014, 136, 6550-6553.
13. Xia, Z.; Zhong, J.; Leng, M.; Hu, L.; Xue, D. J.; Yang, B.; Zhou, Y.; Liu, X.; Qin, Chen, Y. B.; Tang, J., Generalized Water-processed Metal Chalcogenide Complexes: Synthesis and Applications. *Chem. Mater.*, 2015, 27, 8048-8057.

Chapter 1

14. Jin, H.; Choi, S.; Xing, G.; Lee, J. H.; Kwon, Y.; Chong, W. K.; Sum, T. C.; Jang, H. M.; Kim, S., SnS_4^{4-} , SbS_4^{3-} , and AsS_3^{3-} Metal Chalcogenide Surface Ligands: Couplings to Quantum Dots, Electron Transfers, and All-inorganic Multilayered Quantum Dot Sensitized Solar Cells. *J. Am. Chem. Soc.*, 2015, *137*, 13827-13835.
15. Kovalenko, M. V.; Bodnarchuk, M. I., Zaumseil, J.; Lee, J. S.; Talapin, D. V., Expanding the Chemical Versatility of Colloidal Nanocrystals Capped with Molecular Metal Chalcogenide Ligands. *J. Am. Chem. Soc.*, 2010, *132*, 10085-10092.
16. Koh, W.; Saudari, S. R.; Fafarman, A. T.; Kagan, C. R.; Murray, C. B., Thiocyanate-Capped PbS Nanocubes: Ambipolar Transport Enables Quantum Dot Based Circuits on a Flexible Substrate. *Nano Lett.*, 2011, *11*, 4764-4767.
17. Nag, A.; Kovalenko, M. V.; Lee, J. S.; Liu, W.; Spokoyny, B.; Talapin, D. V., Metal-free Inorganic Ligands for Colloidal Nanocrystals: S^{2-} , HS^- , Se^{2-} , HSe^- , Te^{2-} , HTe^- , TeS_3^{2-} , OH^- , and NH_2^- as Surface Ligands. *J. Am. Chem. Soc.*, 2011, *133*, 10612-10620.
18. Fafarman, A. T.; Koh, W.; Diroll, B. T.; Kim, D. K.; Ko, D. K.; Oh, S. J.; Ye, X.; Doan-Nguyen, V.; Crump, M. R.; Reifsnnyder, D. C.; Murray, C. B.; Kagan, C. R., Thiocyanate-capped Nanocrystal Colloids: Vibrational Reporter of Surface Chemistry and Solution-based Route to Enhanced Coupling in Nanocrystal Solids. *J. Am. Chem. Soc.*, 2011, *133*, 15753-15761.
19. Lan, X.; Voznyy, O.; Kiani, A.; de Arquer, F. P. G.; Abbas, A. S.; Kim, G. H.; Liu, M.; Yang, Z.; Walters, G.; Xu, J.; Yuan, M.; Ning, Z.; Fan, F.; Kanjanaboos, P.; Kramer, I.; Zhitomirsky, D.; Lee, P.; Perelgut, A.; Hoogland, S.; Sargent, E. H.; Passivation Using Molecular Halides Increases Quantum Dot Solar Cell Performance. *Adv. Mater.*, 2016, *28*, 299-304.
20. Bae, W. K.; Joo, J.; Padilha, L. A.; Won, J.; Lee, D. C.; Lin, Q.; Koh, W.; Luo, H.; Klimov, V. I.; Pietryga, J. M., Highly Effective Surface Passivation of PbSe Quantum Dots through Reaction with Molecular Chlorine. *J. Am. Chem. Soc.*, 2012, *134*, 20160-20168.
21. Zhang, J.; Gao, J.; Miller, E. M.; Luther, J. M.; Beard, M. C., Diffusion-controlled Synthesis of PbS and PbSe Quantum Dots with In Situ Halide Passivation for Quantum Dot Solar Cells. *ACS Nano*, 2014, *8*, 614-622.
22. Yang, Z.; Janmohamed, A.; Lan, X.; de Arquer, F. P. G.; Voznyy, O.; Yassitepe, E.; Kim, G. H.; Ning, Z.; Gong, X.; Comin, R.; Sargent, E. H., Colloidal Quantum Dot Photovoltaics Enhanced by Perovskite Shelling. *Nano Lett.*, 2015, *15*, 7539-7543.

Chapter 1

23. Gong, X.; Yang, Z.; Walters, G.; Comin, R.; Ning, Z.; Beauregard, E.; Adinolfi, V.; Voznyy, O.; Sargent, E. H., Highly Efficient Quantum Dot Near-infrared Light-Emitting Diodes. *Nat. Photon.*, 2016, *10*, 253-257.
24. Kovalenko, M. V.; Protesescu, L.; Bodnarchuk, M. I., Properties and Potential Optoelectronic Applications of Lead Halide Perovskite Nanocrystals. *Science*, 2017, *358*, 745-750.
25. Akkerman, Q. A.; Rainò, G.; Kovalenko, M. V.; Manna, L., Genesis, Challenges and Opportunities for Colloidal Lead Halide Perovskite Nanocrystals. *Nat. Mater.*, 2018, *17*, 394-405.
26. Stranks, S. D.; Snaith, H. J., Metal-halide Perovskites for Photovoltaic and Light-emitting Devices. *Nat. Nanotechnol.*, 2015, *10*, 391-402.
27. Zhu, H.; Fu, Y.; Meng, F.; Wu, X.; Gong, Z.; Ding, Q.; Gustafsson, M. V. Trinh, M. T.; Jin, S.; Zhu, X. Y., Lead Halide Perovskite Nanowire Lasers with Low Lasing Thresholds and High Quality Factors. *Nat. Mater.*, 2015, *14*, 636-642.
28. Adachi, M. M.; Fan, F.; Sellan, D. P.; Hoogland, S.; Voznyy, O.; Houtepen, A. J.; Parrish, K. D.; Kanjanaboos, P.; Malen, J. A.; Sargent, E. H., Microsecond-sustained Lasing from Colloidal Quantum Dot Solids. *Nat. Commun.*, 2015, *6*, 8694-8702.
29. Yakunin, S.; Sytnyk, M.; Kriegner, D.; Shrestha, S.; Richter, M.; Matt, G. J.; Azimi, H.; Brabec, C. J.; Stangl, J.; Kovalenko, M. V.; Heiss, W., Detection of X-ray Photons by Solution-processed Lead Halide Perovskites. *Nat. Photon.*, 2015, *9*, 444-449.
30. Stoumpos, C. C.; Kanatzidis, M. G., The Renaissance of Halide Perovskites and Their Evolution as Emerging Semiconductors. *Acc. Chem. Res.*, 2015, *48*, 2791-2802.
31. Song, Z.; Wathage, S. C.; Phillips, A. B.; Tompkins, B. L.; Ellingson, R. J.; Heben, M. J., Impact of Processing Temperature and Composition on the Formation of Methylammonium Lead Iodide Perovskites. *Chem. Mater.*, 2015, *27*, 4612-4619.
32. Veldhuis, S. A.; Boix, P. P.; Yantara, N.; Li, M.; Sum, T. C.; Mathews, N.; Mhaisalkar, S. G., Perovskite Materials for Light-Emitting Diodes and Lasers. *Adv. Mater.*, 2016, *28*, 6804-6834.
33. Møller, C. K., Crystal Structure and Photoconductivity of Cæsium Plumbohalides. *Nature*, 1958, *182*, 1436.
34. Møller, C. K., A Phase Transition in Cæsium Plumbochloride. *Nature*, 1957, *180*, 981-982.

Chapter 1

35. Protesescu, L.; Yakunin, S.; Bodnarchuk, M. I.; Krieg, F.; Caputo, R.; Hendon, C. H.; Yang, R.; Walsh, A.; Kovalenko, M. V. Nanocrystals of Cesium Lead Halide Perovskites (CsPbX_3 , X = Cl, Br, and I): Novel Optoelectronic Materials Showing Bright Emission with Wide Color Gamut. *Nano Lett.*, 2015, 15, 3692-3696.
36. Bertolotti, F.; Protesescu, L.; Kovalenko, M. V.; Yakunin, S.; Cervellino, A.; Billinge, S. J. L.; Terban, M. W.; Pedersen, J. S.; Masciocchi, N.; Guagliardi, A., Coherent Nanotwins and Dynamic Disorder in Cesium Lead Halide Perovskite Nanocrystals. *ACS Nano*, 2017, 11, 3819–3831.
37. Belikovitch, B. A.; Pashchuk, I. P.; Pidzyrailo, N. S., Luminescence of CsPbCl_3 Single Crystals. *Opt Spectrosc+*, 1977, 42, 62-64.
38. Heidrich, K.; Künzel, H.; Treusch, J., Optical Properties and Electronic Structure of CsPbCl_3 and CsPbBr_3 . *Solid State Commun.*, 1978, 25, 887-889.
39. Nikl, M.; Nitsch, K.; Polak, K.; Pazzi, G. P.; Fabeni, P.; Citrin, D. S.; Gurioli, M., Optical Properties of the Pb^{2+} -based Aggregated Phase in a CsCl Host Crystal: Quantum-Confinement Effects. *Phys. Rev. B*, 1995, 51, 5192-5199.
40. Nikl, M.; Nitsch, K.; Polak, K.; Mihokova, E.; Zazubovich, S.; Pazzi, G. P.; Fabeni, P.; Salvini, L.; Aceves, R.; Barboza-Flores, M.; Perez-Salas, R.; Gurioli, M.; Scacco, A., Quantum Size eEffect in the Excitonic Luminescence of CsPbX_3 -like Quantum Dots in CsX (X = Cl, Br) Single Crystal Host. *J. Lumin.*, 1977, 72, 377-379.
41. Aceves, R.; Babin, V.; Barboza-Flores, M.; Fabeni, P.; Nikl, M.; Nitsch, K.; Pazzi, G.P. Perez-Salas, R.; Zazubovich, S., Luminescence of CsPbCl_3 -like Quantum Dots in CsCl: Pb Crystals. *Phys. Stat. Sol.*, 2001, 225, 247-255.
42. Thanh, N. T. K.; Maclean, N.; Mahiddine, S., Mechanisms of Nucleation and Growth of Nanoparticles in Solution. *Chem. Rev.*, 2014, 114, 7610-7630.
43. Murray, C. B.; Norris, D. J.; Bawendi, M. G., Synthesis and Characterization of Nearly Monodisperse CdE (E = sulfur, selenium, tellurium) Semiconductor Nanocrystallites. *J. Am. Chem. Soc.*, 1993, 115, 8706-8715.
44. Tsiwah, E. A.; Ding, Y.; Li, Z.; Zhao, Z.; Wang, W.; Hu, C.; Liu, X.; Sun, C.; Zhao, X.; Xie, Y., One-pot Scalable Synthesis of All-inorganic Perovskite Nanocrystals with Tunable Morphology, Composition and Photoluminescence. *CrystEngComm.*, 2017, 19, 7041-7049.
45. Tong, Y.; Bohn, B. J.; Bladt, E.; Wang, K.; Müller, P. B.; Bals, S.; Urban, A. S.; Polavarapu, L.; Feldmann, J., From Precursor Powders to CsPbX_3 Perovskite Nanowires:

Chapter 1

One-pot Synthesis, Growth Mechanism, and Oriented Self-Assembly. *Angew. Chem. Int. Ed.*, 2017, 56, 13887-13892.

46. Chen, X.; Peng, I.; Huang, K.; Shi, Z.; Xie, R.; Yang, W., Non-injection Gram-scale Synthesis of Cesium Lead Halide Perovskite Quantum Dots with Controllable Size and Composition. *Nano Res.*, 2016, 9, 1994-2006.

47. Li, X.; Wu, Y.; Zhang, S.; Cai, B.; Gu, Y.; Song, J.; Zeng, H., CsPbX₃ Quantum Dots for Lighting and Displays: Room-Temperature Synthesis, Photoluminescence Superiorities, Underlying Origins and White Light-emitting Diodes. *Adv. Funct. Mater.*, 2016, 26, 2435-2445.

48. Wei, S.; Yang, Y.; Kang, J.; Wang, L.; Huang, L.; Pan, D., Room-temperature and Gram-scale Synthesis of CsPbX₃ (X = Cl, Br, I) Perovskite Nanocrystals with 50–85% Photoluminescence Quantum Yields. *Chem. Commun.*, 2016, 52, 7265-7268.

49. Zhong, Q.; Cao, M.; Hu, H.; Yang, D.; Chen, M.; Li, P.; Wu, L.; Zhang, Q., One-Pot Synthesis of Highly Stable CsPbBr₃@SiO₂ Core-Shell Nanoparticles. *ACS Nano*, 2018, 12, 8579-8587.

50. Jang, D. M.; Kim, D. H.; Park, K.; Park, J.; Lee, J. W.; Song, J. K., Ultrasound Synthesis of Lead Halide Perovskite Nanocrystals. *J. Mater. Chem. C*, 2016, 4, 10625-10629.

51. Dirin, D. N.; Protesescu, L.; Trummer, D.; Kochetygov, I. V.; Yakunin, S.; Krumeich, F.; Stadie, N. P.; Kovalenko, M. V., Harnessing Defect-Tolerance at the Nanoscale: Highly Luminescent Lead Halide Perovskite Nanocrystals in Mesoporous Silica Matrixes. *Nano Lett.*, 2016, 16, 5866-5874.

52. Malgras, V.; Tominaka, S.; Ryan, J. W.; Henzie, J.; Takei, T.; Ohara, K.; Yamauchi, Y., Observation of Quantum Confinement in Monodisperse Methylammonium Lead Halide Perovskite Nanocrystals Embedded in Mesoporous Silica. *J. Am. Chem. Soc.*, 2016, 138, 13874-13881.

53. Ma, H. H.; Imran, M.; Dang, Z.; Hu, Z., Growth of Metal Halide Perovskite, from Nanocrystal to Micron-Scale Crystal: A Review. *Crystals*. 2018, 8, doi:10.3390/cryst8050182.

54. Buonsanti, R.; Milliron, D. J., Chemistry of Doped Colloidal Nanocrystals. *Chem. Mater.*, 2013, 25, 1305-1317.

55. Jana, S.; Srivastava, B. B.; Jana, S.; Bose, R.; Pradhan, N., Multifunctional Doped Semiconductor Nanocrystals. *J. Phys. Chem. Lett.*, 2012, 3, 2535-2540.

Chapter 1

56. Knowles, K. E.; Hartstein, K. H.; Kilburn, T. B.; Marchioro, A.; Nelson, H. D.; Whitham, P. J.; Gamelin, D. R., Luminescent Colloidal Semiconductor Nanocrystals Containing Copper: Synthesis, Photophysics, and Applications. *Chem. Rev.*, 2016, *116*, 10820-10851.
57. Srivastava, B. B.; Jana, S.; Karan, N. S.; Paria, S.; Jana, N. R.; Sarma, D. D.; Pradhan, N., Highly Luminescent Mn-doped ZnS Nanocrystals: Gram-Scale Synthesis. *J. Phys. Chem. Lett.*, 2010, *1*, 1454-1458.
58. Erickson, C. S.; Bradshaw, L. R.; McDowall, S.; Gilbertson, J. D.; Gamelin, D. R.; Patrick, D. L., Zero-reabsorption Doped-nanocrystal Luminescent Solar Concentrators. *ACS Nano*, 2014, *8*, 3461-3467.
59. Liu, W.; Lin, Q.; Li, H.; Wu, K.; Robel, I.; Pietryga, J. M.; Klimov, V. I., Mn²⁺-doped Lead Halide Perovskite Nanocrystals with Dual-color Emission Controlled by Halide Content, *J. Am. Chem. Soc.*, 2016, *138*, 14954-14961.
60. Parobek, D.; Roman, B. J.; Dong, Y.; Jin, H.; Lee, E.; Sheldon, M.; Son, D. H., Exciton-to-Dopant Energy Transfer in Mn-doped Cesium Lead Halide Perovskite Nanocrystals. *Nano Lett.*, 2016, *16*, 7376-7380.
61. Mir, W. J.; Jagadeeswararao, M.; Das, S.; Nag, A., Colloidal Mn-doped Cesium Lead Halide Perovskite Nanoplatelets. *ACS Energy Lett.*, 2017, *2*, 537-543.
62. Xu, K.; Lin, C. C.; Xie, X.; Meijerink, A., Efficient and Stable Luminescence from Mn²⁺ in Core and Core-isocrystalline Shell CsPbCl₃ Perovskite Nanocrystals. *Chem. Mater.*, 2017, *29*, 4265-4272.
63. Rossi, D.; Parobek, D.; Dong, Y.; Son, D. H., Dynamics of Exciton-to-Mn Energy Transfer in Mn-Doped CsPbCl₃ Perovskite Nanocrystals. *J. Phys. Chem. C*, 2017, *121*, 17143-17149.
64. Dalpian, G. M.; Chelikowsky, J. R., Self-purification in Semiconductor Nanocrystals. *Phys. Rev. Lett.* 2006, *96*, 226802.
65. Zhu, J.; Yang, X.; Zhu, Y.; Wang, Y.; Cai, J.; Shen, J.; Sun, L.; Li, C., Room-temperature Synthesis of Mn-doped Cesium Lead Halide Quantum Dots with High Mn Substitution Ratio. *J. Phys. Chem. Lett.*, 2017, *8*, 4167-4171.
66. Parobek, D.; Dong, Y.; Qiao, T.; Son, D. H., Direct Hot-injection Synthesis of Mn-Doped CsPbBr₃ Nanocrystals. *Chem. Mater.*, 2018, *30*, 2939-2944.
67. Beaulac, R.; Archer, P. I.; Gamelin, G. R., Luminescence in Colloidal Mn²⁺-doped Semiconductor Nanocrystals. *J. Solid State Chem.*, 2008, *181*, 1582-1589.

Chapter 1

68. Vlaskin, V. A.; Janssen, N.; van Rijssel, J.; Beaulac, R.; Gamelin, D. R. Tunable Dual Emission in Doped Semiconductor Nanocrystals. *Nano Lett.*, 2010, *10*, 3670-3674.
69. Xu, K.; Meijerink, A., Tuning Exciton–Mn²⁺ Energy Transfer in Mixed Halide Perovskite Nanocrystals. *Chem. Mater.*, 2018, *30*, 5346-5352.
70. Milstein, T. J.; Kroupa, D. M.; Gamelin, D. R., Picosecond Quantum Cutting Generates Photoluminescence Quantum Yields Over 100% in Ytterbium-doped CsPbCl₃ Nanocrystals. *Nano Lett.*, 2018, *18*, 3792-3799.

Chapter 1

Chapter 2

Facile One-Pot Synthesis of CsPbX₃ (X=Cl, Br, I) Perovskite Nanocrystals

Abstract

All-inorganic CsPbX₃ (X=Cl, Br, I) perovskite nanocrystals form a new and promising class of materials with unique size dependent optical properties, high luminescence quantum yield and colour tunability over the full visible spectrum. Recently, room temperature synthesis methods have been reported for CsPbCl₃ and CsPbBr₃ based on dual solvent methods. Here we report a fast and facile one-pot room temperature synthesis method for CsPbX₃ (X=Cl, Br, I) NCs in toluene. Highly luminescent CsPbX₃ NCs are obtained within 10 minutes by addition of a small volume of a concentrated halide acid solution to a clear precursor solution of Cs⁺ and Pb²⁺.

2.1 Introduction

In the past decade research on lead halide perovskite (LHP) materials has seen a spectacular rise.¹⁻³ The success in achieving record high conversion efficiencies in solar cells, reaching nearly 20% power conversion within a few years⁴⁻⁶ and the size-tunable physical properties through quantum confinement effects in LHP nanostructures have triggered the rapid growth in research on this interesting class of materials. The excellent photo-physical properties combined with the flexible and cost-effective solution-processability and low-temperature synthesis methods for LHP materials may initiate a new era in the renewable energy industry.⁷ A big challenge that remains is the limited stability of this class of perovskites, both to moisture and elevated temperatures.

LHP materials are not only promising for conversion of light to electricity but also for the reverse process. Highly efficient emission over the full visible range has been realized for LHPs and this makes these materials also suitable for optoelectronic applications such as light-emitting diodes (LEDs), displays and lasers.^{3,8} In these applications a high luminescence efficiency is crucial and an effective way to improve the efficiency of LHP based LEDs is fabrication of nano-sized, defect free LHP NCs with high luminescence quantum yield.

NCs, also known as artificial atoms, are inorganic or organic-inorganic hybrid nanomaterials which exhibit unique size-dependent optical properties.⁹ Due to quantum confinement effects the absorption and emission wavelengths can be continuously tuned while the quantum yield can be high (even close to 100 %). Typically, the NCs are synthesized by state-of-art hot injection (HI) methods for the synthesis of nearly defect-free quantum dots with a remarkably small size distribution (less than 10 % polydispersity).¹⁰ However, high temperatures and sometimes toxic chemicals, are involved in the synthesis process. Inspired by the fact that crystalline LHP materials can be synthesized at relatively low temperatures, extensive work on room temperature synthesis of LHP NCs has been reported.^{11,12}

Organic-inorganic hybrid LHP (MAPbX₃, MA= CH₃NH₃⁺, X=Cl, Br, I) NCs with photoluminescence quantum yields (PLQYs) of 50~70% were fabricated at room temperature by Ligand-Assisted Re-Precipitation method (LARP).¹¹ Also for full inorganic LHP NCs, a room temperature LARP based synthesis method was published shortly after

the first report of a successful HI synthesis method.^{12,13}

The LARP method is essentially a bottom-up method. A solution containing nano-clusters of precursors is made by dissolving the precursors (e.g. PbX_2 and CsX , $\text{X}=\text{Cl}$, Br , I) and surface ligand (e.g. oleic acid and oleylamine) in a good solvent which is usually dimethylformamide (DMF) or dimethyl sulfoxide (DMSO). Injection of this precursor solution to the poor solvent, toluene, gives rise to over-saturation of precursors which triggers the crystallization and precipitation of crystals. The presence of surfactant molecules passivating the surface results in the formation of free-standing NCs. The choice of a suitable good-poor solvent pair is integral to inducing the crystallization and obtaining nano-sized particles. Despite the elegance of this method, this two-solvent method takes a relatively long time making it less cost effective. Furthermore, due to the meta-stable nature of optical active (cubic) phase of CsPbI_3 , it has not been possible to synthesize pure CsPbI_3 NCs through this room temperature method.

In this chapter, we demonstrate a facile room temperature synthesis method of full inorganic CsPbX_3 ($\text{X}=\text{Cl}$, Br , I) NCs using a single solvent, toluene. Through this method, CsPbX_3 NCs with superior colloidal stability could be synthesized within 10 min. The synthetic scheme developed here is more straightforward, more environmental friendly and less time-consuming than those reported previously. It is also the first time, to the best of our knowledge, that pure iodide based cesium lead halide perovskite NCs have been directly synthesized at room temperature.

2.2 Experimental Section

Materials: All the chemicals were obtained from Sigma Aldrich and used as received without further purification. CsAc (Cesium Acetate, 99.9%), $\text{PbAc}_2 \cdot 3\text{H}_2\text{O}$ (Lead Acetate, 99.99%), HCl acid (Hydrochloric, 37wt.% in water), HBr acid (Hydrobromic acid, 48wt.% in water), HI acid (Hydroiodic acid, 57wt% in water, $\leq 1.5\%$ hypophosphorous acid as stabilizer) and TOL (Toluene, 99.8%).

Synthesis of CsPbX_3 ($\text{X}=\text{Cl}$, Br and I) NCs: Equimolar amounts of CsAc and PbAc_2 with a varying amount of Oleic Acid (OA) and Oleylamine (OLAM) were stirred in 5 mL toluene at room temperature (~ 293 K). A colorless transparent solution was achieved after 5 minutes. Subsequently the halide acid solution in water was added under vigorous stirring. After further stirring for 5 min, the resulting strong luminescent NCs-contained solution

were centrifuged at low speed to remove any big particles and acid introduced water that collects at the bottom because of the higher density.

For the synthesis of mixed-halide NCs an additional partial anion exchange step is used. The anion-exchange reactions were done by mixing a desired halide acid and NCs solution corresponding to designed mole ratio of the different halides.

In a typical synthesis, 0.1 mmol of CsAc and 0.1 mmol of $\text{PbAc}_2 \cdot 3\text{H}_2\text{O}$ were mixed in 5 ml TOL and stirred with 0.1 ml OA and 0.01 ml OLAM to get a clear solution. 0.01 ml HBr acid was injected under vigorous stirring. The formation of CsPbBr_3 NCs was followed through the observation of a strong green emission under excitation with 365 nm UV lamp.

Characterization

X-ray diffraction (XRD) patterns were recorded by using a PW 1729 Philips diffractometer, operating at 40 kV and 20 mA and using $\text{Cu K}\alpha$ radiation ($\lambda = 1.5418 \text{ \AA}$). For XRD analysis, the sample plates were prepared by depositing the NCs colloidal solution on the silicon wafer and evaporating the solvent under vacuum. Aluminum holder was used as sample holder for silica coated NCs. Crystal structures were produced by visualization for electronic and structural analysis (VESTA).¹⁴

Absorption spectra were obtained with a double beam Perkin-Elmer Lambda 950 UV/VIS/IR spectrophotometer. Excitation and emission spectra and photoluminescence (PL) decay curves were measured by an Edinburgh Instruments FLS920 spectrofluorimeter equipped with a 450 W Xenon lamp as excitation source and a 0.22 m double grating monochromator for excitation (Bentham DTMS300, 1200 lines/mm grating, blazed at 300 nm for excitation). Emission spectra (400-850 nm) were recorded with a single 0.22 m monochromator (500 nm blazed grating) and the emitted light was detected by a Hamamatsu R928 photomultiplier tube (PMT). Decay curves of the CsPbX_3 NCs emission were recorded in the same set-up using an Edinburgh Instruments diode laser with an excitation wavelength of 376.8 nm (65 ps pulse width, 0.2-20 MHz repetition rate) and a fast Hamamatsu H74220-02 PMT for light detection. The samples for optical analysis were prepared by dissolving the crude NCs mixture in toluene and transferring the solution to the quartz cuvette.

Transmission electron microscopy (TEM) images were made with a FEI TECNAI T12,

operating at 120 kV. The samples for TEM imaging were prepared by dipping a carbon-coated copper mesh TEM grid into a toluene solution of NCs. The excess liquid were evaporated under vacuum.

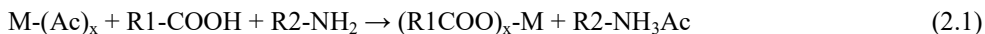
2.3 Results and Discussion

Synthesis of CsPbX₃ (X= Cl, Br and I) NCs

To illustrate the synthesis and discuss the mechanism for the formation of CsPbX₃ NCs we will use CsPbBr₃ NCs as an example. The synthesis of CsPbCl₃ and CsPbI₃ NCs is largely analogous. Equimolar amounts of CsAc and PbAc₂ with a varying amount of oleic acid (OA) and oleylamine (OLAM) were stirred in 5 mL toluene at room temperature (~293 K). A colorless transparent solution was achieved after 5 minutes. Subsequently the halide acid solution in water (HCl, HBr or HI for CsPbCl₃, CsPbBr₃ or CsPbI₃ NCs, respectively) was added under vigorous stirring.

For the synthesis of CsPbX₃ NCs in toluene the first challenge is to obtain stable Cs- and Pb-precursor solutions in toluene. Stirring of solely the Cs-acetate (CsAc) or Pb-acetate (PbAc) precursors in toluene results in a white cloudy suspension and precursors precipitated at the bottom of the vial. Upon injection of HBr acid, the precursors do react forming large particles which precipitate out from the solution. Addition of either oleic acid (OA) or oleylamine (OLAM) does not result a clear solution. For a suspension with OA added, precipitation occurred immediately after addition of HBr acid. The yellow precipitate showed no emission under 365 nm excitation. Addition of OLAM gives a similar result, although weak luminescent products formed after addition of HBr acid. The PL and colloidal stability degraded within minutes. The XRD pattern clearly revealed that all the precipitate formed was CsPbBr₃ with the orthorhombic structure.

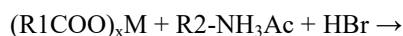
To obtain a clear precursor solution, both OA and OLAM were added. The synergetic effect of the combination of OA and OLAM is crucial to dissolve the precursors. A potential mechanism is given in the reaction scheme below (Equation 2.1):



in which M-(Ac)_x (x= 1 or 2) represents CsAc or PbAc₂. R1-COOH and R2-NH₂ are short hand notations of oleic acid and oleylamine, respectively. As indicated in Equation 2.1, a fraction of OA is deprotonated by OLAM resulting free oleate ligand. Metal acetate

combines with the free oleate ligand to form a dissolvable oleate-coordinated complex. The replaced acetate ligands combine with protonated oleylamines forming oleylammonium acetate.

Upon addition of HBr acid to the clear precursor solution rapid coloration of the solution is observed. Within seconds a green solution forms and no changes are observed at longer time scales. Under illumination with a UV-lamp the solution shows a bright green emission. These observations suggest the formation of CsPbBr₃ NCs. Further evidence for the formation of CsPbBr₃ NCs will be presented below. Equation 2.2 describes a possible reaction mechanism: addition of the acid causes the oleates in metal-oleate compounds to be partially or fully protonated and replacement of the oleate by bromide induces the formation of metal-bromide. This initiates the reaction between CsBr and PbBr₂ nanoclusters^{16,17} to form CsPbBr₃ NCs stabilized by organic ligands.



The synthesis of CsPbCl₃ QDs and CsPbI₃ QDs is completely analogous, except that 0.01 ml of a concentrated HCl or HI solution was added. It is also anticipated that this facile synthesis methodology is also applicable to synthesis of other perovskite NCs such as FAPbBr₃ NCs.

Characterization, Optical Properties and pH Stability

The luminescent products of the syntheses described in above-mentioned sections were analyzed using transmission electron microscopy (TEM), x-ray diffraction (XRD) and (time-resolved) luminescence spectroscopy. The XRD patterns of synthesized NCs are shown in the Figure 2.1a. The diffraction patterns show the characteristic cubic perovskite structure and from Cl⁻ to I⁻, the diffraction peaks shift to smaller angles which is consistent with the expansion of the crystal lattice due to the increasing ionic radius from Cl⁻ to Br⁻ to I⁻.

The TEM images of the products are shown in the Figure 2.1(b-d). Most of the particles have a cubic shape which reflects the underlying symmetry of the crystal lattice. It can also be seen that as-prepared NCs self-organize to a two-dimensional structure which indicates a small size dispersion. The size of typical NCs is 10 nm for CsPbCl₃ NCs, 12 nm for

CsPbBr₃ and 13 nm for CsPbI₃ NCs.

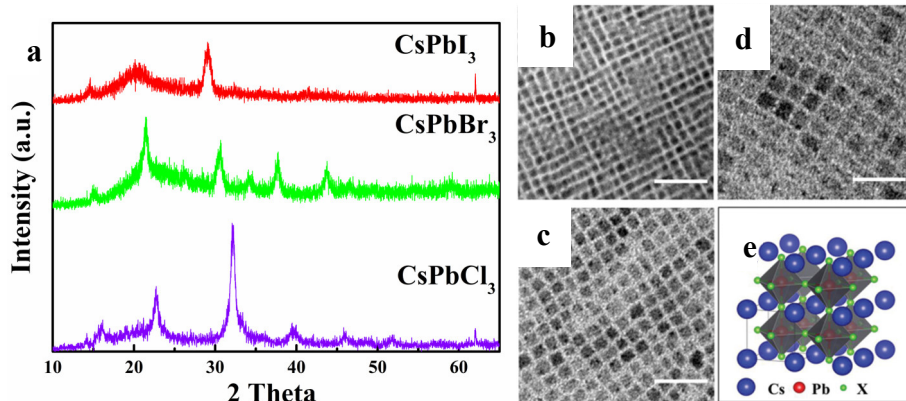


Figure 2.1. XRD patterns of NCs and TEM Images of as-synthesized CsPbX₃ NCs. (a) XRD pattern of as-prepared NCs. (b, c, d) TEM images of as-prepared CsPbX₃ (X = Cl, Br, I) NCs. (e) Illustration of perovskite lattice for the cubic phase.

Variations in the synthesis protocol did not lead to significant variation of size. The slight increase in size from Cl⁻ to Br⁻ to I⁻ can have different reasons. As discussed above, a nucleation burst will occur after injection of halide acid. The transportation of halide ions from the water phase to the toluene phase is crucial for the NCs' formation. Furthermore, the monomers' depletion rate is also a key factor for controlling the growth of NCs. Variations in the kinetics for this process for the different halides can affect the final particle size. In addition, the increase in ionic radius from Cl⁻ to Br⁻ to I⁻ will also contribute to a larger NC size. The fast crystallization does not allow a full understanding of the growth process and factors influencing the final particle size. Further research is still needed.

The appearance and photoluminescence (PL) properties of different samples are shown in Figure 2.2. The emission peak of pure Cl⁻ to Br⁻ to I⁻ based NCs are located at 400 nm, 520 nm and 680 nm, respectively. The FWHMs increase from 20 nm to 35 nm as halide ion changes from Cl to I. The Stokes shifts of the emission are small: around 400 cm⁻¹ for all

CsPbX₃ NCs. Both emission and absorption of NCs red shift when anion changes from Cl⁻ to I⁻, reflecting the reducing of the exciton energy from Cl⁻ to I⁻.¹³

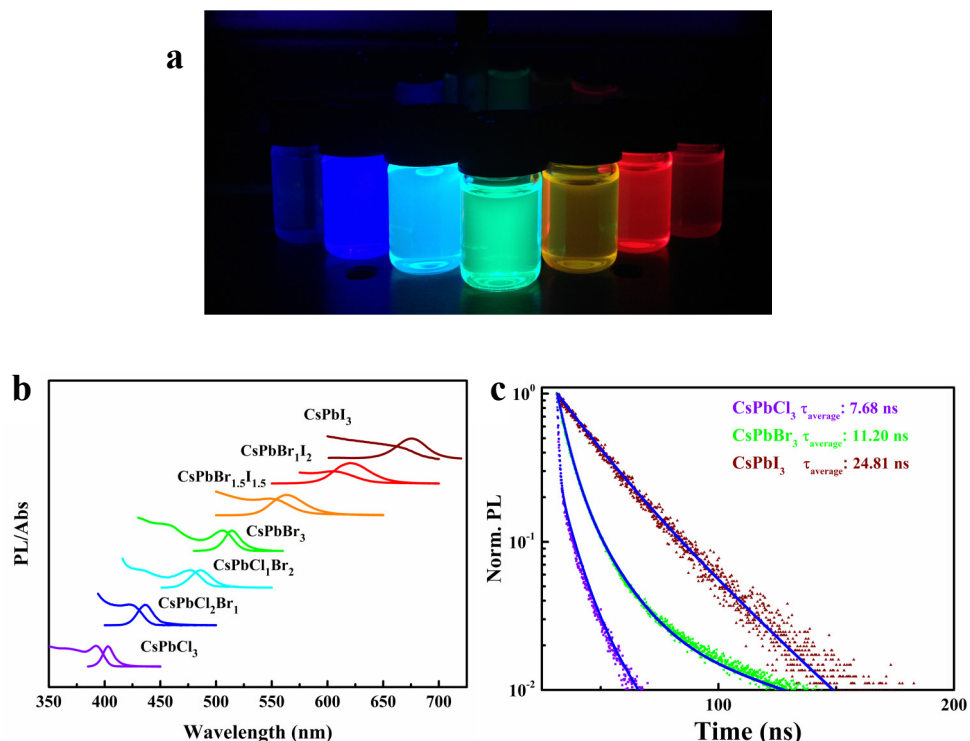
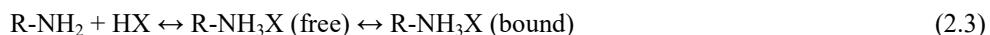


Figure 2.2. Photoluminescence spectra of CsPbX₃ (X= Cl, Br, I) NCs at 297 K. (a) Digital image of CsPbX₃ (X= Cl, Br, I) NCs ($\lambda_{\text{ex}}= 365$ nm) and mixed halide NCs under 365 nm UV excitation. (b) Optical absorption and emission of CsPbX₃ NCs ($\lambda_{\text{ex}}= 365$ nm). (c) time-resolved PL decays for single halide based NCs ($\lambda_{\text{ex}}= 365$ nm, $\lambda_{\text{em}}= 410$ nm (X=Cl), 520 nm (X=Br) or 680 nm (X=I)).

The luminescence decay curves of the emission from the pure Cl⁻ to Br⁻ to I⁻ NCs are shown in the Figure 2.2c. The luminescence decay is not purely single exponential but a good agreement with experiment is obtained by a bi-exponential fit. The average lifetime is 7.68

ns for CsPbCl₃, 11.20 ns for CsPbBr₃ and 24.81 ns for CsPbI₃. For these highly luminescent CsPbX₃ NCs the decrease in radiative decay rate for the heavier halide ion NCs can be partly explained by Fermi's golden rule which predicts a slower spontaneous emission rate for lower energy (longer wavelength) emission.

An important issue which hampers application of lead halide perovskites NCs, both in solar cells and light emitting devices, is the limited stability. CsPbX₃ NCs are not stable when exposed to air or polar solvents. For example, 0.15 mmol of hot-injection-synthesized NCs in 5 ml toluene will lose their PL, colloid stability and their structural integrity immediately after mixing with 0.5 ml of a polar solvent such as water. However, in the present synthesis, as much as 0.5 ml halide acid (water content is 0.4 ml in HCl, 0.387 ml HBr and 0.365 ml HI) was added to 5 ml toluene with 0.1 mmol precursor and the quantum dots formed instantaneously. During the subsequent 30 minutes of stirring, there was no sign of significant degradation in spite of the presence of water. To understand the superior stability, the degradation mechanism has to be considered. Hens et al. reported on the highly dynamic nature of the surface of CsPbBr₃ NCs and ascribed the loss of structural integrity to the desorption of surface ligands.¹⁵ When looking at the ligand molecules on the surface of NCs, there are two types of surface binding species, oleylammonium halide and oleylammonium oleate. Those ligands are in dynamic equilibrium between bound and free state. When a polar solvent is added, the loss of bound surface ligands proceeds rapidly and results in the disintegration of NCs. Addition of halide acid provides a high concentration of protons and halide ions and is responsible for the formation of tightly bound ligands which enhances the colloidal stability of NCs. Specifically, if we consider the equilibrium represented below (Equation 2.3), it can be seen that the addition of halide acid (HX) shifts the equilibrium to the direction of tightly bound ligands, which protects NCs from the polar solvent.



To further characterize the colloidal stability of perovskite NCs in polar solvents, 0.1 ml of freshly made crude solution of CsPbBr₃ NCs was diluted with 2 ml toluene was mixed with HBr acid solution with different pH (pH ranges from 7 to 2, with water content kept fixed at 2 ml). To measure the variation of the emission intensity as function of time and pH value in this system it is important to create a homogeneous suspension between toluene and acid or water to prevent phase separation and variations in emission intensity when

emission from NCs in one of segregated phases dominates. In a typical quartz cuvette ($H \times W \times D$: 56 mm \times 12.5 mm \times 12.5 mm), it is difficult to achieve a homogeneous suspension within a short period. This difficulty can be avoided by using glass vial with a 28 mm diameter and 61 mm height which allows for an efficient mixing.

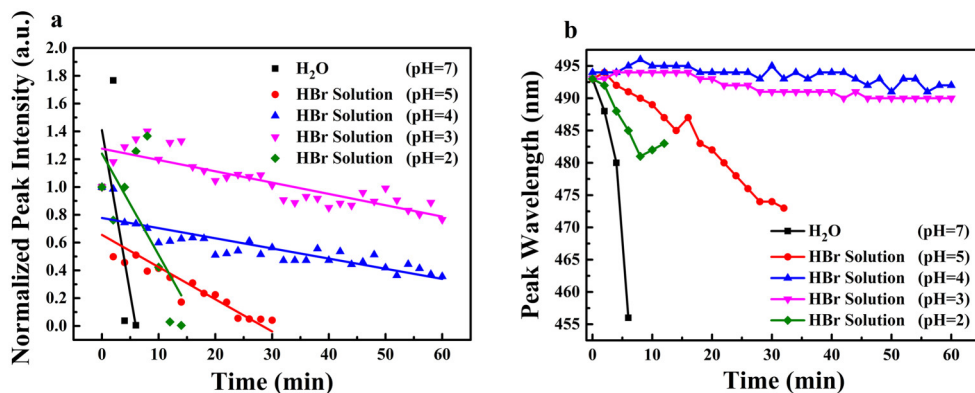


Figure 2.3 PL Intensity evolution with time for CsPbBr₃ NCs (a) mixture of 0.1 ml crude NCs solution 2 ml toluene and HBr acid of different pH value (pH: 7~2, with water content fixed at 2 ml). (b) peak wavelength evolution.

Photoluminescence (PL) intensities were corrected for the background signal and spectrofluorometer artifacts by measuring 2 ml toluene in 2 ml water in a vial as a blank sample. CsPbBr₃ NCs which emit at 500 nm were chosen to conduct the experiment. Emission spectra were taken every two minute for all NCs-Acid combination. During the interval between measurements the mixture was vigorously stirred to ensure a sufficient mixing of toluene and acid solution. After the stirring, in order to avoid the disturbance of PL from the phase separation, the vial was left undisturbed for 1 min and after that the PL was measured again. The emission intensity as a function of time and pH is presented in Figure 2.3. An initial enhancement on PL of sample was observed on sample pH=2 and pH=3 which was attributed to the formation of perovskite hydrate, providing further passivation of NCs' surface thus improving the quantum yield¹⁶. The PL decreasing was

observed on all the samples, however, with different rate. As expected, at pH 7.0 (DI water), a rapid and complete quenching of the emission of NCs can be observed within minutes accompanied by a gradual blue shift of PL indicating a shrinking of the NCs originating from dissolution. With decreasing pH, a systematic increase of the final PL intensity is clearly seen in Figure 2.3. However, upon further decreasing the pH value, the etching effect caused by H^+ ions starts to dominant and causes a detrimental effect on the PL. The complete decoloring of the toluene layer for a pH=2 acid was observed after ~4 min. Our result demonstrate the pH dependent stability of $CsPbX_3$ NCs, providing new insights into avenues to improve their stability in contact with polar solvents.

2.4 Conclusions

A DMF-free facile and fast one-pot room temperature synthesis method of $CsPbX_3$ ($X=Cl, Br, I$) NCs is reported. In toluene, strong luminescent $CsPbX_3$ NCs can be obtained within 10 min by addition of a small volume of a concentrated HX solution to a clear Cs^+ and Pb^{2+} precursor solution. By varying the halide composition in the NCs almost the full visible range (violet to red) can be covered by highly efficient $CsPbX_3$ NCs. The NCs have improved stability in the presence of water and the origin of enhanced stability of NCs is ascribed to the formation of a stable ligand shell because of the high halide concentration.

References

1. Grätzel, M., The Light and Shade of Perovskite Solar Cells. *Nat. Mater.*, 2014, *13*, 838-842.
2. Stoumpos, C. C.; Kanatzidis, M. G., The Renaissance of Halide Perovskites and Their Evolution as Emerging Semiconductors. *Acc. Chem. Res.*, 2015, *48*, 2791-2802.
3. Stranks, S. D.; H. J. Snaith, Metal-Halide Perovskites for Photovoltaic and Light-emitting Devices. *Nat. Nanotechnol.*, 2015, *10*, 391-402.
4. Kojima, A.; Teshima, K.; Shirai, Y.; Miyasaka, T., Organometal Halide Perovskites as Visible-Light Sensitizers for Photovoltaic Cells. *J. Am. Chem. Soc.*, 2009, *131*, 6050-6051.
5. Im, J.H.; Lee, C. R.; Lee, J. W.; Park, S. W.; Park, N. G., 6.5% Efficient Perovskite Quantum-dot-sensitized Solar Cell. *Nanoscale.*, 2011, *3*, 4088-4093.
6. Jeon, N. J.; Noh, J. H.; Yang, W. S.; Kim, Y. C.; Ryu, S.; Seo, J.; Seok, S. I., Compositional Engineering of Perovskite Materials for High-performance Solar Cells. *Nat.*, 2015, *517*, 476-480.
7. Kazim, S.; Nazeeruddin, M. K.; Gratzel, M. Ahmad, S., Perovskite as Light Harvester: a Game Changer in Photovoltaics. *Angew. Chem. Int. Ed.*, 2014, *53*, 2812-2824.
8. Tan, Z. K.; Moghaddam, R. S.; Lai, M. L.; Docampo, P.; Higler, R.; Deschler, F.; Sadhanala, M. A.; Pazos, L. M.; Credgington, D.; Hanusch, F.; Bein, T.; Snaith, H. J. Friend, R. H., Bright Light-emitting Diodes Based On Organometal Halide Perovskite. *Nat. Nanotechnol.*, 2014, *9*, 687-692.
9. Kim, J. Y.; Voznyy, O.; Zhitomirsky, D.; Sargent, E. H., 25th Anniversary Article: Colloidal Quantum Dot Materials and Devices: a Quarter-Century of Advances. *Adv. Mater.*, 2013, *25*, 4986-5010.
10. Mello Donega, C. de; Liljeroth, P.; Vanmaekelbergh, D., Physicochemical Evaluation of the Hot-Injection Method, a Synthesis Route for Monodisperse Nanocrystals. *Small*, 2005, *1*, 1152-1162.
11. Zhang, F.; Zhong, H.; Chen, C.; Wu, X.; Hu, X.; Huang, H.; Han, J.; Zou, B.; Dong, Y., Brightly Luminescent and Color-Tunable Colloidal $\text{CH}_3\text{NH}_3\text{PbX}_3$ ($X = \text{Br, I, Cl}$) Quantum Dots: Potential Alternatives for Display Technology. *ACS Nano*, 2015, *9*, 4533-4542.
12. Li, X.; Wu, Y.; Zhang, S.; Cai, B.; Gu, Y.; Song, J.; Zeng, H., CsPbX_3 Quantum Dots for Lighting and Displays: Room Temperature Synthesis, Photoluminescence Superiorities, Underlying Origins and White Light-Emitting Diodes. *Adv. Funct. Mater.*, 2016, *26*,

2435-2446.

13. Protesescu, L.; Yakunin, S.; Bodnarchuk, M. I.; Krieg, F.; Caputo, R.; Hendon, C. H.; Yang, R. X.; Walsh, A.; Kovalenko, M. V., Nanocrystals of Cesium Lead Halide Perovskites (CsPbX_3 , X = Cl, Br, and I): Novel Optoelectronic Materials Showing Bright Emission with Wide Color Gamut. *Nano Lett.*, 2015, 15, 3692-3696.
14. Momma, K.; Izumi, F., VESTA 3 for Three-dimensional Visualization of Crystal, Volumetric and Morphology Data. *J. Appl. Crystallogr.*, 2011, 44, 1272-1276.
15. De Roo, J.; Ibáñez, M.; Geiregat, P.; Nedelcu, G.; Walravens, W.; Maes, J.; Martins, J. C.; Driessche, I. V.; Kovalenko, M. V.; Hens, Z., Highly Dynamic Ligand Binding and Light Absorption Coefficient of Cesium Lead Bromide Perovskite Nanocrystals. *ACS Nano*, 2016, 10, 2071-2081.
16. Eperon, G. E.; Habisreutinger, S. N.; Leijtens, T.; Bruijnaers, B. J.; van Franeker, J. J.; D. deQuilettes, W.; Pathak, S.; Sutton, R.; Grancini, G.; Ginger, D.; Janssen, R.; Petrozza, A.; Snaith, H. J., the Importance of Moisture in Hybrid Lead Halide Perovskite Thin Film Fabrication. *ACS Nano*, 2015, 9, 9380-9393.
17. Wang, H. C.; Lin, S. Y.; Tang, A. C.; Singh, B. P.; Tong, H. C.; Chen, C. Y.; Lee, Y. C.; Tsai, T. L.; Liu, R. S., Mesoporous Silica Particles Integrated with All-inorganic CsPbBr_3 Perovskite Quantum-dot Nanocomposites (MP-PQDs) with High Stability and Wide Color Gamut Used for Backlight Display. *Angew. Chem. Int. Ed.*, 2016, 55, 7924-7929.

Chapter 2

Chapter 3

Efficient and Stable Luminescence from Mn^{2+} in Core and Core-isocrystalline Shell CsPbCl_3 Perovskite Nanocrystals

Abstract

There has been a growing interest in applying CsPbX_3 ($X=\text{Cl, Br, I}$) nanocrystals (NCs) for optoelectronic application. However, research on doping of this new class of promising NCs with optically active and/or magnetic transition metal ions is still limited. Here we report a facile room temperature method for Mn^{2+} doping into CsPbCl_3 NCs. By addition of a small amount of concentrated HCl acid to a clear solution containing Mn^{2+} , Cs^+ and Pb^{2+} precursors, Mn^{2+} doped CsPbCl_3 NCs with strong orange luminescence of Mn^{2+} at ~ 600 nm is obtained. Mn^{2+} doped CsPbCl_3 NCs show the characteristic cubic phase crystal structure very similar to the undoped counterpart, indicating that the nucleation and growth mechanism are not significantly modified for the doping concentrations realized (0.1 at.% - 2.1 at.%). To enhance the Mn^{2+} emission intensity and to improve the stability of the doped NCs, isocrystalline shell growth was applied. Growth of an undoped CsPbCl_3 shell greatly enhanced the emission intensity of Mn^{2+} and resulted in lengthening the radiative lifetime of the Mn^{2+} emission to 1.4 ms. The core-shell NCs also show superior thermal stability and no thermal degradation up to at least 110°C which is important in applications.

3.1 Introduction

Doping transition metals (i.e. Mn^{2+} , Ni^{2+} , Co^{2+}) in nanoparticles has received significant research interest¹⁻⁴. Fascinating new properties (e.g. optical and magnetic) can be introduced by intentional incorporating dopant ions into nanoparticles. Mn^{2+} doped II-VI (CdSe, CdS, ZnSe) quantum dots (QDs), as a representative, have been studied extensively in recent years⁵⁻⁷. The intense luminescence of Mn^{2+} combined with the large absorption cross section of QDs make these Mn^{2+} doped II-VI quantum dots promising for a wide range of applications⁸⁻¹¹. For example, luminescent Mn^{2+} doped ZnSe QDs show emission that is detuned from the QDs' absorption making these highly luminescent QDs promising for application in solar cells¹¹. In addition, another interesting aspect of Mn^{2+} doped QDs is their unique magneto-optical behavior resulting from interaction of photo-generated charge carriers in the QDs with the high magnetic moment of Mn^{2+} ($3d^5$) ions^{12,13}.

Recently, all-inorganic CsPbX_3 ($X=\text{Cl}$, Br , I) perovskite nanocrystals have emerged as a very promising group of materials with nearly unity quantum yield in a broad spectral range covering the visible spectrum¹⁴⁻¹⁷. Particular attention is presently given to new synthesis routes for this group of materials aimed at a better control of their optical properties (emission color, efficiency) as well as the chemical and temperature stability¹⁸⁻²¹. A promising avenue to improve control over the optical properties is doping these NCs with luminescent ions but so far studies on doping of lead halide perovskite NCs with optically active ions are limited. Two recent papers reveal the possibility of doping Mn^{2+} with CsPbCl_3 NCs at elevated temperature (180 °C) via a hot-injection method^{22,23}. Here, we report an alternative synthesis method allowing successful synthesis of Mn^{2+} -doped CsPbCl_3 NCs at room temperature. Creating a high chemical potential for Mn^{2+} in solution by mixing a reactive Mn^{2+} precursor with a Cs^+ and Pb^{2+} precursor in toluene followed by the addition of a small amount of HCl acid, results in Mn^{2+} -doped CsPbCl_3 NCs showing intense yellow/orange emission. A thermodynamically controlled doping mechanism is proposed to explain the doping process. In a next step, an undoped CsPbCl_3 shell is grown which greatly enhances the luminescence quantum yield and stability of the doped CsPbCl_3 : Mn^{2+} NCs.

3.2 Experimental Section

Chemicals: All the chemicals were obtained from Sigma Aldrich and used as received without further purification. The chemicals' specifications are: CsAc (Cesium Acetate, 99.9%), $\text{PbAc}_2 \cdot 3\text{H}_2\text{O}$ (Lead Acetate, 99.99%), $\text{MnAc}_2 \cdot 4\text{H}_2\text{O}$ (Manganese Acetate, 99.9%), HCl acid (Hydrochloric, 37 wt.% in water).

Synthesis of Mn^{2+} doped CsPbCl_3 NCs: Equimolar amount of the acetates CsAc and PbAc_2 with a variable amount of MnAc_2 were stirred in 5 mL toluene at room temperature (~ 293 K) under N_2 atmosphere. Oleic Acid (OA) and oleylamine (OLAM) were chosen as ligands. A colorless clear solution was achieved after ~ 15 minutes of stirring. Subsequently, the HCl acid in water was added under vigorous stirring. A white suspension formed and the suspension was centrifuged at low speed (1500 rpm) to remove large particles, agglomerates and acid residues (water). The larger particles precipitated at the bottom of the vial. The supernatant which contains the NCs was collected and stored at 0°C for 15 min followed by centrifuging, now at a higher speed (3500 rpm) to precipitate the NCs. After removing the supernatant the NCs were re-dissolved in 3 ml toluene and centrifuged again at low temperature (0°C). The supernatant was discarded and followed by addition of 1 ml toluene, resulting in a stable colloidal dispersion of Mn^{2+} doped CsPbCl_3 NCs.

In a typical synthesis, 0.1 mmol of CsAc, 0.1 mmol of $\text{PbAc}_2 \cdot 3\text{H}_2\text{O}$ and 0.005 mmol MnAc_2 (5 at.%) were mixed in 5 ml toluene and stirred with 0.045 ml OA and 0.075 ml OLAM to get a clear solution. 0.1 ml of concentrated HCl acid was injected under vigorous stirring. The successful doping of CsPbCl_3 NCs was evidenced by the observation of the characteristic emission of Mn^{2+} under excitation with 365 nm UV lamp. The average chemical yield is around 70% and was determined by weighing the final reaction product and comparing this to the expected weight for 0.1 mmol of the product.

Shell Growth: For growth of an undoped CsPbCl_3 shell around the Mn^{2+} -doped NCs, a coating precursor solution was prepared by dissolving 0.01 mmol CsAc and PbAc_2 in 5 ml toluene with 0.01 ml OA and OLAM. Separately, a clear crude solution of NCs was made by re-dissolving dried Mn^{2+} doped CsPbCl_3 NCs (~ 0.01 mmol) and oleylammonium chloride (~ 0.01 mmol) in 1 ml toluene. To this crude solution, the coating precursor solution was slowly added. To achieve different shell thickness, the amount of coating solution was increased from 0 ml to 0.3 ml with the increment of 0.05 ml.

Characterization

A variety of techniques was used to characterize the doped CsPbCl₃ NCs and to investigate the doping process. To determine the crystal structure and phase purity, X-ray diffraction (XRD) patterns were recorded by using a PW 1729 Philips diffractometer, operating at 40 kV and 20 mA and using Cu K α radiation ($\lambda = 1.5418 \text{ \AA}$). For XRD analysis, the sample plates were prepared by evaporating the NCs films on the silicon wafer. Transmission electron microscopy (TEM) images were made with a FEI TECNAI T12, operating at 120 kV and a TalosTM F200X, operating at 200 kV. The samples for TEM imaging were prepared by dipping a carbon-coated copper mesh TEM grid into a toluene solution of NCs. The excess liquid was evaporated under vacuum. Elemental analysis was used to determine the Mn/Pb elemental ratio using a Perkin Elmer Optima 8300 Inductively Coupled Plasma-Optical Emission Spectrometer (ICP-OES). To this end, samples were dissolved in concentrated HCl acid overnight, followed by dilution with 5 % HNO₃ acid.

Absorption spectra were obtained with a double beam Perkin-Elmer Lambda 950 UV/VIS/IR spectrophotometer. Luminescence (emission and excitation) spectra and photoluminescence (PL) decay curves were measured using an Edinburgh Instruments FLS920 spectrofluorometer equipped with a 450 W Xenon lamp as excitation source and a 0.22 m double grating monochromator for excitation (Bentham DTMS300, 1200 lines/mm grating, blazed at 300 nm for excitation). Emission spectra (380-700 nm) were recorded with a single 0.22 m monochromator (500 nm blazed grating) and the emitted light was detected by a Hamamatsu R928 photomultiplier tube (PMT). Decay curves of the Mn²⁺ emission were recorded in the same set-up using the 3rd harmonic of a 10 Hz pulsed Nd:YAG laser as the excitation source (pulse width: 10 ns, $\lambda_{\text{ex}}=355 \text{ nm}$) and a Hamamatsu R928 photomultiplier tube (PMT) for light detection. The samples for optical analysis were prepared by dissolving the crude NCs mixture in toluene and transferring the solution to the quartz cuvette.

Photoluminescence quantum yield (PL QY) determination was done using Lumogen Red 305 with a PL QY 95% in toluene as a first reference. With this reference, the PL QY of CsPbBr_{1.5}I_{1.5} nanocrystals ($\lambda_{\text{em}}=598 \text{ nm}$) was determined under 443 nm excitation. Next, the PL QY of Mn²⁺ doped CsPbCl₃ NCs was determined by comparison with the second

reference (CsPbBr_{1.5}I_{1.5} nanocrystals) using 380 nm excitation. The absorption coefficient of all the samples was carefully tuned to range of 0.02~0.1.

3.3 Results and Discussion

Synthesis and Luminescence of CsPbCl₃: Mn²⁺ NCs

To investigate the formation of the CsPbCl₃ NCs, the reaction product was analyzed using a variety of techniques to determine size, crystal structure and chemical composition. In Figure 3.1a the x-ray diffraction (XRD) pattern for doped and undoped CsPbCl₃ NCs is shown. The XRD pattern shows a number of diffraction peaks at angles that are characteristic of the CsPbCl₃ perovskite structure. The position for diffraction peaks calculated from the unit cell parameters are marked by filled blue circles and match the position observed. There is no difference between the XRD pattern for the doped (nominal concentration: 10 at.% Mn, actual Mn²⁺ concentration ~1 at.%) and undoped CsPbCl₃ NCs. The width of the peaks reflects a small crystallite size. However, due to the close resemblance of diffraction peaks of tetragonal phase of CsPbCl₃ and cubic phase (Supporting Information, Figure S3.1) coupled with broadness of diffraction peaks, further study is still needed to confirm the phase of the product. To determine the size and size distribution, TEM images were recorded. Figure 3.1b shows TEM images of CsPbCl₃ NCs on a TEM grid that was dipped into a NCs' solution. On the grid, areas with a high density of NCs are observed where the NCs are ordered. It is believed that during evaporation of the solvent self-assembly of the cubic CsPbCl₃ NCs takes place resulting in the highly ordered pattern. From analysis of the size of NCs, an average size (length of the edge of squares) was determined to be 7 nm. In Figure S3.2 the size distribution obtained from the analysis of 100 NCs is shown (Supporting Information Figure S3.2 (C1)). For 7 nm CsPbCl₃ NCs, weak quantum confinement effects can be expected as the exciton Bohr radius in CsPbCl₃ is ~2.5 nm¹⁴. Elemental analysis was done to determine the actual Mn²⁺ concentration in the NCs as it is often observed that the fraction of dopant ions incorporated is lower than the nominal concentration of dopants added to the reaction mixture. A series samples was prepared with different nominal Mn²⁺ concentration (5 at.% to 25 at.%, relative to Pb²⁺). The Mn²⁺ concentrations in the CsPbCl₃: Mn²⁺ NCs after careful washing were determined with ICP-AES and the results are shown in Table S3.1 of the Supporting Information. The concentration of Mn²⁺ incorporated is about 10 times less than the

concentration in the reaction mixtures and seems to saturate around just above 2 at.% Mn^{2+} for the presently used synthesis protocol. The fraction of dopant ions incorporated is typically much lower than the nominal concentration added and is determined by kinetic and thermodynamic effects which are less favorable for incorporation of the chemically different dopant ion than for the host cation^{24,25}. For example, for Mn^{2+} incorporation in ZnSe NCs the actual Mn^{2+} concentration was found to be around 10% of the Mn^{2+} concentration added and to saturate at 3 at.% Mn^{2+} ²⁶. Similar observations have been reported for ZnS: Mn^{2+} ²⁷. Extensive research on Mn^{2+} incorporation in CdSe QDs has provided more insight into the role of both kinetic and thermodynamic factors controlling dopant incorporation and under extreme circumstances (very high Mn^{2+} concentration in the presence of extra host anions), concentration of 30 at.% Mn^{2+} were realized²⁸. It can be expected that with different synthesis methods also for CsPbCl_3 NCs higher Mn^{2+} doping levels are possible.

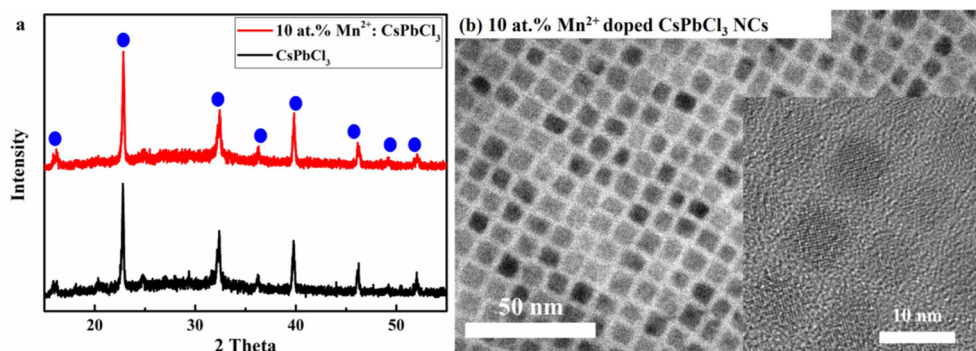


Figure 3.1. Structure characterization of as-prepared un-doped and Mn-doped CsPbCl_3 NCs. (a) XRD pattern of undoped and doped samples.(b) TEM image of Mn^{2+} (nominal concentration: 10 at.%, actual concentration \sim 1 at.%) doped CsPbCl_3 NCs.

The optical properties of the NCs were explored by recording emission and excitation spectra for CsPbCl_3 NCs doped with Mn^{2+} . Figure 3.2 shows the typical absorption, emission and excitation spectrum of Mn^{2+} (10 at.%) doped CsPbCl_3 NCs. In the emission

Chapter 3

spectrum, two distinctive peaks can be seen, namely, a narrow peak located at 405 nm with FWHM 11 nm and a broad band with a maximum around 600 nm. The narrow band at 405 nm is assigned to intrinsic exciton emission of CsPbCl₃ NCs while the broader emission peak at 600 nm (FWHM: ~100 nm) is assigned to a 3d⁵ intraconfigurational Mn²⁺ transition (⁴T₁→⁶A₁)^{2, 22, 23}. The excitation spectra of both the exciton emission at 405 nm and of the Mn²⁺ emission at 600 nm very closely follow the absorption spectrum. The spectra have a sharp onset at 400 nm followed by a first maximum around 385 nm, a weak second maximum around 360 nm and a third maximum around 337 nm. The fine structure observed is typical for nanoparticles where discrete energy levels that emerge at the band edges give rise to discrete transitions and fine structure in the absorption/excitation spectra. For the II-VI (e.g. CdSe) and IV-VI (e.g. PbSe) QDs this fine structure has been extensively investigated and theoretical calculations on peak positions and absorption strengths have been compared with experimental spectra to gain insight in the energy levels structure of the QDs. For the perovskite NCs, energy level calculations explaining the fine structure are in progress. The observation of the exciton absorption peaks in the excitation spectrum of the Mn²⁺ emission provides strong evidence for the incorporation of Mn²⁺ in the CsPbCl₃ NCs. Clearly, exciton absorption by the CsPbCl₃ NCs is followed by energy transfer to Mn²⁺ and bright yellow/orange emission from the Mn²⁺ ions. The fact that exciton to Mn²⁺ energy transfer is observed, shows the successful incorporation of Mn²⁺ in the CsPbCl₃ NCs.

It is interesting to investigate the incorporation mechanism for this room temperature synthesis. In the formation mechanism of NCs, ligands play an important role. To investigate the role of the ligands, we systematically varied the concentrations of both oleic acid (OA) and oleylamine (OLAM). Surface passivation by ligands is crucial and influences colloidal stability, quantum yield and doping efficiency. In the present case, a ligand combination of OA and OLAM is used. This is essential to obtain a clear solution of the precursors (CsAc, PbAc₂ and MnAc₂), which is important for achieving a stable colloidal solution of NCs. Furthermore, the long chained amine can play an important role in regulating the crystallization process of the NCs, while the steric repulsion provided by oleic acid is integral to preventing the irreversible coagulation. The presence of ligands is crucial in forming a stable colloidal solution of NCs. However, a stable bond between Mn²⁺ ions and ligands will hinder the effective incorporation of Mn²⁺. These considerations

reflect the trade-off between colloidal stability and successful incorporation of Mn^{2+} ions. To optimize the synthesis, the added volume of OA was varied from 0.015 ml to 0.125 ml while keeping the added volume of OLAM fixed at 0.015 ml and the added OLAM volume was varied from 0.015 ml to 0.15 ml while keeping the volume of OA fixed at 0.045 ml.

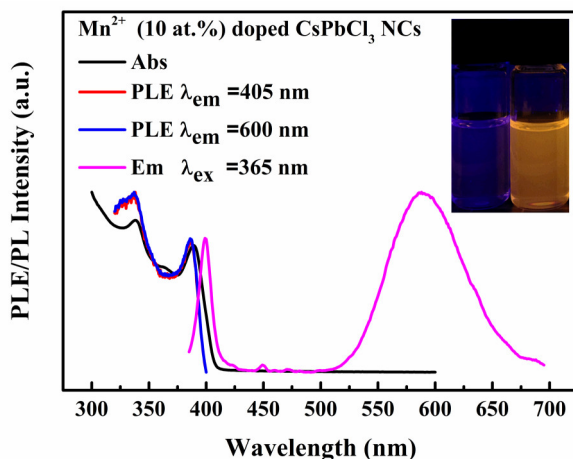


Figure 3.2. Absorption, excitation and emission spectrum of Mn^{2+} (10 at.% nominal concentration) doped CsPbCl_3 NCs. The inset shows a photograph of a vial with a colloidal dispersion of undoped (left) and Mn -doped (right) CsPbCl_3 sample under excitation of 365 nm UV light. The Mn^{2+} concentration indicated is nominal concentration, the actual Mn^{2+} concentration in the NCs is much lower (see Table S3.1 of the Supporting Information).

The variation of the emission spectra as a function of OA or OLAM volume are shown in Figure 3.3a and 3.3b. The results show a strong dependence of the relative Mn^{2+} emission intensity, especially on the OA concentrations. The relative intensity of the Mn^{2+} emission is expected to increase with Mn^{2+} concentration in the CsPbCl_3 NCs. The Mn^{2+} concentrations were determined using ICP and the results are collected in Table S3.1 of the Supporting Information. Indeed, the Mn^{2+} concentration shows the same trends as the Mn^{2+} emission intensity which means that a decrease in the Mn^{2+} emission intensity can be explained by a lower concentration on Mn^{2+} in the NC, except for the highest Mn^{2+}

Chapter 3

concentrations where concentration quenching starts to play a role (vide infra). For OA added volumes higher than 0.045 ml a very rapid decrease in the Mn^{2+} concentration is observed. The added volume of OLAM also affects the relative intensity of the Mn^{2+} emission. For an OA volume of 0.045 ml, the highest relative Mn^{2+} emission intensity is observed for 0.075 ml of OLAM.

To understand the variation in incorporation efficiency for different added OLAM/OA volumes the doping mechanism needs to be considered. Given the present reaction conditions, the doping resembles diffusion doping that was recently shown to be effective in incorporating Mn^{2+} in CdSe²⁹. This doping process is largely thermodynamically controlled. Dopant incorporation is driven by a high chemical potential of the dopant in solution which will be further internalized from the surface layer and subsequently diffuses inwards. In our synthesis, metal acetate salts are the initial metal precursors. When metal acetate salts are dissolved in toluene with oleic acid and oleylamine, acetate ligands will be replaced by oleate ligands and form dissolvable metal-oleate complexes. Initially, after addition of the hydrochloric acid, the carboxylate groups of the oleate ligand are protonated which results in a massive increase in the concentration of active metal monomers. Consequently, the chemical potential of metal ions (e.g. Cs^+ , Pb^{2+} , Mn^{2+}) in bulk solution is substantially increased and provides a strong driving force for the crystallization of CsPbCl_3 . In the presence of excess Cl^- (from the addition of concentrated HCl) a Cl^- surface layer allows for binding of Mn^{2+} to the surface, followed by inward diffusion. Given that there is an activation energy for inward diffusion, the Mn^{2+} incorporation is expected to be slow at room temperature and the Mn^{2+} concentration in the surface layer can be expected to be higher than in the core of the NCs.

Secondly, since the doping and crystallization process are initiated by protonation of metal-oleate complex, it is expected that H^+ ions are of prime importance to determine PL properties. The influence of varying volume of HCl added is depicted in Figure 3.3c. A strong increase in the Mn^{2+} emission intensity is observed when the volume of HCl acid increases from 0.01 ml to 0.1 ml. Increasing the concentration of H^+ will facilitate the formation of reactive metal monomer, resulting a higher chemical potential difference of metal ions in solution and nanocrystals. In addition, the higher Cl^- concentration will result in surface adsorption of Cl^- and adsorption of Mn^{2+} at the Cl^- rich surface will be followed by internalization of Mn^{2+} through cation diffusion. Thus, excess Cl^- will decrease the

chemical potential of dopant ions in the host lattice, enlarging the driving force for Mn^{2+} incorporation. Again, similar observations were made for Mn^{2+} diffusion doping of CdSe where the anion (Se^{2-}) concentration in solution was shown to be crucial for successful Mn^{2+} doping²⁹. With further increase of the amount of HCl acid, the emission intensity of Mn^{2+} decreases.

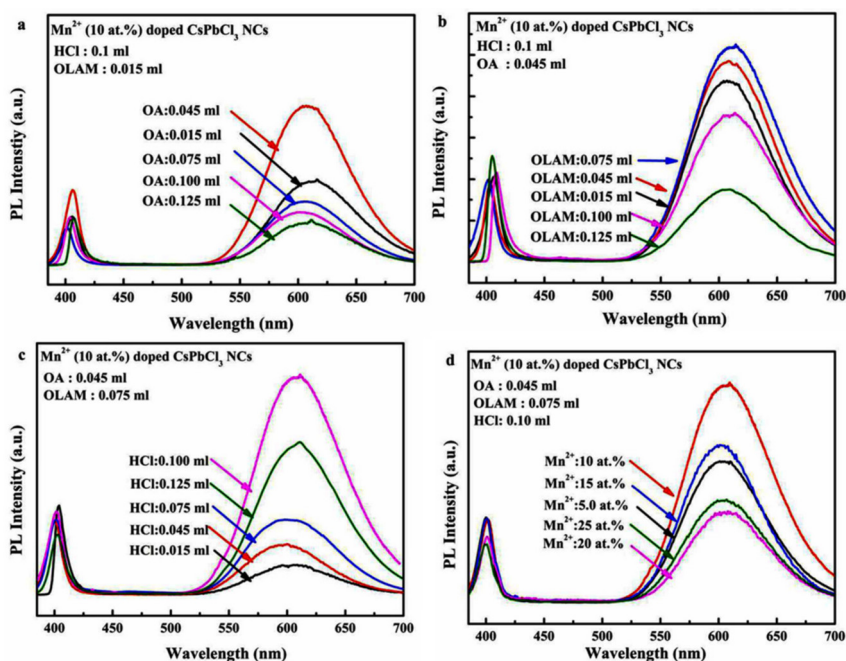


Figure 3.3. Emission spectrum of as-prepared $\text{CsPbCl}_3:\text{Mn}^{2+}$ NCs samples formed under different reaction conditions at 297 K. All spectra are normalized to the absorption at 365 nm which makes a direct comparison of the efficiencies of the emission possible. (a) PL emission spectrum as a function of OA volume ($\lambda_{\text{ex}}=365$ nm). (b) PL emission spectrum as a function of OLAM volume ($\lambda_{\text{ex}}=365$ nm). (c) PL emission spectrum as a function of HCl volume ($\lambda_{\text{ex}}=365$ nm). (d) Emission spectrum of Mn^{2+} doped CsPbCl_3 NCs with 5 at.%~25 at.% Mn^{2+} in the reaction mixture. The Mn^{2+} concentrations indicated are nominal concentration, the actual Mn^{2+} concentration in the NCs is much lower and depends strongly on the synthesis conditions (see Table S3.1 of the Supporting Information).

Chapter 3

The reduction of Mn^{2+} emission intensity suggests that H_2O from halide acid may affect the incorporation of Mn^{2+} while also the chemical stability of the NCs may be reduced at the highest HCl concentrations. The optimum concentration (under the presently optimized reaction conditions) is 0.10 ml of concentrated HCl.

Based on the observations discussed above, the optimized synthesis conditions for further NCs synthesis are HCl: 0.1 ml. OA: 0.045 ml and OLAM: 0.075 ml. The observation of Mn^{2+} emission indicates that energy transfer from the exciton to Mn^{2+} ions occurs. However, it still cannot rule out the possibility that a large fraction of the Mn^{2+} ions are only surface bound and not (statistically) incorporated in the nanocrystal lattice. The fact that for a 1~2 at.% Mn^{2+} content (on average 30~60 Mn^{2+} ions per CsPbCl_3 NC) still exciton emission is observed indicates that energy transfer to Mn^{2+} is not highly efficient. For Mn^{2+} in the center of the NC, where the exciton wavefunction has the higher amplitude, more efficient energy transfer is expected. The observation of exciton emission indicates that the concentration of Mn^{2+} is relatively higher closer to the surface of the NC where the overlap with the exciton wavelengths is weaker. The relative intensity of the exciton emission is observed to vary between samples that were prepared under identical conditions and is also affected by the washing procedure. The trends observed in Figure 3.3 are however reproducible and provide information on the optimum conditions for Mn^{2+} incorporation for the present synthesis protocol.

In order to further internalize surface bound dopant ions, surface passivation by isocrystalline core-shell (ICS) growth was adopted. Several reports have confirmed that solution epitaxial growth of additional layers of host material can efficiently internalize surface-bound dopant ions hence enhance the relative intensity of dopant emission³⁰⁻³². For growing a CsPbCl_3 -shell layer, 0.01 mmol of the purified Mn^{2+} doped CsPbCl_3 NCs was re-dispersed in 1 ml toluene. This was followed by slow addition of a specific volume of a solution consisting Pb^{2+} and Cs^+ precursors for overgrowth with a CsPbCl_3 shell under vigorous stirring. The samples obtained after additional shell growth will be referred to as Cx (x represent sample number, C1 is the original NCs without any modification, higher numbers correspond to a thicker shell). Figure 3.4 presents the evolution of PL QY of an as-prepared sample with that of NCs with different isocrystalline shell thickness. The details on PL QY determination can be found in experimental section. As can be seen from the Figure 3.4, a general trend of an increase in PL QY of the Mn^{2+} emission is observed

with increasing shell thickness. The highest PL quantum yield is measured for sample C7. The high PL QY (39 %) reflects successful incorporation of surface bound Mn^{2+} ions by overgrowth of a CsPbCl_3 shell. Successful growth of additional layers of CsPbCl_3 is also supported by a slight red shift of the exciton emission peak of CsPbCl_3 NCs (Supporting Information Figure S3.3). Additionally, the shape of the emission peak of CsPbCl_3 NCs is largely unaffected without any broadening. This confirms that the process of continued growth on existing CsPbCl_3 NCs is dominant (Supporting Information, Figure S3.3). TEM images of sample C1 and C7 were shown in Figure S3.2 and reveal a clear increase of average size of NCs after shell coating (from 7 nm to 8.5 nm). Further evidence for the beneficial influence of ICS growth on the luminescence efficiency can be obtained from luminescence lifetime measurements.

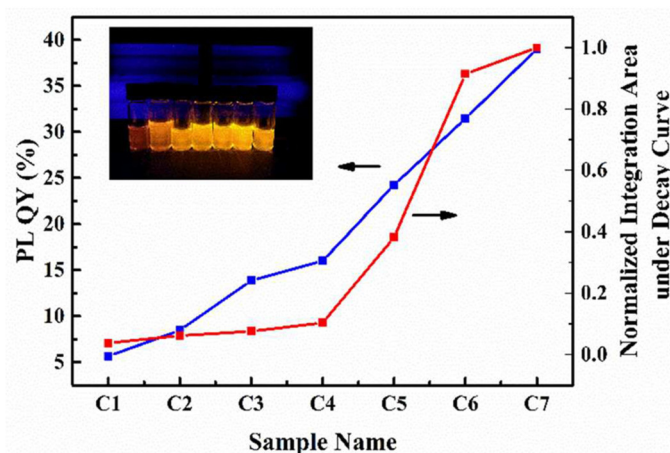


Figure 3.4. Effect of ICS growth on the relative PL QY and integrated area under the Mn^{2+} luminescence decay curves for Mn^{2+} doped CsPbCl_3 NCs. Blue line: evolution of PL QY as a function of shell thickness ($\lambda_{\text{ex}}=380$ nm). The inset shows a photograph of samples C1 to C7 (left to right) under excitation with a 365 nm UV lamp (Please note that of NCs concentration of each sample is different, decreasing from left to right). Red line: Evolution of integrated area under the Mn^{2+} emission decay curves for samples C1 to C7 ($\lambda_{\text{ex}}=355$ nm, $\lambda_{\text{em}}=600$ nm).

Chapter 3

Luminescence decay curves of the Mn^{2+} emission are shown in Figure S3.4 of the Supporting Information. The Mn^{2+} emission decay curve of the as-prepared samples do not show mono exponential decay behavior. A multi-exponential fitting has to be used and a bi-exponential fit gives a reasonably good agreement with lifetimes of 0.15 ms and 0.78 ms. Upon overgrowth of an additional CsPbCl_3 shell, a clear lengthening of the decay lifetime of the Mn^{2+} emission is observed. This is explained by a reduction of Mn^{2+} ions close to surface quenching sites. It is well-known that luminescent ions close to the surface experience faster decay as a result of energy transfer to surface defects. This results in a faster and also non-exponential decay as the non-radiative decay rate varies between luminescent ions at varying distances from quenching sites. A transformation of the Mn^{2+} emission decay curve from multi-exponential to mono exponential is observed as the undoped CsPbCl_3 layer thickness increases. This is consistent with efficient incorporation of Mn^{2+} ions by additional shell growth which effectively removes Mn^{2+} ions at the NC surface by overcoating with an undoped isocrystalline CsPbCl_3 shell. For the thickest CsPbCl_3 shell a mono exponential decay curve with a 1.4 ms decay time is observed. The 1.4 ms Mn^{2+} lifetime is the radiative life-time and is in the ms range that is expected for the spin- and parity-forbidden ${}^4\text{T}_1\text{-}{}^6\text{A}_1$ transition within the 3d^5 configuration of Mn^{2+} . The evolution of integration area under the decay curve, which is a good indicator for the relative PL QY, runs parallel to the PL QY determined by double reference method. The final PL QY of 40% is high and can possibly be further improved by optimizing the synthesis conditions. The high PL QY makes these Mn^{2+} doped NCs promising for application as efficient emitter in optical devices.

Thermal stability of NCs is another issue, especially for applications in high-power LEDs where on-chip phosphors reach temperatures between 150 and 200 °C. To gain insight on the quenching behavior of NCs with different shell thickness at elevated temperature, the thermal stability of C1- Mn^{2+} : CsPbCl_3 and C7- Mn^{2+} : CsPbCl_3 (both in toluene, boiling point: 111 °C) were tested using a thermal cycling experiment. By monitoring the luminescence intensity of the Mn^{2+} emission band for successive heating and cooling cycles, we studied the temperature dependent luminescent behavior. The thermal cycling experiment were conducted between 30 °C-110 °C. Emission spectra was taken every 10 °C under 365 nm illumination. During the measurement, the temperature of the sample was

gradually increased to 110 °C and allowed to cool down to 30 °C. Both heating and cooling were done in a controlled manner (heating and cooling rate: ~ 10 °C/min).

The temperature dependent luminescence characteristics of C1-Mn²⁺: CsPbCl₃ (no CsPbCl₃ shell) and C7-Mn²⁺: CsPbCl₃ (thickest CsPbCl₃ shell) are plotted in the Figure 3.5. Upon raising the temperature, the peak intensity of the uncoated CsPbCl₃: Mn²⁺ sample shows a continuous decrease (Figure 3.5a, emission spectra are shown in Figure S3.5), losing nearly 50% of peak intensity at 110 °C.

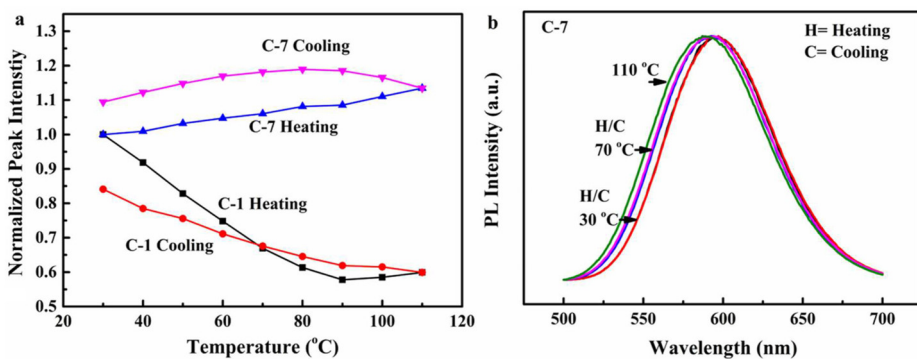


Figure 3.5. Temperature dependent PL behavior. (a) Peak emission intensity of sample C1-Mn²⁺: CsPbCl₃ NCs (no shell overgrowth) and C7-Mn²⁺: CsPbCl₃ NCs (overcoated) as a function of temperature. (b) Temperature dependent emission spectra for C7-Mn²⁺: CsPbCl₃ NCs

After the first heating cycle the uncoated CsPbCl₃: Mn²⁺ sample suffered a $\sim 15\%$ permanent peak intensity loss (see Fig. 3.5a). A much superior temperature stability is observed for the emission from the core-shell sample C7. A nearly constant PL intensity is observed when temperature varies from 30 °C to 110 °C (see also Figure 3.5a and Figure S3.6). In fact, a small increase in emission intensity is observed upon heating. This increase can be explained by thermal annealing of defects. Defects reduce the emission intensity. The non-equilibrium defect concentration, for example defects at the interface between the core and isocrystalline shell, can be reduced by annealing. A beneficial effects of annealing

is generally observed for (nano)crystalline luminescent materials and can explain the presently observed increase in emission intensity during and after the heat treatment. The superior thermal stability of the Mn^{2+} emission for the $\text{CsPbCl}_3:\text{Mn}^{2+}$ after overgrowth with an undoped CsPbCl_3 shell is explained by efficient passivation from thermally induced quenching sites located at the surface. Furthermore, it is also interesting to note a small shift of the emission wavelength of the Mn^{2+} emission during the heating cycle. As shown in Figure 3.5b, the emission shifts to higher energies (blue shift) when the temperature increases from 30 °C to 110 °C which is fully reversible upon cooling. The reason for the temperature dependent emission wavelength is lattice expansion at high temperature³³. Lattice expansion results in a larger Mn^{2+} -ligand distance and thus a smaller crystal field splitting. The $3d^5$ Tanabe-Sugano diagram shows that the emission maximum shifts to higher energies (shorter wavelengths) for stronger crystal fields. The stabilization of the doped CsPbCl_3 NCs is important for the applicability of ICS growth.

3.4 Conclusions

In summary, Mn^{2+} -doped CsPbCl_3 perovskite NCs were synthesized by a facile room temperature method. Following addition of a small volume of concentrated HCl acid to a clear solution containing Mn^{2+} , Cs^+ and Pb^{2+} precursors, monodisperse Mn^{2+} -doped CsPbCl_3 NCs showing bright orange Mn^{2+} emission were obtained. For the used doping levels (up to 25 at.% relative to Pb), no substantial changes of the NC size and shape were observed. Several important synthesis parameters, e.g. ligand volume and ratio, HCl volume and Mn^{2+} concentration, were optimized to achieve highly efficient Mn^{2+} emission. Overgrowth with an undoped CsPbCl_3 shell strongly improves the photoluminescence quantum yield of the Mn^{2+} emission (up to 40%) and also improves the thermal stability (no thermal quenching up to 110 °C). Overall, the presently reported room temperature synthesis method enables us to achieve highly luminescent NCs and provides new insights in the development of new doping strategies for perovskite NCs.

References

1. Karan, N. S.; Sarma, D. D.; Kadam, R. M.; Pradhan N., Doping Transition Metal (Mn or Cu) Ions in Semiconductor Nanocrystals. *J. Phys. Chem. Lett.*, 2010, *1*, 2863-2866.
2. Suyver, J. F.; Wuister, S. F.; Kelly, J. J.; Meijerink, A., Synthesis and Photoluminescence of Nanocrystalline ZnS: Mn²⁺. *Nano Lett.*, 2001, *1*, 429-433.
3. Singh, N.; Charan, S.; Sanjiv, K.; Huang, S.; Hsiao, Y.; Kuo, C.; Chien, F.; Lee, T.; Chen, P., Synthesis of Tunable and Multifunctional Ni-doped near-Infrared QDs for Cancer Cell Targeting and Cellular Sorting. *Bioconjugate Chem.*, 2012, *23*, 421-430.
4. Song, E.; Ye S.; Liu T.; Du P.; Si R.; Jing X.; Ding S.; Peng M.; Zhang, Q.; Wondraczek, L., Tailored near-Infrared Photoemission in Fluoride Perovskites Through Activator Aggregation and Super-Exchange Between Divalent Manganese Ions. *Adv. Sci.*, 2015, *2*, 1500089-1500097.
5. Pradhan, N.; Battaglia, D. M.; Liu, Y.; Peng, X., Efficient, Stable, Small, and Water-Soluble Doped ZnSe Nanocrystal Emitters as Non-cadmium Biomedical Labels. *Nano Lett.*, 2007, *7*, 312-317
6. Beaulac, R.; Archer, P. I.; Ochsenein, S. T.; Gamelin, D. R., Mn²⁺-Doped CdSe Quantum Dots: New Inorganic Materials for Spin-electronics and Spin-photonics. *Adv. Funct. Mater.*, 2008, *18*, 3873-3891.
7. Ochsenein, S. T.; Feng, Y.; Whitaker, K. M.; Badaeva, E.; Liu, W. K.; Li, X.; Gamelin, D. R., Charge-Controlled Magnetism in Colloidal Doped Semiconductor Nanocrystals. *Nat. Nanotechnol.*, 2009, *4*, 681-687.
8. Zhou, R.; Li, M.; Wang, S.; Wu, P.; Wu, L.; Hou, X., Low-Toxic Mn-Doped ZnSe@ZnS Quantum Dots Conjugated with Nano-hydroxyapatite for Cell Imaging. *Nanoscale*, 2014, *6*, 14319-14325.
9. Wang, C.; Xu, S.; Wang, Y.; Wang, Z.; Cui, Y., Aqueous Synthesis of Multilayer Mn:ZnSe/Cu:ZnS Quantum Dots With White Light Emission. *J. Mater. Chem. C*, 2014, *2*, 660-666.
10. Xu, C.; Zhou, R.; He, W.; Wu, L.; Wu, P.; Hou, X., Fast Imaging of Eccrine Latent Fingerprints with Nontoxic Mn-doped ZnS QDs. *Anal. Chem.*, 2014, *86*, 3279-3283.
11. Erickson, C. S.; Bradshaw, L. R.; McDowall, S.; Gilbertson, J. D.; Gamelin, D. R.; Patrick, D. L., Zero-Reabsorption Doped-nanocrystal Luminescent Solar Concentrators. *ACS Nano*, 2014, *8*, 3461-3467.

Chapter 3

12. Magana, D.; Perera, S. C.; Harter, A. G.; Dalal, N. S.; Strouse, G. F., Switching-On Superparamagnetism in Mn/CdSe Quantum Dots. *J. Am. Chem. Soc.*, 2006, *128*, 2931-2939.
13. Ochsenbein, S. T.; Gamelin, D. R., Quantum Oscillations in Magnetically Doped Colloidal Nanocrystals. *Nat. Nanotechnol.*, 2011, *6*, 112-115.
14. Protesescu, L.; Yakunin, S.; Bodnarchuk, M. I.; Krieg, F.; Caputo, R.; Hendon, C. H.; Yang, R.; Walsh, A.; Kovalenko, M. V.; Nanocrystals of Cesium Lead Halide Perovskites (CsPbX₃, X = Cl, Br, and I): Novel Optoelectronic Materials Showing Bright Emission with Wide Color Gamut. *Nano Lett.*, 2015, *15*, 3692-3696.
15. Nedelcu, G.; Protesescu, L.; Yakunin, S.; Bodnarchuk, M. I.; Grotevent, M.; Kovalenko, M. V., Fast Anion-Exchange in Highly Luminescent Nanocrystals of Cesium Lead Halide Perovskites (CsPbX₃, X = Cl, Br, I). *Nano Lett.*, 2015, *15*, 5635-5640.
16. Li, X.; Wu, Y.; Zhang, S.; Cai, B.; Gu, Y.; Song, J.; Zeng, H., CsPbX₃ Quantum Dots for Lighting and Displays: Room Temperature Synthesis, Photoluminescence Superiorities, Underlying Origins and White Light-emitting Diodes. *Adv. Funct. Mater.*, 2016, *26*, 2435-2446.
17. Song, J.; Li, J.; Li, X.; Xu, L.; Dong, Y.; Zeng, H., Quantum Dot Light-emitting Diodes Based on Inorganic Perovskite Cesium Lead Halides (CsPbX₃). *Adv. Mater.*, 2015, *27*, 7162-7167.
18. Huang, H.; Chen, B.; Wang, Z.; Hung, T. F.; Susha, A. S.; Zhong, H.; Rogach, A. L., Water Resistant CsPbX₃ Nanocrystals Coated by Polyhedral Oligomeric Silsesquioxane and Their Use as Solid State Luminophores in All-perovskite White Light Emitting Devices. *Chem. Sci.*, 2016, *7*, 5699-5703.
19. Dastidar, S.; Egger, D. A.; Tan, L.; Cromer, S. B.; Dillon, A. D.; Liu, S.; Kronik, L.; Rappe, A. M.; Fafarman, A. T., High Chloride Doping Levels Stabilize the Perovskite Phase of Cesium Lead Iodide. *Nano Lett.*, 2016, *16*, 3563-3570.
20. Ramasamy, P.; Lim, D.; Kim, B.; Lee, S.; Lee, M.; Lee, J., All-inorganic Cesium Lead Halide Perovskite Nanocrystals for Photodetector Applications. *Chem. Commun.*, 2016, *52*, 2067-2070.
21. Zhang, X.; Lin, H.; Huang, H.; Reckmeier, C.; Zhang, Y.; Choy, W. C. H.; Rogach, A. L., Enhancing the Brightness of Cesium Lead Halide Perovskite Nanocrystal Based Green Light-Emitting Devices through the Interface Engineering with Perfluorinated Ionomer. *Nano Lett.*, 2016, *16*, 1415-1420.

Chapter 3

22. Liu, W.; Lin, Q.; Li, H.; Wu, K.; Robel, I.; Pietryga, J. M.; Klimov, V. I., Mn²⁺-Doped Lead Halide Perovskite Nanocrystals with Dual-color Emission Controlled by Halide Content. *J. Am. Chem. Soc.*, 2016, *138*, 14954-14961.
23. Parobek, D.; Roman, B. J.; Dong, Y.; Jin, H.; Lee, E.; Sheldon, M.; Son, D., Exciton-to-Dopant Energy Transfer in Mn-Doped Cesium Lead Halide Perovskite Nanocrystals. *Nano Lett.*, 2016, *16*, 7376-7380.
24. Erwin, S. C.; Zu, L.; Haftel, M. I.; Efros, A. L.; Kennedy T. A.; Norris, D. J., Doping Semiconductor Nanocrystals. *Nature*, 2005, *436*, 91-94.
25. Norris, D. J.; Efros, A. L.; Erwin, S. C., Doped Nanocrystals, *Science*, 2008, *319*, 1776-1779.
26. Suyver, J. F.; Wuister, S. F.; Kelly, J. J.; Meijerink, A., Luminescence of Nanocrystalline ZnSe: Mn²⁺, *Phys. Chem. Chem. Phys.*, 2000, *2*, 5445-5448.
27. Bol, A. A.; Meijerink, A., Luminescence Quantum Efficiency of Nanocrystalline ZnS: Mn²⁺. 1. Surface Passivation and Mn²⁺ Concentration, *J. Phys. Chem. B*, 2001, *105*, 10197-10202.
28. Barrows, C. J.; Chakraborty, P.; Kornowske, L. M.; Gamelin, D. R., Tuning Equilibrium Compositions in Colloidal Cd_{1-x}Mn_xSe Nanocrystals Using Diffusion Doping and Cation Exchange, *ACS Nano*, 2016, *10*, 910-918.
29. Vlaskin, V. A.; Barrows, C. J.; Erickson, C. S.; Gamelin, D. R., Nanocrystal Diffusion Doping. *J. Am. Chem. Soc.*, 2013, *135*, 14380-14389.
30. Bryan, J. D.; Gamelin, D. R., Doped Semiconductor Nanocrystals: Synthesis, Characterization, Physical Properties, and Applications. *Prog. Inorg. Chem.*, 2005, *54*, 47-126.
31. Rodríguez, R. M.; Geitenbeek, R.; Meijerink, A., Incorporation and Luminescence of Yb³⁺ in CdSe Nanocrystals. *J. Am. Chem. Soc.*, 2013, *135*, 13668-13671.
32. Zhao, Y.; Rabouw, F. T.; van Puffelen, T.; van Walree, C. A.; Gamelin, D. R.; de Mello Donegá, C.; Meijerink, A., Lanthanide-Doped CaS and SrS Luminescent Nanocrystals: A Single Source Precursor Approach for Doping. *J. Am. Chem. Soc.*, 2014, *136*, 16533-16543.
33. Suyver, J. F.; Kelly, J. J.; Meijerink, A., Temperature-Induced Line Broadening, Line Narrowing and Line Shift in the Luminescence of Nanocrystalline ZnS: Mn²⁺. *J. Lumin.*, 2003, *104*, 187-196.

Supporting Information

Chapter 3. Efficient and Stable Luminescence from Mn^{2+} in Core and Core-isocrystalline Shell $CsPbCl_3$ Perovskite Nanocrystals

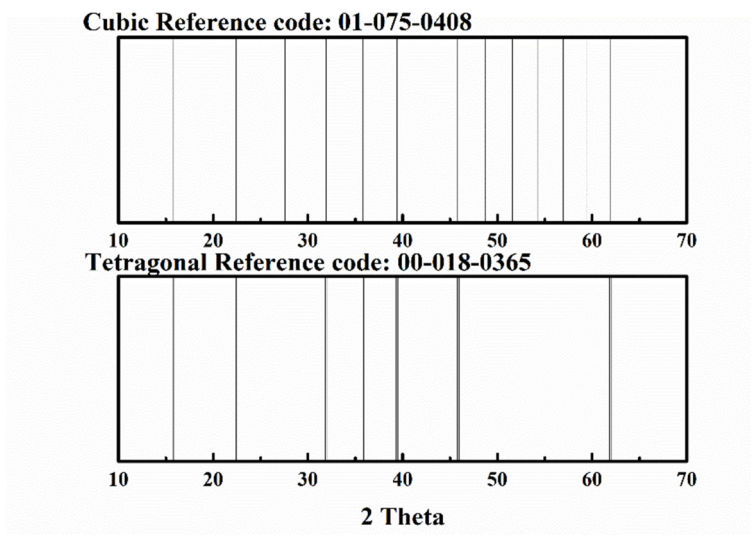


Figure S3.1. Standard XRD pattern of cubic phase and tetragonal phase of $CsPbCl_3$

Chapter 3

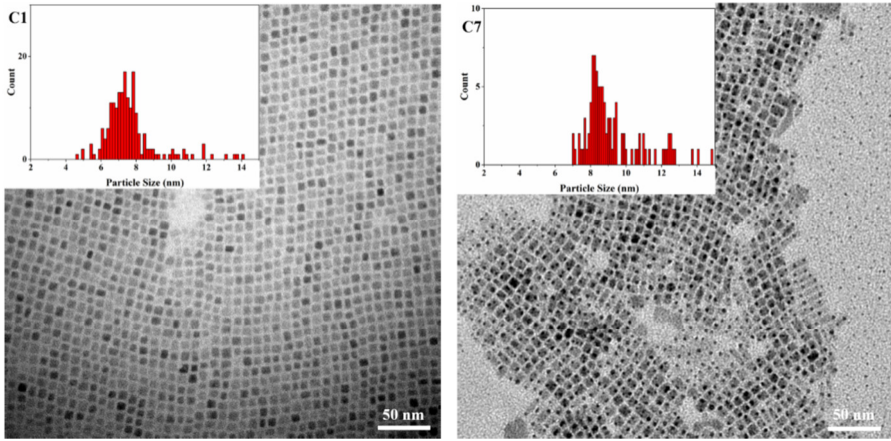


Figure S3.2. TEM image of sample C1 (uncoated) and C7 (after CsPbCl_3 overgrowth). The insets show corresponding size histogram.

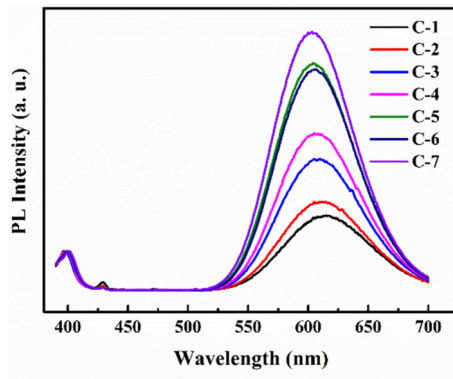


Figure S3.3. Emission spectra of $\text{CsPbCl}_3: \text{Mn}^{2+}$ quantum dots before (C1) and after shell growth with undoped CsPbCl_3 (C2 to C7, where the shell thickness increases from C2 to C7). All spectra are normalized to the exciton emission peak at 405 nm.

Chapter 3

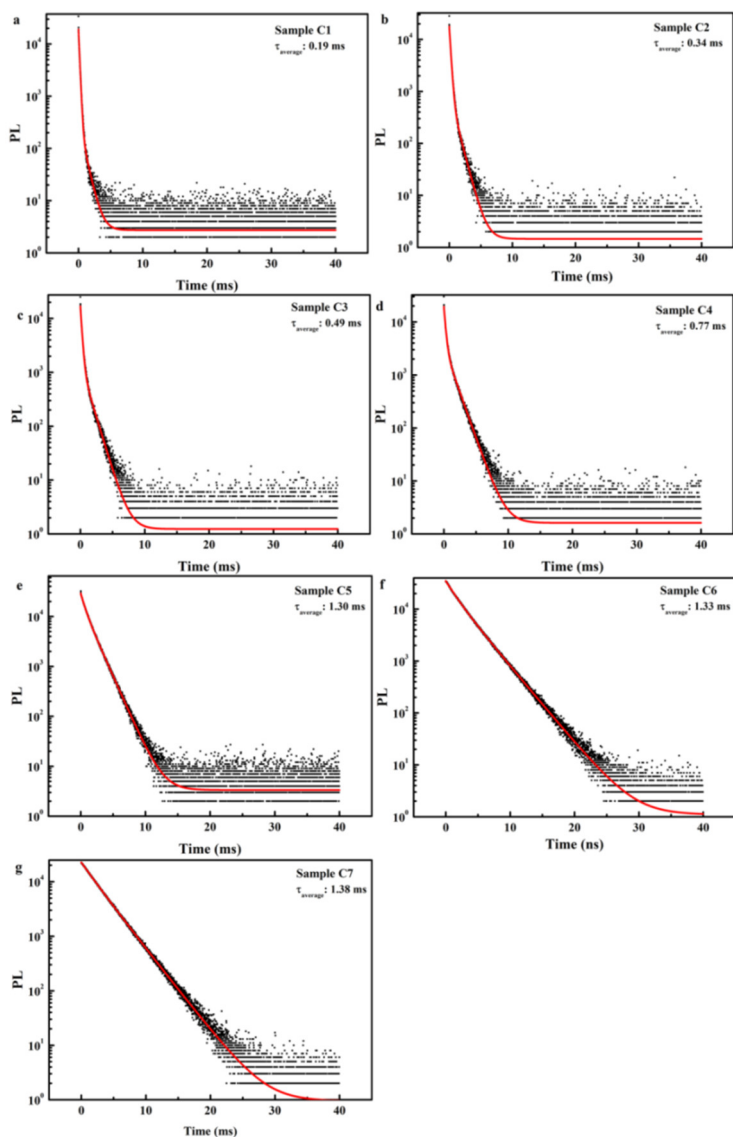


Figure S3.4. Luminescence decay curve for Mn²⁺-doped CsPbCl₃ QDs with different CsPbCl₃ shell thickness ($\lambda_{\text{ex}}=355$ nm, $\lambda_{\text{em}}=600$ nm, Red line: fit to bi-exponential decay or mono-exponential decay).

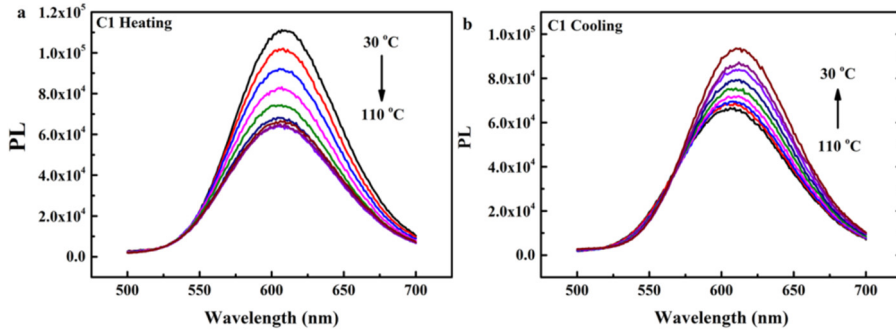


Figure S3.5. Temperature dependent emission spectra of $\text{CsPbCl}_3:\text{Mn}^{2+}$ before overcoating with undoped CsPbCl_3 (sample C1).

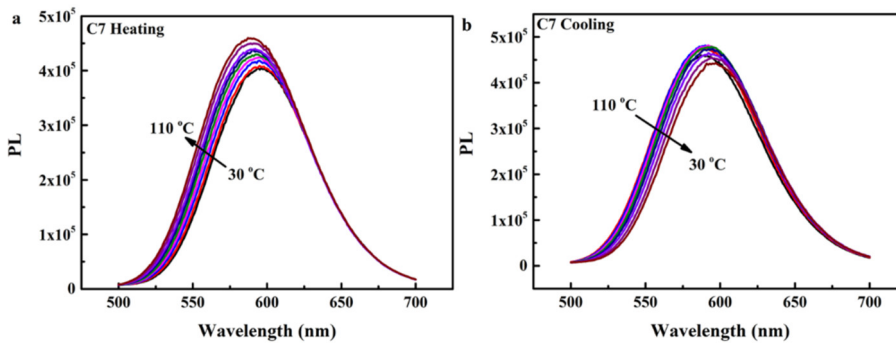


Figure S3.6. Temperature dependent emission spectra of $\text{CsPbCl}_3:\text{Mn}^{2+}$ after overcoating with undoped CsPbCl_3 (sample C7).

Chapter 3

Table S3.1. Elemental analysis (by ICP-OES) of samples made under different reaction conditions with different amounts of Oleic Acid (OA), Oleylamine (OLAM), HCl and Mn²⁺ precursor (see Figure 3.3 of the main text for the corresponding emission spectra).

Sample Name	Nominal concentration	doping	ICP ratio Mn/Pb
OA-1 (0.015 ml)	10 at.%		0.71 %
OA-2 (0.045 ml)	10 at.%		0.89 %
OA-3 (0.075 ml)	10 at.%		0.63 %
OA-4 (0.100 ml)	10 at.%		0.51 %
OA-5 (0.125 ml)	10 at.%		0.34 %
OLAM-1 (0.015 ml)	10 at.%		0.89 %
OLAM-2 (0.045 ml)	10 at.%		0.95 %
OLAM-3 (0.075 ml)	10 at.%		1.04 %
OLAM-4 (0.100 ml)	10 at.%		0.68 %
OLAM-5 (0.125 ml)	10 at.%		0.42 %

Chapter 3

Sample Name	Nominal concentration	doping	ICP ratio Mn/Pb
HCl-1 (0.015 ml)	10 at.%		0.11 %
HCl-2 (0.045 ml)	10 at.%		0.38 %
HCl-3 (0.075 ml)	10 at.%		0.45 %
HCl-4 (0.100 ml)	10 at.%		1.04 %
Mn-2	10 at.%		1.04 %
Mn-3	15 at.%		1.76 %
Mn-4	20 at.%		2.12 %
Mn-5	25 at.%		2.06%

Chapter 4

Tuning Exciton-Mn²⁺ Energy Transfer in Mixed Halide Perovskite Nanocrystals

Abstract

Doping nanocrystals (NCs) with luminescent activators provides additional color tunability for these highly efficient luminescent materials. In CsPbCl₃ perovskite NCs the exciton-to-activator energy transfer (ET) has been observed to be less efficient than in II-VI semiconductor NCs. Here we investigate the evolution of the exciton-to-Mn²⁺ ET efficiency as function of composition (Br/Cl ratio) and temperature in CsPbCl_{3-x}Br_x:Mn²⁺ NCs. The results show a strong dependence of the transfer efficiency on Br⁻ content. An initial fast increase in the relative Mn²⁺ emission intensity with increasing Br⁻ content is followed by a decrease for higher Br⁻ contents. The results are explained by a reduced exciton decay rate and faster exciton-to-Mn²⁺ ET upon Br⁻ substitution. Further addition of Br⁻ and narrowing of the host bandgap makes back transfer from Mn²⁺ to the CsPbCl_{3-x}Br_x host possible and leads to a reduction in Mn²⁺ emission. Temperature dependent measurements provide support for the role of back transfer as the highest Mn²⁺-to-exciton emission intensity ratio is reached at higher Br⁻ content at 4.2 K where thermally activated back transfer is suppressed. With the present results it is possible to pinpoint the position of the Mn²⁺ excited state relative to the CsPbCl_{3-x}Br_x host band states and predict the temperature and composition dependent optical properties of Mn²⁺-doped halide perovskite NCs.

4.1 Introduction

Lead halide perovskite NCs CsPbX_3 ($X=\text{Cl}, \text{Br}, \text{I}$) emerge as a promising class of materials for optoelectronic application because of their superb optical properties, e.g. high photoluminescence quantum yield (PL QY), short exciton life time, wide spectral tuning range covering the full visible spectrum and ease of preparation.¹⁻⁶ Incorporation of luminescent dopants (Mn^{2+} , lanthanides ions) has been reported recently and provides additional flexibility in tuning the optical properties for specific applications.⁷⁻¹² Of the particular interest is the dopant ion Mn^{2+} , whose efficient broad band emission is centred around ~ 600 nm and is detuned from the absorption of the perovskite host thus preventing reabsorption of the exciton emission which is important in e.g. solar cell applications. Recently, Mn^{2+} doped CsPbCl_3 NCs assisted solar cell have been successfully manufactured.^{13, 14}

Despite the extensive research¹⁵⁻¹⁷, the understanding of energy transfer between exciton and Mn^{2+} is still limited, especially the combined role of halide composition (Br/Cl ratio), Mn^{2+} content and temperature. Energy transfer (ET) from the exciton to Mn^{2+} is orders of magnitude slower than in Mn^{2+} -doped II-VI QDS ($\text{CdS}/\text{ZnS}:\text{Mn}^{2+}$) and even for high Mn^{2+} doping concentrations exciton emission from the perovskite host is still present.^{9,15,16,18} The inefficient ET has been attributed to the more ionic character of the perovskite NCs and the weaker confinement which reduces ET by wave function overlap. The influence of $\text{Cl}^- \leftrightarrow \text{Br}^-$ substitution on the ET is not extensively studied. In various reports, a decrease in the relative Mn^{2+} emission intensity was observed upon replacing Cl^- by Br^- .^{7, 19} The decrease can be explained by a narrowing of the bandgap which allows for back transfer from Mn^{2+} to the exciton state for higher Br^- content.⁷ Upon close inspection however, an initial increase in relative Mn^{2+} emission intensity is observed for low Br^- content, followed by a rapid decrease of the Mn^{2+} /exciton emission intensity ratio ($I_{\text{Mn}}/I_{\text{Exc}}$). Here we aim to gain further understanding of the exciton-to- Mn^{2+} ET in mixed $\text{CsPbCl}_{3-x}\text{Br}_x$ NCs and focus on systems with a relatively low Br^- content. Temperature (4.2 K-295 K) dependent emission of a series of Mn^{2+} -doped $\text{CsPbCl}_{3-x}\text{Br}_x$ ($x: 0 \sim 1.18$) NCs are reported. Upon anion exchange of Cl^- by Br^- we find two distinct regimes. In the first regime, where the exciton peak shifts from 405 to 420 nm, there is a strong increase in the Mn^{2+} to exciton emission intensity ratio with increasing Br^- content. The increase is explained by a reduced exciton decay rate combined with faster exciton-to- Mn^{2+} ET. In the second regime, further

replacement of Cl⁻ by Br⁻ leads to a continued exciton red shift from 420 to 440 nm but now accompanied by a marked decrease of the Mn²⁺/exciton intensity ratio. This decrease is explained by back-transfer from Mn²⁺ to exciton state because of narrowing of the bandgap resulting in overlap of Mn²⁺ excited states with host band states. In addition, the temperature dependence and decay kinetics of both exciton and Mn²⁺ emission have been measured and reveal a weaker temperature dependence of the exciton-to-Mn²⁺ ET efficiency than previously reported for pure CsPbCl₃:Mn²⁺ NCs.¹⁶ The present results provide important insight in the ET transfer dynamics of Mn²⁺ doped perovskite nanocrystals that will aid to optimize the ET and Mn²⁺ luminescence efficiency.

4.2 Experimental Section:

Chemicals: cesium carbonate (Cs₂CO₃), lead chloride (PbCl₂), manganese chloride (MnCl₂*4H₂O), octylammonium bromide (Oct-Br), octadecene (ODE), oleic acid (OA), oleylamine (OM), toluene (anhydrous)

Preparation of the Cesium Precursor: 0.4 g Cs₂CO₃ was mixed with 8 ml OA and loaded into a 50 ml flask, degassed and dried under 120 °C for 30 min under vacuum, and then heated at 150 °C under N₂ atmosphere for an additional 30 min to complete the reaction between Cs₂CO₃ and OA. The resulting solution was kept at 150 °C for further use.

Preparation of Pure CsPbCl₃ NCs and Mn²⁺ doped CsPbCl₃ NCs: pure CsPbCl₃ NCs and Mn²⁺ doped CsPbCl₃ NCs with 40 at% nominal Mn-doping concentrations (added mole fraction relative to Pb²⁺) were synthesized at a temperature of 190 °C. For a typical synthesis, 0.222 g (0.8 mmol) PbCl₂ and 0.064 g (0.32 mmol) MnCl₂*4H₂O were loaded into a 50 ml three neck flask with 20 ml ODE, 2 ml OA and 2 ml OM in a N₂ gas filled glovebox. The flask was then transferred to a Schlenk line, dried under vacuum at 120 °C and then heated to 190 °C under N₂ atmosphere. 10 min after reaching the 190 °C, 1.8 ml of the hot Cs precursor was injected swiftly. The reaction was quenched 30s later by immersion of the reaction container in an ice-water bath. The product was separated by centrifuging washed once with acetone/hexane and finally dissolved in 5 ml toluene.

Preparation of Br-anion Precursor: 0.042 g (0.2 mmol) of Oct-Br was dissolved in the 10 ml toluene and heated to 60 °C for 30 min. The resulting clear and colorless solution was kept at 60 °C for further use.

Preparation of Mixed-anion NCs by Post-synthesis Anion Exchange: To compare NC concentrations, it is assumed that the molar extinction coefficient of pure CsPbCl₃ NCs and Mn²⁺ doped CsPbCl₃ NCs are the same around 355 nm. The products are diluted with a designated amount of toluene and the concentration of both pure CsPbCl₃ NCs and Mn²⁺-doped CsPbCl₃ NCs were calibrated by the absorption strengths at 355 nm. The resulting solutions were mildly heated to 40 °C and a varying amount of Br precursor (oct-Br) was subsequently added (From 10 μL to 100 μL with a step of 10 μL). The obtained samples were allowed to settle for 2h to precipitate extra anion precursors (limited solubility of oct-Br in toluene at room temperature). Then only the supernatant of each sample was collected and used for the measurements. The exciton emission wavelength of the samples after anion exchange showed no temporal evolution during the time of measurement indicating that the composition (Cl/Br ratio) was stable after anion exchange and removal of excess Br⁻ precursor. The exciton emission wavelength was measured for each sample and was observed to continuously shift, from 400 nm to 442 nm, upon exchange of Cl⁻ by Br⁻.

Characterization Method

Transmission electron microscopy (TEM) images were made with a FEI TECNAI T12 and FEI TECNAI T20, operating at 120 kV and 200 kV respectively. The samples for TEM imaging were prepared by dipping a carbon-coated copper mesh TEM grid into a hexane solution of NCs. The excess liquid was evaporated under vacuum.

Absorption spectra were obtained with a double beam Perkin-Elmer Lambda 950 UV/VIS/IR spectrophotometer. Luminescence (emission and excitation) spectra and photoluminescence (PL) decay curves were measured using an Edinburgh Instruments FLS920 spectrofluorometer equipped with a 450 W Xenon lamp as excitation source and a 0.22 m double grating monochromator for excitation (Bentham DTMS300, 1200 lines/mm grating, blazed at 300 nm for excitation). Emission spectra (380-700 nm) were recorded with a single 0.22 m monochromator (500 nm blazed grating) and the emitted light was detected by a Hamamatsu R928 photomultiplier tube (PMT). The PL QYs of undoped samples were determined using this spectrometer equipped with a calibrated integrating sphere. Decay curves of the Mn²⁺ emission were recorded in the same set-up using the 3rd harmonic of a 10 Hz pulsed Nd:YAG laser as the excitation source (pulse width: 10 ns,

$\lambda_{\text{ex}}=355$ nm) and a Hamamatsu R928 photomultiplier tube (PMT) for light detection. The fast decay profiles of the exciton emission were recorded by using an Edinburgh EPL375 pulsed diode laser ($\lambda_{\text{ex}}=376.8$ nm, pulse width: 65 ps) with a fast Hamamatsu H74422–40 PMT. An Oxford Instruments liquid helium flow cryostat was used to measure the PL properties at low temperatures (down to 4.2 K). The samples for room temperature optical analysis were prepared by dissolving the crude NCs mixture in hexane and transferring the solution to the quartz cuvette. For low temperature measurement, the dried samples were sandwiched between two quartz plates.

4.3 Results and Discussion

Fast anion-exchange is one of the unique properties of lead halide perovskite nanocrystals (NCs).^{20, 21} The rapid exchange allows a facile post-synthetic treatment to continuously vary the composition and properties of these materials. Replacement of lighter halides (Cl⁻) by heavier halide ions (Br⁻ or I⁻) decreases the bandgap, or vice versa. Notably, during such rapid anion-exchange the cationic sub-lattice of NCs is largely unaffected because of the lower mobility of the cations. As a result, the parent NCs' morphological features and size-dispersity are maintained during the anion-exchange process.

Anion exchange can be achieved by addition of a halide precursor. As a control experiment, the influence of Cl⁻↔Br⁻ anion exchange was first investigated for undoped CsPbCl₃ NCs.

CsPbCl₃ NCs of ~12 nm were used as parent NCs. Addition of bromide precursors into the colloidal solution of CsPbCl₃ NCs initiates the Cl⁻ to Br⁻ ion exchange. The halide exchange induces a red shift of both the absorption onset and exciton emission peak, indicating the narrowing the band gap as the result of gradual substitution of Cl⁻ by Br⁻. In Figure 4.1a the absorption and emission spectra are shown upon raising the Br⁻ content in CsPbCl_{3-x}Br_x from x=0 (black spectrum, bottom) to x=1.18 (blue spectrum, top). Fine-tuning of the Br⁻ content results in shift of the absorption onset and emission in the range of 400 nm to 442 nm. The Br⁻ content x can be estimated based on the position of the exciton emission peak. A continuous shift to longer wavelengths from 404 nm (x=0) to 420 nm (x=0.6) to 437 nm (x=1.1) to 487 nm (x=2.4).⁷ Similar shifts are reported in Refs. 22. Based on the known relation between the exciton peak position and Br⁻ content we determined the Br⁻ content in our samples from the position of the exciton emission peak.

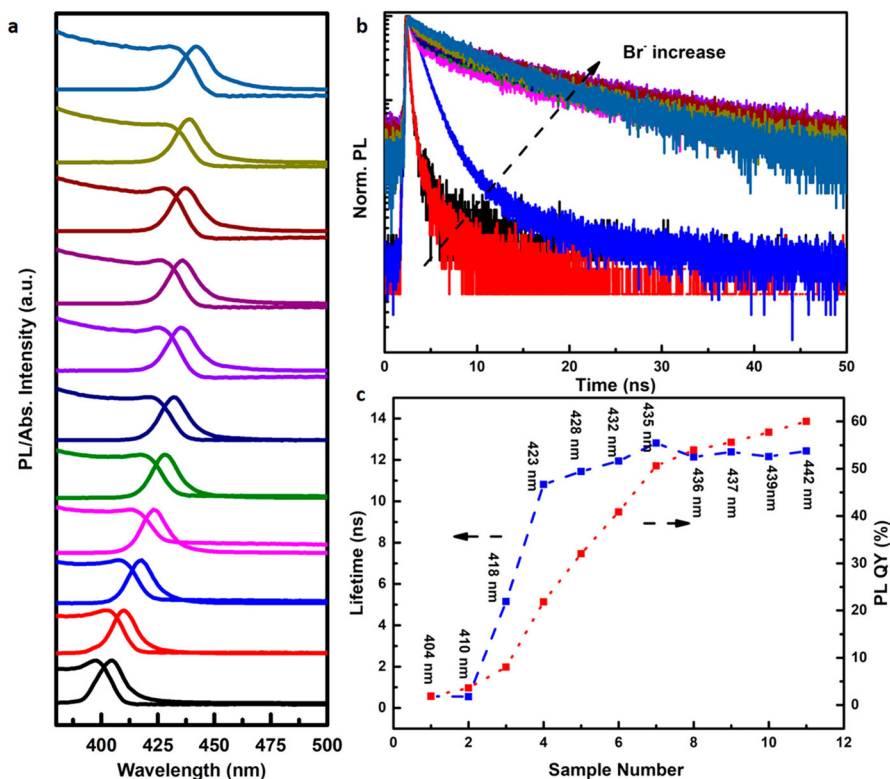


Figure 4.1. Evolution of photoluminescence properties of CsPbCl_{3-x}Br_x NCs at 300 K as function of x (x is varied from 0 to 1.18 estimated from the position of the exciton peak). (a) Absorption and emission spectra of CsPbCl_{3-x}Br_x NCs with different x ($\lambda_{\text{ex}}=355$ nm). (b) Luminescence decay curves of the exciton emission for CsPbCl_{3-x}Br_x NCs plotted on semi-logarithmic scale ($\lambda_{\text{ex}}=376$ nm, pulse width= 65 ps) (3) PL QY and exciton emission lifetime of CsPbCl_{3-x}Br_x NCs upon increasing x . The Br⁻ content can be determined from the position of the exciton emission peak (see Ref. 7, 22) and increases from $x=0$ for Sample 1 to $x=0.55$ for Sample 3, $x=0.84$ for Sample 5, $x=1.07$ for sample 8 and $x=1.18$ for sample 11.

The Br⁻ content increases from $x=0$ for Sample 1 to $x=0.55$ for Sample 3, $x=0.84$ for Sample 5, $x=1.07$ for sample 8 and $x=1.18$ for sample 11. Besides the red shift of the

Chapter 4

photoluminescence, with the replacement of Cl^- by Br^- the PL QY increases and the exciton life time is lengthened, as illustrated in Figures 4.1b and c. The origin of the substantial enhancement of PL QY is twofold. First, the addition of a halide source efficiently passivates the surface halide vacancies. Surface halide vacancies provide non-radiative recombination sites (sub-band trap state) which reduce the PL QY of exciton emission.^{23,24} The origin of halide vacancies is a halide deficiency resulting from the synthesis strategy. In a typical synthesis, PbX_2 is used as the halide source and subsequent addition of Cs-oleate triggers the crystallization of CsPbX_3 with a metal to halide ratio=1:1:3 (Cs:Pb:X). Consequently, the Pb^{2+} ions are in excess and thus contribute to the creation of halide vacancy trap states.²⁵ In addition, the post-synthetic purification contributes to the loss of surface halide ions. Filling of halide vacancies in a halide rich reaction medium has been shown to enhance the PL QY.^{26,27} Also for Mn^{2+} -doped CsPbCl_3 NCs, the PL QY of the exciton emission increases compared to undoped CsPbCl_3 NCs synthesized under similar conditions.⁸ The halide ions introduced by the added MnCl_2 contribute to the enhancement of the exciton emission. Furthermore, the position of trap states relative to the bottom of conduction band varies with the halide composition. With the narrowing the band gap, the density of trap states within the band gap can decrease substantially, which render NCs with a smaller band gap more efficient as demonstrated by Kovalenko et al²⁸ and Yamauchi et al²⁹. With increasing PL QY the exciton emission lifetime lengthens (Figure 4.1b), consistent with a reduction in the non-radiative decay rate.

In the subsequent section, we focus on the influence of anion composition on the exciton-to- Mn^{2+} ET efficiency. The starting Mn^{2+} -doped CsPbCl_3 NCs were synthesized with a hot-injection method and a 2.8 at% concentration of Mn^{2+} which is an optimum concentration to realize high Mn^{2+} luminescence efficiencies. Exciton-to- Mn^{2+} ET becomes less efficient for lower doping concentrations while for higher concentrations, concentration quenching occurs.¹⁶ Representative TEM images and photographs of both doped and undoped CsPbCl_3 NCs and EDX spectrum of doped CsPbCl_3 NCs are shown in the supporting information (Supporting Information Figure S4.1). Similar morphology and size distribution are observed for the Mn^{2+} -doped and undoped CsPbCl_3 NCs (cubic, with edge length of ~12 nm). PL properties of Mn^{2+} -doped CsPbCl_3 NCs resemble their undoped counterpart with a few noteworthy differences. For Mn^{2+} -doped CsPbCl_3 NCs, a slight blue-shift of the absorption spectrum is noticed and ascribed to an alloying effect.

Chapter 4

Replacement of Pb^{2+} by the smaller and more ionic Mn^{2+} ion results in a widening of the bandgap with increasing Mn^{2+} content⁷ similar to the widening of the bandgap observed for Mn-doped CdSe QDs³⁰. The loss of sharpness of the absorption spectrum at the onset reflects the statistical nature of dopant inclusion within the ensemble of NCs. To explore the influence of replacement of Cl^- by Br^- a series of samples with various Br/Cl ratios was synthesized by a facile post-synthetic anion exchange using octylammonium bromide (oct-bromide) as bromide precursor. Oct-bromide is a Pb-free Br-precursor and its use allows for anion exchange without loss of Mn^{2+} from the NCs during the exchange reaction.⁷ On the contrary, using PbBr_2 as a Br^- source has been shown to result in Mn^{2+} loss.⁷ Samples with various Br/Cl ratios have nearly identical morphology and size-dispersity. No broadening of the exciton emission peak is observed which serves as evidence for the formation of homogeneous final products. The use of a halide-ammonium precursor (unlike PbX_2 , $\text{X}=\text{Cl}, \text{Br}, \text{I}$) avoids a role of cation exchange accompanying anion exchange and allows for a meaningful comparison between different samples. To carefully probe the role of the Br/Cl ratio, eleven samples were studied for $x=0$ (no Br^-) to $x=1.18$. The exact Br^- content was not determined as it is difficult to completely wash away all precursor materials. The continuous shift of the exciton emission line from 404 nm to 442 nm shows a continuously increasing Br^- content in the series of samples. The Br^- content x was estimated based on the position of the exciton emission peak just as for the undoped $\text{CsPbCl}_{3-x}\text{Br}_x$ NCs and increases from $x=0$ for Sample 1 to $x=0.42$ for Sample 3, $x=0.79$ for Sample 5, $x=1.04$ for sample 8 and $x=1.18$ for sample 11. The normalized emission spectra of the $\text{CsPbCl}_{3-x}\text{Br}_x:\text{Mn}^{2+}$ samples at 300 K and 4.2 K are shown in Figures 4.2a and b (for absorption spectrum and calibrated emission spectra at 300 K, see Supporting Information, Figure S4.2a). While the exciton emission redshifts to longer wavelengths upon increasing the Br^- content, a small but consistent blue shift of Mn^{2+} emission (from 601 nm to 593 as x is increased from 0 to 1.18) is clearly observed with increasing Br^- fraction. A similar blue shift of the Mn^{2+} emission upon increasing the Br^- content was recently reported in Ref. 19. The blue shift is attributed to lattice expansion due to exchange of the smaller Cl^- by larger Br^- anions which results in a weaker of the crystal field. In the Tanabe-Sugano ($3d^5$) diagram of Mn^{2+} it is evident that the ${}^4\text{T}_1$ excited state shifts to higher energies for a weaker crystal field which explains the observed blue shift. To investigate the influence of the Br/Cl ratio on the exciton-to- Mn^{2+} ET efficiency, the ratio of the Mn^{2+} to exciton emission intensities ($I_{\text{Mn}}/I_{\text{Exc}}$) was determined from the spectra in Figure 4.2a and

4.2b. In Figure 4.2c the ratio is plotted for the series of samples both at 300 K and 4.2 K. I_{Mn}/I_{Exc} initially increases with Br^- content. At 300 K a significant three-fold increase is observed upon substitution of Cl^- by Br^- reaching a maximum ratio of 26 for the sample showing exciton emission at 420 nm. The subsequent decrease upon further Cl^- to Br^- substitution results in a ratio of ~ 8 for $x=1.18$ (Sample 11), similar to ratio observed in the $CsPbCl_3:Mn^{2+}$ sample ($x=0$).

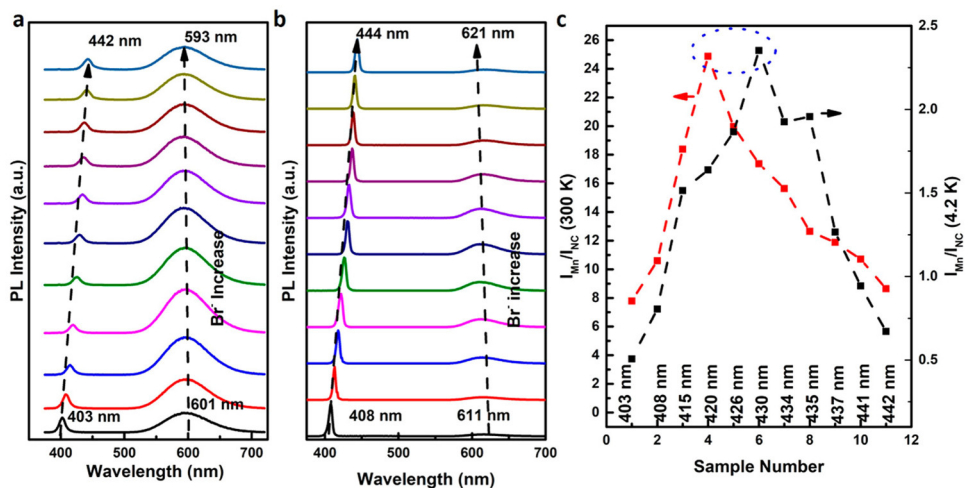


Figure 4.2. Evolution of emission spectra as the function of Br^- content in 2.8% Mn^{2+} -doped $CsPbCl_{3-x}Br_x$ NCs ($\lambda_{exc}=355$ nm) at (a) 295 K and (b) 4.2 K. (c) Evolution of the Mn^{2+} -to-exciton integrated emission intensity ratio with x at 300 K (red curve) and 4.2 K (black curve) as determined from the spectra in Figures a and b. The Br^- content can be determined from the position of the exciton emission peak (see Refs. 7, 22) and increases from $x=0$ for Sample 1 to $x=0.42$ for Sample 3, $x=0.79$ for Sample 5, $x=1.04$ for sample 8 and $x=1.18$ for sample 11.

In analogy with previous work on dual emission in $Zn_{1-x}Mn_xSe/ZnCdSe$ QDs, the PL intensity of exciton (I_{Exc}) and Mn^{2+} (I_{Mn}) are described using equations (4.1) and (4.2).³¹ The emission intensities are determined by the total generation rate (G), non-radiative and radiative decay rate for the emitting excitonic states in the NCs (k_{nr}^{Exc} , k_r^{Exc}) and Mn^{2+} (k_{nr}^{Mn} ,

Chapter 4

k_r^{Mn}), forward and back energy transfer rates (k_{ET} , k_{BET}) and the population of ground state (N_{gs}), excited state of Mn^{2+} (N_{Mn}) and nanocrystal (N_{NC})

$$I_{Exc} = K_r^{Exc} N_{NC} = GN_{gs} + k_{BET} N_{Mn} - (k_{nr}^{Exc} + k_{ET}) N_{NC} \quad (4.1)$$

$$I_{Mn} = K_r^{Mn} N_{Mn} = k_{ET} N_{NC} - (k_{nr}^{Mn} + k_{BET}) N_{Mn} \quad (4.2)$$

Upon creation of an exciton in Mn^{2+} doped $CsPbCl_{3-x}Br_x$ NCs, several relaxation mechanisms are active. Charge carrier trapping at surface-related trap states accounts for the decreased PL QY and shortening of exciton lifetime and contributes to k_{nr}^{Exc} . For Mn^{2+} -doped NCs a competing de-excitation pathway is exciton-to- Mn^{2+} energy transfer. Compared to II-VI Mn^{2+} -doped NCs, ET to Mn^{2+} in Mn^{2+} -doped $CsPbCl_3$ NCs is slow which is attributed to the highly ionic nature of the NCs. Typical exciton to Mn^{2+} energy transfer rates k_{ET} in $CsPbCl_3$ NCs are in the 0.3 to 3 ns⁻¹ range^{8, 15}, more than an order of magnitude slower than in $Zn_{1-x}Mn_xSe/ZnCdSe$ ^{32, 33}. This slow ET explains the co-existence of exciton and Mn^{2+} emission even in heavily Mn^{2+} -doped $CsPbCl_3$ NCs. The non-radiative decay rate of excited Mn^{2+} (k_{nr}^{Mn}) is usually neglected as Mn^{2+} luminescence quenching is limited as evidenced by a single exponential decay with a ms decay time, typical of the radiative life time for Mn^{2+} emission (supporting information, Figure S4.3).

To understand the variation of the Mn^{2+} to exciton emission intensity ratios, competition between all possible decay processes needs to be considered, i.e. radiative and non-radiative decay of the of the exciton as well as forward and back energy transfer between exciton and Mn^{2+} . As discussed above, for undoped $CsPbCl_3$ a substantial increase in the PL QY is observed for the exciton emission during the Cl^- to Br^- anion exchange process by elimination of surface trap states which reduces non-radiative exciton decay and turns on dark NCs. The fast non-radiative decay will compete with both exciton emission and energy transfer to Mn^{2+} in Mn^{2+} -doped NCs. Upon anion exchange the addition of Br^- anions leads to passivation of surface states and causes a decrease in the direct non-radiative decay channel. The decrease in the non-radiative decay rate for the exciton emission that accompanies the anion exchange process cannot explain the increase in the relative intensity of the Mn^{2+} emission as it would mostly enhance the exciton emission intensity. Non-radiative ET to surface trap states is fast and is expected to dominate in NCs

Chapter 4

with surface trap states. It is responsible for a decrease in the overall emission intensity. The relative intensities of exciton and Mn^{2+} emission are determined by competition between the radiative decay rate of the exciton emission and the ET rate to Mn^{2+} . The increase in ratio of the Mn^{2+} -to-exciton emission intensity ratio upon substitution of Cl by Br⁻ therefore reflects the change in ratio between the radiative exciton decay rate (k_r^{Exc}) and the energy transfer rate to Mn^{2+} (k_{ET}). The observed increase in the relative intensity of the Mn^{2+} emission can be explained by two effects: (1) The radiative exciton decay rate decreases with increasing Br⁻ content and (2) the exciton-to- Mn^{2+} ET rate increases. A decrease of the radiative decay rate of exciton emission both at room temperature and at cryogenic temperatures has been reported from CsPbCl_3 to CsPbBr_3 to CsPbI_3 .^{4, 34} The influence of chemical composition on the exciton-to- Mn^{2+} transfer rate is not well established. It is clear that the ET efficiency is low in comparison to the II-VI semiconductor QDs where ~20 ps transfer times have been observed.³² The slow ns ET in CsPbCl_3 has been attributed to the ionic character of the perovskite NCs. In addition, the larger size of the perovskite NCs (typically ~10 nm) in comparison with the II-VI QDs (3-6 nm) will reduce wavefunction overlap and thus reduce the ET rate. Substitution of Cl with Br⁻ will increase the host covalency and can qualitatively explain the observed increase in ET rate.

Following the initial strong increase of $I_{\text{Mn}}/I_{\text{Exc}}$ with the fraction of Br⁻ ions, a sharp decrease of the relative Mn^{2+} emission intensity is observed upon further raising the Br⁻ content, in the regime where the exciton emission shifts from 420 to 442 nm. This cannot be explained by a change in k_r^{Exc} (which expected to continue to decrease with Br⁻ content) or k_{ET} (which will continue to increase with Br⁻ content). However, as the bandgap narrows with increasing Br⁻ content, back transfer from Mn^{2+} to the exciton can occur. As the radiative decay rate of the exciton emission is about 10^6 times higher than the slow (ms, spin- and parity-forbidden) Mn^{2+} emission, already for small thermal population levels back transfer will result in dominant exciton emission. The situation is analogous to that for $\text{CdSe}:\text{Mn}^{2+}$. In small CdSe QDs (large bandgap) fast trapping of the exciton results in dominant Mn^{2+} emission. In larger QDs with a narrower bandgap, the proximity of the Mn^{2+} excited states and the band edge of the CdSe QDs results in efficient back transfer from Mn^{2+} to the exciton, giving strongly temperature dependent Mn^{2+} and exciton emission intensities.³³ The back energy transfer is a thermally activated processes with a

Chapter 4

rate proportional to the $\exp(-E_a/k_B T)$ in which the activation energy E_a is the energy separation between the band edge and the emitting state of Mn^{2+} . The activation barrier E_a is reduced with the progressive exchange of Cl^- by Br^- , and hence the thermally activated back energy transfer becomes more pronounced and causes a reduction in the $I_{\text{Mn}}/I_{\text{Exc}}$ emission intensity ratio. The back energy transfer is also collaborated by the time resolved PL measurement of Mn^{2+} . The shortening of excited lifetime of Mn^{2+} with increasing of bromide fraction (decreasing of E_a) provides additional experimental evidence of back energy transfer (for decay curves, see Supporting Information S4.3). Note that also enhanced spin-orbit interaction through the replacement of chlorine by heavier bromide contributes to faster decay of Mn^{2+} emission (heavy atom effect, coordination with heavy ligands enhances spin-orbit coupling to relax the spin-selection rule for spin-forbidden transitions).

To obtain further information on the competition between exciton emission and exciton-to- Mn^{2+} ET as a function of host composition in $\text{CsPbCl}_{3-x}\text{Br}_x$, photoluminescence measurements were conducted in liquid helium (4.2 K, Figure 4.2b). At cryogenic temperatures thermally activated quenching by trap (surface) states is reduced and the relative intensities of the Mn^{2+} and exciton emission ($I_{\text{Mn}}/I_{\text{Exc}}$) more closely reflect the composition dependence of $k_{\text{ET}}/k_{\text{r}}^{\text{Exc}}$. The evolution of intensity ratio of various samples at 4.2 K is depicted in the Figure 4.2c. A similar trend is found as for the measurements at 295 K. An initial increase of the intensity ratio is followed by a decrease, now starting at a sample with a higher Br^- content (exciton emission at 430 nm). The absolute values of the intensity ratios $I_{\text{Mn}}/I_{\text{Exc}}$ are about 10 times smaller at 4.2 K. The higher relative intensity of the exciton emission and can be understood from the much faster radiative decay rate $k_{\text{r}}^{\text{Exc}}$ of the exciton emission at 4.2 K.³⁴ Contrary to other QDs (e.g. II-VI and IV-VI), the lowest exciton state is a bright state for CsPbX_3 perovskite nanocrystals with an order of magnitude faster decay rate than higher energy exciton states which are thermally populated at room temperature.³⁴ The higher value for $k_{\text{r}}^{\text{Exc}}$ at 4.2 K and a similar value for k_{ET} explains the large difference in $I_{\text{Mn}}/I_{\text{Exc}}$ between 4.2 K and 300 K.

The composition dependence shows that upon raising the Br^- content in the $\text{CsPbCl}_{3-x}\text{Br}_x:\text{Mn}^{2+}$ NCs again an initial increase in $I_{\text{Mn}}/I_{\text{Exc}}$ is followed by a sharp decrease. The transition point has shifted to a higher Br^- content (i.e. smaller bandgap). This is consistent with back transfer as the mechanism responsible for the decrease in I_{Mn} . At RT

Chapter 4

thermally activated back transfer occurs when the Mn^{2+} excited state is close to the NC edge state. The energy difference between the transition points at 4.2 K and 300 K (430 nm vs. 420 nm) correspond to a difference in host bandgap of $\sim 550 \text{ cm}^{-1}$, close to $\sim 3 \text{ kT}$ at 300 K. The 4.2 K measurements pinpoint the composition where the Mn^{2+} excited state is resonant with band states of the $\text{CsPbCl}_{3-x}\text{Br}_x$ NCs which emit at 430 nm since at 4 K thermally activated back transfer can be neglected and the Mn^{2+} excited state can only transfer to states at the same or lower energies.

Back transfer from excited d-states to the conduction band becomes possible when the d-states overlap in energy with the continuum of band states of the valence or conduction band.³⁵⁻³⁷ The position of the ground state relative to the band edges is crucial. If the ground state is resonant with the valence band edge, the exciton emission and dopant emission need to be close in energy. However, if the ground state is situated above the valence band edge, back transfer from excited d-states to conduction band states can occur when the dopant emission is lower in energy than the exciton emission. With an electronic origin of the Mn^{2+} d-d emission band around 550 nm and substantial quenching of the Mn^{2+} emission for NCs with exciton emission around 440 nm, the energy mismatch of $\sim 0.5 \text{ eV}$ corresponds to the energy difference between the Mn^{2+} ground state and the top of the valence band.

It is also insightful to investigate the temperature dependence of the luminescence properties. In Figure 4.3 the temperature dependent emission, luminescence decay curves and absolute Mn^{2+} emission intensities are shown for the mixed $\text{CsPbCl}_{3-x}\text{Br}_x:\text{Mn}^{2+}$ sample with the highest relative Mn^{2+} emission intensity at 4.2 K (430 nm exciton emission). The exciton emission shows a small but consistent shift to longer wavelengths (red shift) from 430 nm at 300 K to 435 nm at 4.2 K. For most semiconductors a blue shift is observed upon cooling and is described by the empirical Varshni equation.³⁸ Just as for CsPbX_3 NCs, also for PbX ($X=\text{S}, \text{Se}, \text{Te}$) QDs an anomalous redshift has been reported upon cooling and has been explained by competing influences on the bandgap energy, related to lattice contraction and freezing out of lattice vibrations upon lowering of T .³⁹ It will be interesting to conduct further research to elucidate the mechanism behind the anti-Varshni behavior in Pb-containing semiconductors NCs. The Mn^{2+} emission also shows a marked redshift from 588 nm at 300 K to 615 nm at 4.2 K. This redshift is explained by lattice contraction.

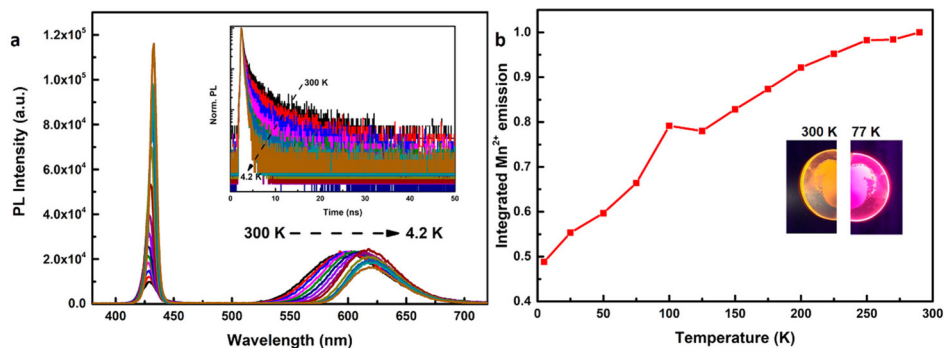


Figure 4.3. Temperature dependent luminescence of $\text{CsPbCl}_{3-x}\text{Br}_x\text{:Mn}^{2+}$ 2.8% for sample of exciton emission wavelength 430 nm ($x=0.90$). (a) Emission spectra at different temperature ($\lambda_{\text{ex}}=355$ nm). Inset: luminescence decay curves of the exciton emission ($\lambda_{\text{ex}}=376$ nm, pulse width: 65 ps). (b) The evolution of integrated Mn^{2+} emission with temperature. The inset shows a photograph of the sample at 300 K and at 77 K under illumination with a handheld UV-lamp emitting 365 nm UV radiation. The color shift reflects the much higher relative intensity of the exciton emission at 77 K compared to 300 K.

The position of emission peak of Mn^{2+} is largely determined by the crystal field splitting (Dq) which increases as the distance between Mn^{2+} and coordinating ligands (here Cl^- and Br^- anions) decreases. Lowering the temperature gives lattice contraction and enhances the crystal field splitting. In the Tanabe-Sugano diagram for the $3d^5$ configuration it is clear that the 4T_1 excited state of Mn^{2+} from which the orange emission originates is lowered in energy for a higher crystal field and this explains a red shifted Mn^{2+} emission upon lattice contraction.

The temperature dependent decay kinetics of the exciton emission (inset Figure 4.3a) show the increasingly fast decay upon lowering the temperature. The average decay time decreases from 1.7 ns at 300 K to 0.7 ns at 4.2 K. The faster decay can be explained by the higher radiative decay rate from the lowest (bright) exciton state. The low temperature decay times observed are limited by the time resolution of the experimental set-up (~ 0.5 ns). The absolute intensity of the Mn^{2+} emission (Figure 4.3b) shows a continuous

reduction upon cooling and decreases by a factor of 2 between 300 K and 4.2 K. For Mn^{2+} -doped CsPbCl_3 NCs (the parent NCs), the integrated PL intensity of Mn^{2+} at 4.2 K decreased more strongly, by a factor of ~ 3 compared to 300 K. An even more substantial decrease was reported by Gamelin et al.¹⁶ who observed a fivefold decrease of the Mn^{2+} intensity upon cooling to 80 K. The origin of these differences is in the larger k_{ET}/k_r ratio for the bromine rich samples which enhances the Mn^{2+} emission and gives rise to brighter Mn^{2+} emission at 4.2 K. The variations between samples reflect differences in non-radiative decay rate (surface defects) which affect the absolute emission intensities, especially at 300 K and thus contribute to how absolute emission intensities vary. The situation in the perovskite nanocrystals is vastly different from that in II-VI QDs where a strong increase in Mn^{2+} emission is observed upon cooling. The highly efficient trapping of excitons by the Mn^{2+} dopants give rise to dominant Mn^{2+} emission. Both non-radiative decay rates and back transfer rates from Mn^{2+} to the exciton are reduced at low temperature in Mn^{2+} -doped II-VI QDs and give rise to strongly enhanced Mn^{2+} emission at cryogenic temperatures.

A more quantitative analysis of the exciton emission decay curves shows that the average decay rates of undoped (emission wavelength: 432 nm) and doped samples (emission wavelength: 430 nm) are 1.1 ns^{-1} (k_r^{Exc}) and 3.7 ns^{-1} ($k_r^{\text{Exc}} + k_{\text{ET}}$), respectively, at 4.2 K. This enables us to calculate k_{ET} to be approximately 2.6 ns^{-1} and hence the $k_{\text{ET}}/k_r^{\text{Exc}}$ is 2.5 which is in good agreement with the branching ratio from steady state luminescence measurement of 2.4. Even though good agreement is obtained, it is important to realize that the calculated energy transfer rate is a rough estimate as the time scale of 0.7 ns is approaching the time response of the system ($\sim 0.5 \text{ ns}$).

5.3 Conclusions

In summary, the composition and temperature dependence of Mn^{2+} to exciton emission intensity ratios have been investigated for mixed halide $\text{CsPbCl}_{3-x}\text{Br}_x$ perovskite NCs ($x = 0$ to ~ 1.18). Slow ($\sim \text{ns}$) exciton-to- Mn^{2+} transfer times are observed, consistent with earlier reports. The transfer efficiency can be controlled by the Br/Cl ratio. Initial substitution of Cl by Br⁻ enhances the efficiency through a combined effect of slower exciton decay and faster energy transfer. As the bandgap narrows upon further substitution of Br⁻, back energy transfer from Mn^{2+} to host band states sets in and results in a strong reduction of the relative Mn^{2+} emission intensity. At cryogenic temperatures the energy transfer efficiency is

Chapter 4

reduced which is explained by the faster radiative exciton decay from the lowest energy bright exciton state. Again, faster energy transfer is observed upon substituting Cl⁻ by Br⁻ reaching a maximum efficiency for compositions with an exciton emission at 430 nm. The new insights in the exciton-to-Mn²⁺ energy transfer pinpoint the position of the Mn²⁺ excited state relative to the CsPbCl_{3-x}Br_x band states and predict the temperature and composition dependent optical properties of Mn²⁺-doped halide perovskite NCs.

References

1. Rosales, B. A.; Hanrahan, M. P.; Boote, B. W.; Rossini, A. J.; Smith, E. A.; Vela, J. Lead Halide Perovskites: Challenges and Opportunities in Advanced Synthesis and Spectroscopy. *ACS Energy Lett.*, 2017, 2, 906-914
2. Yuan, M.; Quan, L. N.; Comin, R.; Walters, G.; Sabatini, R.; Voznyy, O.; Hoogland, S.; Zhao, Y.; Beauregard, E. M.; Kanjanaboos, P.; Lu, Z.; Kim, D. H.; Sargent, E. H. Perovskite Energy Funnels for Efficient Light-Emitting Diodes. *Nat. Nanotech.*, 2016, 11, 872-877
3. Sutton, R. J.; Eperon, G. E.; Miranda, L.; Parrott, E. S.; Kamino, B. A.; Patel, J. B.; Hörantner, M. T.; Johnston, M. B.; Haghighirad, A. A.; Moore, D. T.; Snaith, H. J. Tunable Cesium Lead Halide Perovskites with High Thermal Stability for Efficient Solar Cells. *Adv. Energy Mater.*, 2016, 6, 1502458-1502463.
4. Protesescu, L.; Yakunin, S.; Bodnarchuk, M. I.; Krieg, F.; Caputo, R.; Hendon, C. H.; Yang, R.; Walsh, A.; Kovalenko, M. V. Nanocrystals of Cesium Lead Halide Perovskites (CsPbX_3 , X = Cl, Br, and I): Novel Optoelectronic Materials Showing Bright Emission with Wide Color Gamut. *Nano Lett.*, 2015, 15, 3692-3696
5. Song, J.; Li, J.; Li, X.; Xu, L.; Dong, Y.; Zeng, H. Quantum Dot Light-emitting Diodes Based on Inorganic Perovskite Cesium Lead Halides (CsPbX_3). *Adv. Mater.*, 2015, 27, 7162-7167.
6. Li, X.; Wu, Y.; Zhang, S.; Cai, B.; Gu, Y.; Song, J.; Zeng, H. CsPbX_3 Quantum Dots for Lighting and Displays: Room Temperature Synthesis, Photoluminescence Superiorities, Underlying Origins and White Light-emitting Diodes. *Adv. Funct. Mater.*, 2016, 26, 2435-2446.
7. Liu, W.; Lin, Q.; Li, H.; Wu, K.; Robel, I.; Pietryga, J. M.; Klimov, V. I., Mn^{2+} -doped Lead Halide Perovskite Nanocrystals with Dual-color Emission Controlled by Halide Content. *J. Am. Chem. Soc.*, 2016, 138, 14954-14961.
8. Parobek, D.; Roman, B. J.; Dong, Y.; Jin, H.; Lee, E.; Sheldon, M.; Son, D., Exciton-to-dopant Energy Transfer in Mn-doped Cesium Lead Halide Perovskite Nanocrystals. *Nano Lett.*, 2016, 16, 7376-7380.
9. Liu, H.; Wu, Z.; Shao, J.; Yao, D.; Gao, H.; Liu, Y.; Yu, W.; Zhang, H.; Yang, B., $\text{CsPb}_x\text{Mn}_{1-x}\text{Cl}_3$ Perovskite Quantum Dots with High Mn Substitution Ratio. *ACS Nano.*, 2017, 11, 2239-2247.

Chapter 4

10. Xu, K.; Lin, C.; Xie, X.; Meijerink, A., Efficient and Stable Luminescence from Mn^{2+} in Core and Core-isocrystalline Shell CsPbCl_3 Perovskite Nanocrystals. *Chem Mater.*, 2017, 29, 4265-4272.
11. Zhou, D.; Liu, D.; Pan, G.; Chen, X.; Li, D.; Xu, W.; Bai, X.; Song, H. Cerium and Ytterbium Codoped Halide Perovskite Quantum Dots: A Novel and Efficient Downconverter for Improving the Performance of Silicon Solar Cells. *Adv. Mater.*, 2017, 29, 1704149-1704154.
12. Pan, G.; Bai, X.; Yang, D.; Chen, X.; Jing, P.; Qu, S.; Zhang, L.; Zhou, D.; Zhu, J.; Xu, W.; Dong, B.; Song, H. Doping Lanthanide into Perovskite Nanocrystals: Highly Improved and Expanded Optical Properties. *Nano Lett.*, 2017, 17, 8005-8011.
13. Wang, Q.; Zhang, X.; Jin, Z.; Zhang, J.; Gao, Z.; Li, Y.; Liu, S., Energy-down-shift CsPbCl_3 :Mn Quantum dots for Boosting the Efficiency and Stability of Perovskite Solar Cells. *ACS Energy Lett.*, 2017, 2, 1479-1486.
14. Meinardi, F.; Akkerman, Q. A.; Bruni, F.; Park, S.; Mauri, M.; Dang, Z.; Manna, L.; Brovelli, S., Doped Halide Perovskite Nanocrystals for Reabsorption-Free Luminescent Solar Concentrators. *ACS Energy Lett.*, 2017, 2, 2368-2377.
15. Rossi, D.; Parobek, D.; Dong, Y.; Son, D. H., Dynamics of Exciton-to-Mn Energy Transfer in Mn doped CsPbCl_3 Perovskite Nanocrystals. *J. Phys. Chem. C*, 2017, 121, 17143-17149.
16. Yuan, X.; Ji, S.; De Siena, M. C.; Fei, L.; Zhao, Z.; Wang, Y.; Li, H.; Zhao, J.; Gamelin, D. R., Photoluminescence Temperature Dependence, Dynamics, and Quantum Efficiencies in Mn^{2+} -Doped CsPbCl_3 Perovskite Nanocrystals with Varied Dopant Concentration. *Chem. Mater.*, 2017, 29, 8003-8011.
17. Chen, D.; Fang, G.; Chen, X., Silica-Coated Mn-Doped $\text{CsPb}(\text{Cl}/\text{Br})_3$ Inorganic Perovskite Quantum Dots: Exciton-to-Mn Energy Transfer and Blue-Excitable Solid-State Lighting. *ACS Appl. Mater. Interfaces*, 2017, 9, 40477-40487.
18. Chen, H. Y.; Maiti, S.; Son, D. H. Doping Location-Dependent Energy Transfer Dynamics in Mn-doped CdS/ZnS Nanocrystals. *ACS Nano*, 2012, 6, 583-591.
19. Li, F.; Xia, Z. G.; Pan, C. F.; Gong, Y.; Gu, L.; Liu, Q. L.; Zhang, J. Z. High Br-Content $\text{CsPb}(\text{Cl}_y\text{Br}_{1-y})_3$ Perovskite Nanocrystals with Strong Mn^{2+} Emission through Diverse Cation/Anion Exchange Engineering. *ACS Appl. Mater. Interfaces*, 2018, 10, 11739-11746.

Chapter 4

20. Nedelcu, G.; Protesescu, L.; Yakunin, S.; Bodnarchuk, M. I.; Grotevent, M.; Kovalenko, M. V., Fast Anion-exchange in Highly Luminescent Nanocrystals of Cesium Lead Halide Perovskites (CsPbX₃, X=Cl, Br, I). *Nano Lett.*, 2015, 15, 5635-5640.
21. Akkerman, Q. A.; D’Innocenzo, V.; Accornero, S.; Scarpellini, A.; Petrozza, A.; Prato, M.; Manna, L., Tuning the Optical Properties of Cesium Lead Halide Perovskite Nanocrystals by Anion Exchange Reactions. *J. Am. Chem. Soc.*, 2015, 137, 10276-10281.
22. Li, F.; Xia, Z. G.; Gong, Y.; Gu, Lin.; Liu, Q. L., Optical properties of Mn²⁺ doped Cesium Lead Halide Perovskite Nanocrystals via Cation-anion Co-substitution Exchange Reaction. *J. Mater. Chem. C.*, 2017, 5, 9281-9287.
23. Diroll, B. T.; Nedelcu, G.; Kovalenko, M. V.; Schaller, R. D., High-Temperature Photoluminescence of CsPbX₃ (X = Cl, Br, I) Nanocrystals. *Adv. Funct. Mater.*, 2017, 27, 1606750-1606756.
24. Noel, N. K.; Abate, A.; Stranks, S. D.; Parrott, E. S.; Burlakov, V. M.; Goriely, A.; Snaith, H. J. Enhanced Photoluminescence and Solar Cell Performance via Lewis Base Passivation of Organic–inorganic Lead Halide Perovskites. *ACS Nano*, 2014, 8, 9815-9821.
25. Liu, P.; Chen, W.; Wang, W.; Xu, B.; Wu, D.; Hao, J.; Cao, W.; Fang, F.; Li, Y.; Zeng, Y.; Pan, R.; Chen, S.; Cao, W.; Sun, X. W.; Wang, K., Halide-rich Synthesized Cesium Lead Bromide Perovskite Nanocrystals for Light-emitting Diodes with Improved Performance. *Chem. Mater.*, 2017, 29, 5168-5173.
26. Stasio, F. D.; Christodoulou, S.; Huo, N.; Konstantatos, G., Near-Unity Photoluminescence Quantum Yield in CsPbBr₃ Nanocrystal Solid-State Films via Postsynthesis Treatment with Lead Bromide. *Chem. Mater.*, 2017, 29, 7663-7667.
27. Zhang, D.; Yang, Y.; Bekenstein, Y.; Yu, Y.; Gibson, N. A.; Wong, A. B.; Eaton, S. W.; Kornienko, N.; Kong, Q.; Lai, M.; Alivisatos, P. A.; Leone, S. R.; Yang, P. Synthesis of Composition Tunable and Highly Luminescent Cesium Lead Halide Nanowires Through Anion-exchange Reactions. *J. Am. Chem. Soc.*, 2016, 138, 7236-7239.
28. Dirin, D. N.; Protesescu, L.; Trummer, D.; Kochetygov, I. V.; Yakunin, S.; Krumeich, F.; Stadie, N. P.; Kovalenko, M. V., Harnessing Defect-tolerance at the Nanoscale: Highly Luminescent Lead Halide Perovskite Nanocrystals in Mesoporous Silica Matrices. *Nano Lett.*, 2016, 16, 5866-5874.
29. Malgras, V.; Tominaka, S.; Ryan, J. W.; Henzie, J.; Takei, T.; Ohara, K.; Yamauchi, Y., Observation of Quantum Confinement in Monodisperse Methylammonium Lead Halide Perovskite Nanocrystals Embedded in Mesoporous Silica. *J. Am. Chem. Soc.*, 2016, 138,

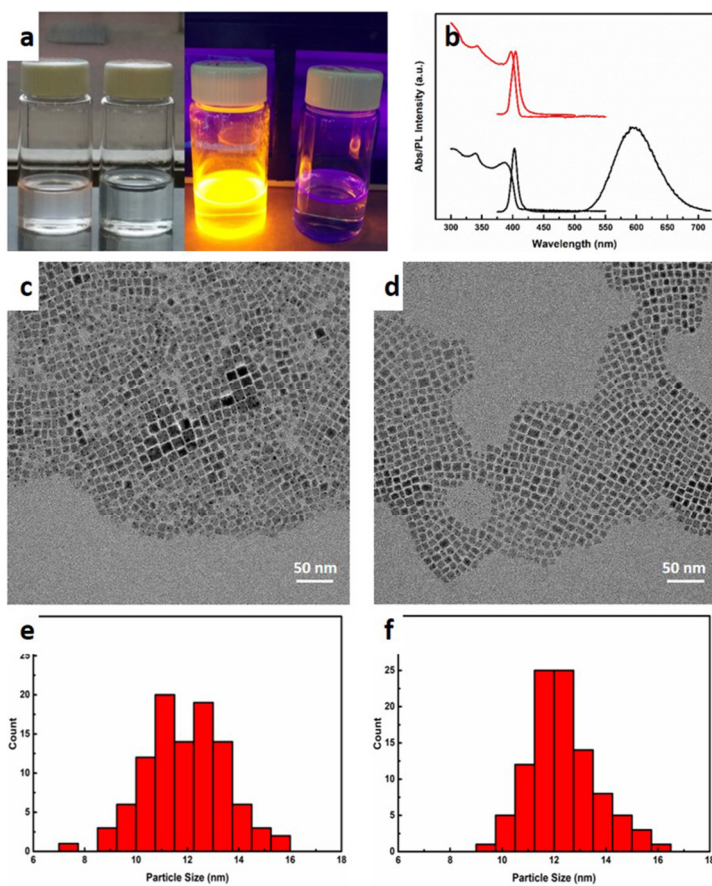
13874-13881.

30. Vlaskin, V. A.; Barrows, C. J.; Erickson, C. S.; Gamelin, D. R. Nanocrystal Diffusion Doping. *J. Am. Chem. Soc.*, 2013, *135*, 14380-14389.
31. Beaulac, R.; Ochsenbein, S. T.; Gamelin, D. R. Colloidal Transition Metal-Doped Quantum Dots. In *Nanocrystal Quantum Dots*, Second Edition; Klimov, V. I.; CRC Press: Boca Raton, USA, 2010; 432-433.
32. Vlaskin, V. A.; Janssen, N.; van Rijssel, J.; Beaulac, R.; Gamelin, D. R. Tunable Dual Emission in Doped Semiconductor Nanocrystals. *Nano Lett.*, 2010, *10*, 3670-3674.
33. Beaulac, R.; Archer, P. I.; van Rijssel, J.; Meijerink, A.; Gamelin, D. R. Exciton Storage by Mn^{2+} in Colloidal Mn^{2+} -Doped CdSe Quantum Dots. *Nano Lett.*, 2008, *8*, 2949-2953.
34. Becker, M. A.; Vaxenburg, R.; Nedelcu, G.; Sercel, P. C.; Shabaev, A.; Mehl, M. J.; Michopoulos, J. G.; Lambrakos, S. G.; Bernstein, N.; Lyons, J. L.; Stöferle, T.; Mahrt, R. F.; Kovalenko, M. V.; Norris, D. J.; Rainò, G.; Efros, A. L. Bright Triplet Excitons in Caesium Lead Halide Perovskites. *Nature.*, 2018, *553*, 189-193.
35. Joos, J. J.; Poelman, D.; Smet, P. F. Energy Level Modeling of Lanthanide Materials: Review and Uncertainty Analysis. *Phys. Chem. Chem. Phys.*, 2015, *17*, 19058-19078.
36. Rogers, E. G.; Dorenbos, P. Vacuum Referred Binding Energy of the Single 3d, 4d, or 5d Electron in Transition Metal and Lanthanide Impurities in Compounds. *ECS J. Solid State Sci. Technol.*, 2014, *3*, R173-R184.
37. Dorenbos, P. Absolute Location of Lanthanide Energy Levels and the Performance of Phosphors. *J. Lumin.*, 2007, *122*, 315-317.
38. Varshni, Y.P. Temperature Dependence of the Energy Gap in Semiconductors. *Physica*, 1967, *34*, 149-154.
39. Shinde, A.; Gahlaut, R.; Mahamuni, S. Low-Temperature Photoluminescence Studies of CsPbBr₃ Quantum Dots. *J. Phys. Chem. C*, 2017, *121*, 14872-14878.

Chapter 4

Supporting Information

Chapter 4. Tuning Exciton-Mn²⁺ Energy Transfer in Mixed Halide Perovskite Nanocrystals



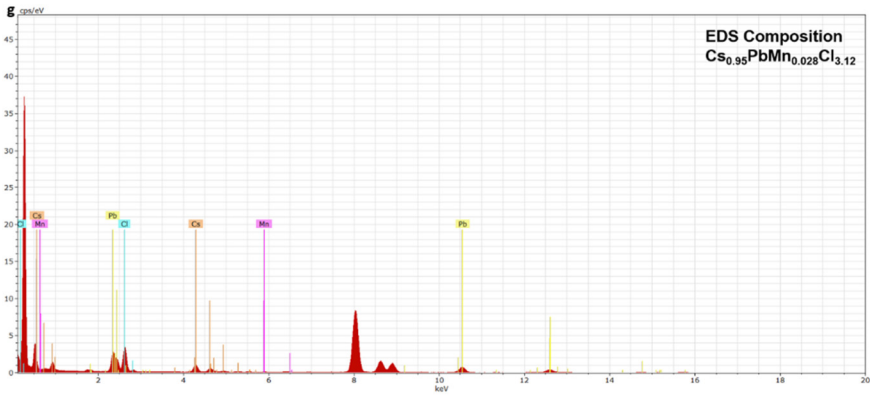


Figure S4.1. (a) Photographs of Mn^{2+} -doped and undoped CsPbCl_3 NCs under day light (left) and 365 UV light (right) (b) Absorption and emission spectra of doped (bottom, black) and undoped (top, red) CsPbCl_3 NCs ($\lambda_{\text{ex}}=355$ nm). (c, d) TEM images of Mn-doped (left) and undoped (right) CsPbCl_3 NCs. (e, f) Size histogram of Mn-doped (left) and undoped (right) CsPbCl_3 NCs. (g)EDX spectrum of Mn doped CsPbCl_3 NCs

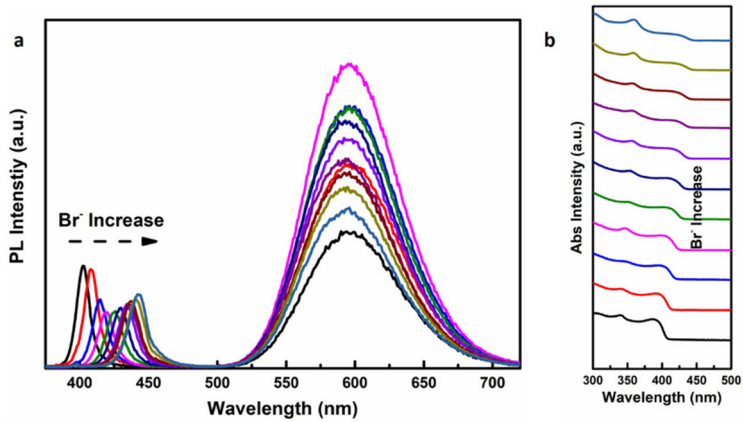


Figure S4.2. (a) Evolution of emission spectrum as the function of Br^- content at 300 K (The spectrum is calibrated with the respective absorption coefficient at excitation wavelength, $\lambda_{\text{ex}}=355$ nm). (b) Evolution of absorption spectrum as the function of Br^- content at 300 K.

Chapter 4

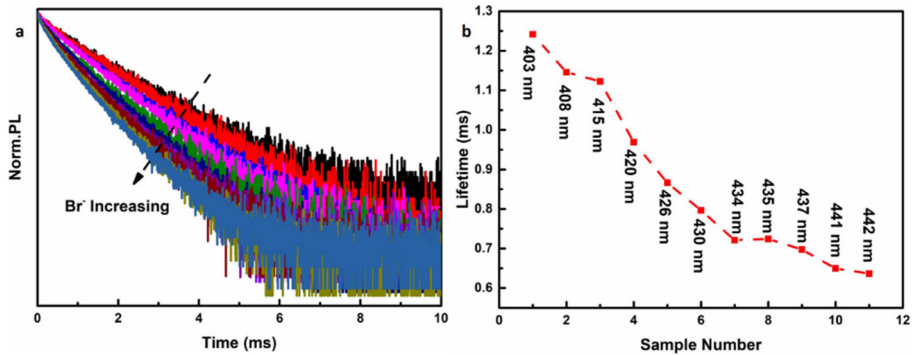


Figure S4.3. (a) Evolution of decay curves the Mn^{2+} emission in of Mn^{2+} -doped $CsPbCl_{3-x}Br_x$ for different x values ($\lambda_{ex}=355$ nm, 10 Hz) and (b) effective Mn^{2+} emission decay times determined from the decay curves in Figure S4.3a.

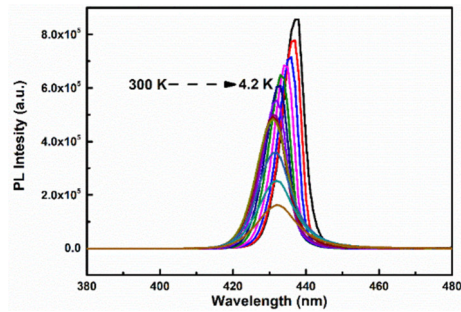


Figure S4.4. Evolution of the exciton emission for $CsPbCl_{3-x}Br_x$ with an emission wavelength of 432 nm (300 K) as the function of temperature down to 4.2 K ($\lambda_{ex}=355$ nm).

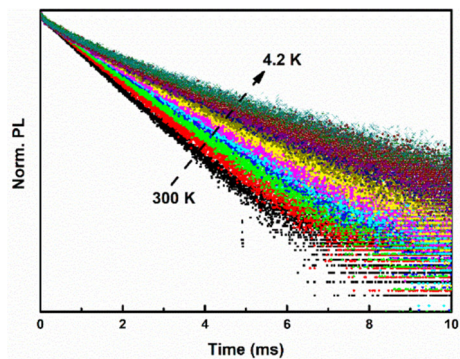


Figure S4.5. Mn^{2+} emission decay curves for the sample with an emission wavelength of 430 nm (300 K) as the function of temperature ($\lambda_{\text{ex}}=355$ nm, 10 Hz)

Chapter 5

Long-lived Dark Exciton Emission in Mn-doped CsPbCl₃ Perovskite Nanocrystals

Abstract

The unusual temperature dependence of exciton emission decay in CsPbX₃ perovskite nanocrystals (NCs) attracts considerable attention. The room temperature lifetime is much shorter than in traditional quantum dots (QDs) which is beneficial for potential applications. Upon cooling extremely short (sub-ns) lifetimes are observed below 20 K which has been explained by an inverted bright-dark state splitting. Here we report temperature dependent exciton life times for CsPbCl₃ NCs doped with 0 to 41% Mn²⁺. The exciton emission life time increases upon cooling from 300 to 75 K. Upon further cooling a strong and fast sub-ns decay component develops. However, the decay is strongly bi-exponential and a weak slow decay component is observed with a ~40-50 ns life time below 20 K. These observations are similar to previous experiments for CsPbX₃ NCs in high magnetic fields. The slow component has a much stronger relative intensity in Mn-doped NCs compared to undoped CsPbCl₃ NCs. The temperature dependence of the slow decay component resembles that of CdSe and PbSe QDs with an activation energy of ~19 meV for the dark-bright state splitting. Based on our observations we propose an alternative explanation for the fast sub-ns exciton decay time in CsPbX₃ NCs. Slow bright-dark state relaxation at cryogenic temperatures gives rise to almost exclusively bright state emission. Incorporation of Mn²⁺ or high magnetic fields enhances the bright-dark state relaxation and allow for the observation of the long-lived dark state emission at cryogenic temperatures.

5.1 Introduction

The discovery of CsPbX₃ (X=Cl, Br, I) nanocrystals (NCs) with unique optical properties has initiated a worldwide increase in research aimed at providing fundamental understanding of their peculiar properties and at realizing applications of these NCs, e.g. in lighting and solar cells¹⁻⁴. The optical properties of the CsPbX₃ NCs resemble those of Cd- and Pb-chalcogenide quantum dots (QDs). Bulk CsPbX₃ is a semiconductor and in the NCs which are typically ~10-15 nm the exciton is confined. The NC size is however larger than the exciton Bohr radius (varying from 2.5 nm in CsPbCl₃ to 6 nm in CsPbI₃) giving rise to weak confinement and only small shifts of the exciton emission wavelength⁵. Tuning of the emission color is therefore not realized by size variation but by changing the chemical composition. The emission color of CsPbX₃ NCs can span the full visible region through anion exchange. Replacing Cl⁻ by Br⁻ shifts the emission from violet to green and subsequent replacement by I⁻ shifts the emission further to the deep red spectral region. Additional color tuning can be realized by doping with luminescent ions (typically 3d transition metal and 4f rare earth ions) and energy transfer of the exciton to the luminescent dopant⁶⁻⁹. For applications of the perovskite NCs in light emitting devices not only the high quantum yield (>90%) and color tunability are advantageous, also the emission life time is short, typically in the ns range at room temperature. The faster emission decay in comparison with e.g. CdSe and InP QDs has advantages in high brightness applications. The limited stability of the perovskite NCs is a point of concern that is addressed by passivation strategies but at present hampers application^{10, 11}.

In recent papers the temperature dependence of the exciton emission life time was investigated for CsPbX₃ NCs. Both for ensemble and individual NCs an unexpected temperature dependence was observed: upon cooling to cryogenic temperatures the already short decay time decreased even further to sub-ns lifetime^{12, 13}. This behaviour is markedly different from that of the traditional Cd- and Pb- chalcogenide QDs. Typically, upon cooling the exciton life time lengthens because of the energy level structure of the emitting exciton states where the lowest energy state is a dark state which has a forbidden transition to the exciton ground state^{14, 15}. In well-passivated QDs the emission from the dark state is still efficient (so the state is not really dark) but the forbidden nature causes the emission life time to lengthen when the system is frozen into this lowest excitonic state. For CsPbX₃ perovskite NCs the opposite behaviour was observed and explained by inversion of the

dark-bright state splitting induced by the Rashba effect¹². As a result, fast bright state emission is observed at 4 K and theoretical calculations also were able to explain the short sub-ns life time. However, also alternative observations were reported. Luminescence decay measurements for CsPbBr₃ and FAPbBr₃ in high magnetic fields revealed a composition dependent dark-bright state splitting with a lowest exciton dark state¹⁶.

Here we report temperature dependent luminescence life time measurements for exciton emission in Mn-doped CsPbCl₃ NCs. For different Mn-doping concentrations we observe a clear lengthening of the exciton decay time upon cooling. Below 200 K a rise time is observed for the exciton emission which indicates that relaxation rates from higher exciton levels to the emitting levels slow down upon cooling. Upon further cooling, below 50 K, a bi-exponential decay is observed with a strong fast component (<1 ns) and a slow component that becomes longer lived upon lowering the temperature. The temperature dependence of this slow component shows the typical behaviour expected for a dark-bright state splitting with a lower energy dark state. As an alternative an inverted dark-bright splitting we propose that inhibited relaxation from bright to dark state explains the observation of fast bright state emission in CsPbX₃ NCs at cryogenic temperatures.

5.2 Experimental Section

Chemicals: All the chemicals were obtained from Sigma Aldrich, i.e. Cesium carbonate (Cs₂CO₃), lead chloride (PbCl₂), manganese chloride (MnCl₂*4H₂O), octadecene (ODE), oleic acid (OA), oleylamine (OM), hexane (anhydrous).

Preparation of the Cesium Precursor: 0.2 g Cs₂CO₃ was mixed with 7.5 ml ODE and 0.625 ml OA and loaded into a 50 ml flask, degassed and dried under 120 °C for 30 min under vacuum, and then heated at 150 °C under N₂ atmosphere for an additional 30 min to complete the reaction between Cs₂CO₃ and OA. The resulting solution was kept at 150 °C for further use.

Preparation of Pure CsPbCl₃ NCs and CsPbCl₃: Mn²⁺ NCs: pure CsPbCl₃ NCs and CsPbCl₃: Mn²⁺ NCs with different dopant concentrations were synthesized at a temperature of 190 °C with various Mn/Pb feeding ratio (see Table 5.1)

Chapter 5

Table 5.1. Precursor composition (Mn/Pb ratio in reaction mixture) for synthesis of CsPbCl₃: Mn²⁺ NCs with various Mn-doping concentrations and the actual Mn-concentration incorporated in the CsPbCl₃ NCs as determined from EDX analysis.

Mn/Pb molar ratio	0	0.5	1	2	3	4	5
Mn in sample (at.%)	0	1	3	9	20	32	41

For a typical synthesis, 0.1 g PbCl₂ and 0.037 g MnCl₂*4H₂O were loaded into a 50 ml three neck flask with 10 ml ODE. The flask was then transferred to a Schlenk line and the reaction mixture was dried at 120 °C under vacuum for 1h. 1 ml dried OA and OM were subsequently injected and then heated to 190 °C, all under a N₂ atmosphere. After reaching 190 °C, 0.9 ml of the hot Cs precursor was injected swiftly. The reaction was quenched 5s later by immersion of the reaction container in an ice-water bath. The product was separated by centrifuging washed once with acetone/hexane and finally dissolved in 5 ml hexane.

Characterization

Transmission electron microscopy (TEM) images were made with a FEI TECNAI T20, operating at 200 kV. The samples for TEM imaging were prepared by dipping a carbon-coated copper mesh TEM grid into a hexane solution of NCs. The excess liquid was evaporated under vacuum.

Luminescence (emission and excitation) spectra and photoluminescence (PL) decay curves were measured using an Edinburgh Instruments FLS920 spectrofluorometer equipped with a 450 W Xenon lamp as excitation source and a 0.22 m double grating monochromator for excitation (Bentham DTMS300, 1200 lines/mm grating, blazed at 300 nm for excitation). Emission spectra (380-700 nm) were recorded with a single 0.22 m monochromator (500 nm blazed grating) and the emitted light was detected by a Hamamatsu R928 photomultiplier tube (PMT). The fast decay profiles of the exciton emission were recorded using an Edinburgh EPL375 pulsed diode laser ($\lambda_{\text{ex}} = 376.8$ nm, pulse width: 65 ps) with a fast Hamamatsu H74422-40 PMT. An Oxford Instruments liquid helium flow cryostat was used to measure the PL properties at low temperatures (down to 4.2 K). The samples for room temperature optical analysis were prepared by dissolving the crude NCs mixture in

hexane and transferring the solution to the quartz cuvette. For low temperature measurement, the NC solution was loaded in a sealed quartz cuvette.

5.3 Results and Discussion

CsPbCl₃ NCs doped with Mn²⁺ were prepared using a hot injection method as described above. The actual amount of Mn incorporated in the CsPbCl₃ NCs was always much lower than that in the reaction mixture, which is typically observed for doping of ions in QDs. TEM images of the NCs are shown in Figure 5.1 and show that cubic NCs are formed with a size of ~12 nm. The NCs show bright luminescence with a sharp excitonic emission line around 400 nm and a broad Mn²⁺ emission band around 600 nm. The emission spectra in Figure 5.1 show that the relative intensity of the Mn²⁺ emission band increases and shifts to longer wavelengths for higher Mn²⁺ concentrations. Upon cooling the relative intensity of the Mn²⁺ emission strongly decreases from 300 K to 150 K. Below 75 K the relative Mn-emission intensity increases again, but it remains much lower than at 300 K (Supporting Information, Figure S5.1 and S5.2). This temperature behaviour is consistent with reports in the literature and reflects the temperature dependence of the exciton-to-Mn²⁺ energy transfer (ET) rate relative to processes giving rise to exciton emission^{17, 18}.

Luminescence decay curves were recorded for both the exciton and Mn²⁺ emission between 4.2 K and 300 K for CsPbCl₃ NCs doped with 0, 1, 3, 9, 20, 32 and 41% of Mn²⁺. Here we focus on the exciton emission decay. As an example, Figure 5.2 displays the luminescence decay curves for the 20% Mn-doped CsPbCl₃ NCs. Three temperature regimes are depicted. Between 293 and 200 K (Figure 5.2a) the decay curves are close to single exponential. Upon cooling from 293 to 200 K the luminescence decay time lengthens from 0.1 ns at 293 K to 0.4 ns at 200 K and the intensity increases. This can be explained by less efficient exciton to Mn²⁺ energy transfer and is consistent with the strong decrease in the relative Mn²⁺ emission intensity between 293 and 200 K. Upon further cooling to 75 K the lengthening of the decay time continues (note the change in time scales from (a) to (c)). In addition, the decay curves show a clear rise with a rise time that increases from 1.8 ns at 150 K to 3.2 ns at 75 K. The observation of a rise indicates that relaxation from the higher excited states that are initially populated under pulsed excitation at 376 nm to the emitting exciton states around 400 nm slows down at cryogenic temperatures. Usually fast (10-100 ps) relaxation is observed for relaxation to band edge states in semiconductors but in the

CsPbCl₃ NCs phonon relaxation is relatively slow and upon freezing out the phonon population relaxation rates decrease to the ns regime.

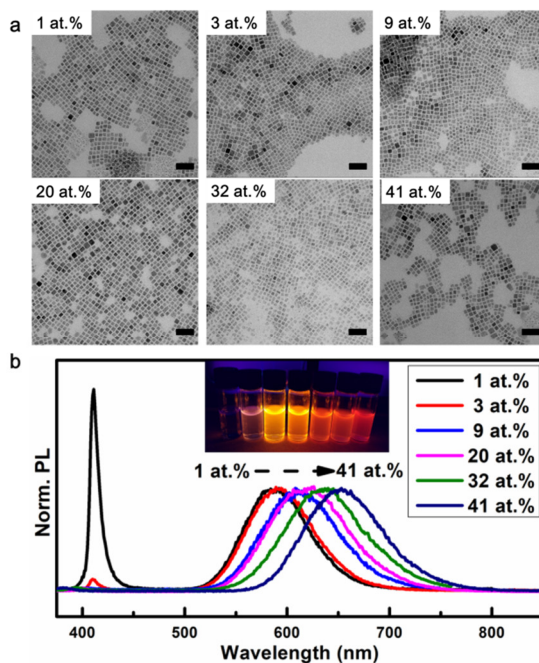


Figure 5.1. Morphology and optical properties of CsPbCl₃: Mn²⁺ (1 at.% ~ 41 at.%) NCs. (a) TEM images of CsPbCl₃: Mn²⁺ NCs with different Mn²⁺ concentration (1 at.% ~ 41 at.%, scale bar: 50 nm). (b) Emission spectra of CsPbCl₃: Mn²⁺ NCs with different Mn²⁺ concentration (1 at.% ~ 41 at.%, $\lambda_{\text{ex}} = 355$ nm, inset: sample under 365 nm excitation provided by a handheld UV lamp.)

Upon further cooling from 75 to 4 K the luminescence decay curves become strongly bi-exponential with a fast sub-nanosecond component and a slow component that lengthens as the temperature decreases from 75 to 4 K. The relative contribution of the fast component increases at lower temperatures and the decay of the slow component slows down and stabilizes below ~20 K. A similar behavior is observed for other

Mn-concentrations. As an example Figure 5.2d and 5.2e show the luminescence decay curves for the exciton emission in $\text{CsPbCl}_3:\text{Mn}^{2+}$ with 9 and 32 at.% Mn^{2+} . An overview of the temperature dependent decay behavior of all $\text{CsPbCl}_3:\text{Mn}^{2+}$ (1 at.% to 41 at.%) samples is given in the supporting information (Supporting Information, Figure S5.3 to S5.6.)

The present observations resemble those for the exciton emission in CsPbBr_3 in a magnetic field where also a fast initial decay at low temperatures was followed by a weak and slow decay component¹⁶. The fast decay component was assigned to bright state exciton emission and the slow component to dark exciton emission. Slow relaxation from the bright to the dark state exciton at low temperatures can explain the observation of short lived bright state emission decay prior to relaxation to the dark state. From the temperature dependence of the dark state emission decay time a dark-bright state splitting of ~ 8 meV was calculated for CsPbBr_3 . Also for CdSe QDs a fast initial decay related to bright state emission prior to relaxation to the dark state has been reported at temperatures below 10 K. The temperature dependent decay behavior of the exciton emission for CsPbX_3 NCs in a magnetic field and the present observations for Mn-doped CsPbCl_3 NCs can be explained by slow bright state – dark state relaxation at cryogenic temperatures. The situation is similar as that for Cd- and Pb- chalcogenide QDs but with a significant slower relaxation between excitonic states which gives rise to the observation of intense and fast (sub-ns) bright state emission which dominates at cryogenic temperatures.

To test the presence of dark state emission in pure CsPbCl_3 NCs we also measured luminescence decay curves as a function of temperature for undoped NCs. The temperature dependent behavior is similar to that observed for the Mn-doped NCs but the relative intensity of the dark state emission is much lower. As an example, Figure 5.3 shows the 35 K decay curves for the exciton emission in CsPbCl_3 NCs and $\text{CsPbCl}_3:\text{Mn}^{2+}$ (20 at.%) NCs. For both systems a fast and strong initial sub-ns decay is followed by a slow temperature dependent decay component. The amplitude for the slow component is more than three orders of magnitude smaller than that of the fast component. For CsPbCl_3 doped with 20% Mn^{2+} the decay behavior is similar but the amplitude of the slow dark state emission component is about two orders of magnitude lower. This can be explained by a faster bright state–dark state relaxation induced by the Mn^{2+} dopants. Similar observations can be found in Ref. 16 where a higher relative intensity is observed for the slow decay component of the exciton emission from CsPbBr_3 NCs in a high (10 T) magnetic field.

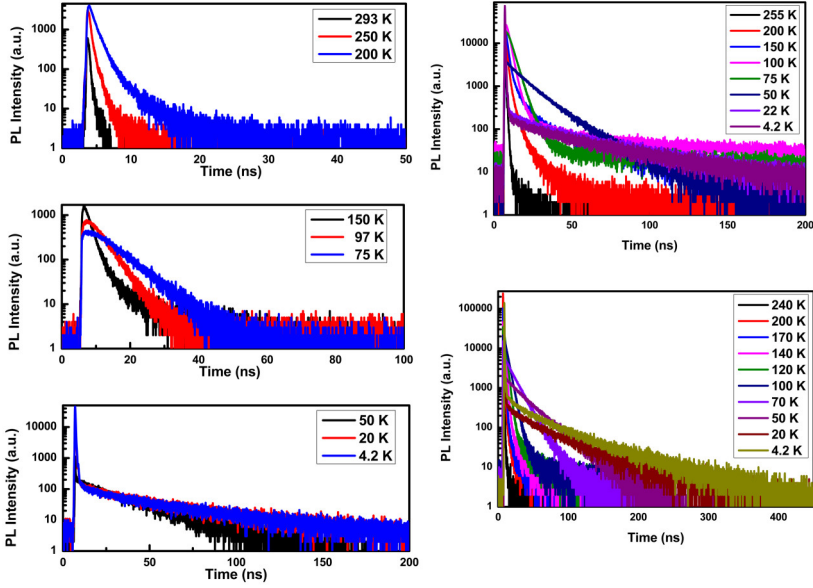


Figure 5.2. Decay curve of CsPbCl₃: Mn²⁺ (20 at.%) NCs (a-c), CsPbCl₃: Mn²⁺ (9 at.%) NCs (d) and CsPbCl₃: Mn²⁺ (32 at.%) NCs (e) at different temperatures plotted on semi-logarithmic scale ($\lambda_{\text{ex}}=376.8$ nm, pulse width: 65 ps)

This indicates that the presence of magnetic ions (Mn²⁺) or an external magnetic field induces faster relaxation between the dark and bright state. In single (undoped) dot experiments the low count rate and more than three orders of magnitude higher amplitude of the bright state emission prevents the observation of the slow dark state emission. Indeed, inspection of the single CsPbX₃ NC exciton decay curves in Ref. 12 shows that the noise level starts above 10^{-3} in the decay curves with a maximum scaled to 10^0 making it impossible to observe the slow decay component of the exciton emission.

To estimate the dark-bright state splitting, the temperature dependence of the slow decay component was analysed for CsPbCl₃ NCs with 9, 20 and 32% of Mn²⁺. The close to single exponential decay in the long time regime was fitted to exponential. The choice of the time interval for the fitting is somewhat arbitrary and introduces an uncertainty in the decay times.

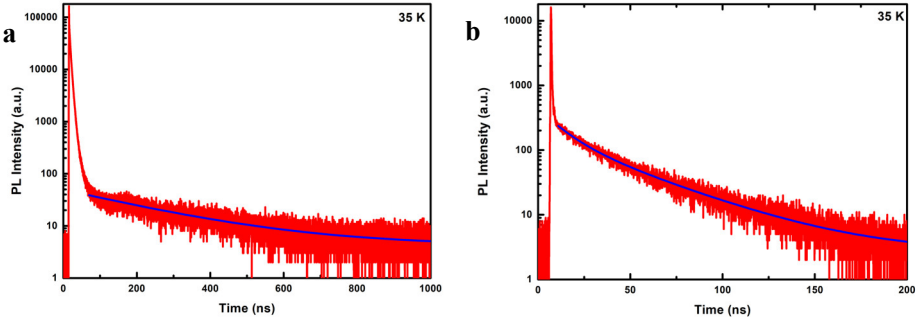


Figure 5.3. Decay curves of undoped CsPbCl₃ NCs (a) and CsPbCl₃: Mn²⁺ (20 at.%) NCs (b) at 35 K plotted on semi-logarithmic scale ($\lambda_{\text{ex}}=376.8$ nm, pulse width: 65 ps)

In Figure 5.4 the temperature dependence of the decay times is depicted. For all three samples a similar behaviour is observed. The decay time is constant around 40-50 ns between 4 and 20 K and decreases strongly between 20 and 75 K. A fit of the temperature dependence to a three-level model:

$$\frac{1}{\tau_{\text{Obs}}} = \frac{1}{\tau_D} \left(\frac{e^{\frac{\Delta E}{kT}}}{1 + e^{\frac{\Delta E}{kT}}} \right) + \frac{1}{\tau_B} \left(\frac{1}{1 + e^{\frac{\Delta E}{kT}}} \right)$$

where τ_{Obs} is the measured decay time, τ_D is the decay time of the dark state and τ_B is decay time of the bright state, gives an energy difference of ~ 19 meV for the dark-bright state splitting. This value is in good agreement with the ~ 14 meV splitting for CsPbCl₃ NCs calculated from the influence of magnetic field induced mixing of dark and bright states which influences the decay rate of the fast component of the exciton emission¹⁶.

The present results provide evidence for a normal splitting of the exciton state in CsPbCl₃ and can explain earlier observations that led to a model with an inverted dark-bright state splitting in CsPbX₃ NCs. To obtain conclusive evidence it will interesting to conduct temperature dependent life time measurements on single Mn²⁺ doped CsPbCl₃ NCs and search for weak, temperature dependent slow dark state emission in single Mn-doped NCs. The origin of the anomalous exciton decay behavior is assigned to unusually slow phonon relaxation between excitonic states in CsPbCl₃ NCs. It will be interesting to verify this slow

relaxation by other techniques, e.g. pump-probe experiments, and by theoretical calculations.

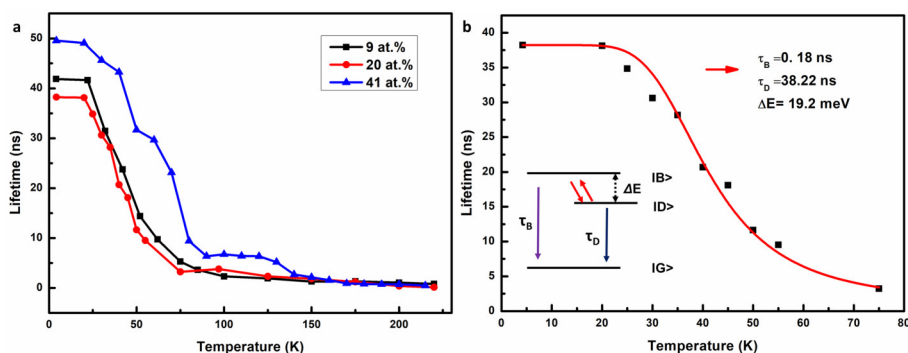


Figure 5.4. Lifetime CsPbCl₃: Mn²⁺ (9 at.%, 20 at.% and 32 at.%) NCs as function of temperature (a) Evolution of lifetime of CsPbCl₃: Mn²⁺ (9 at.%, 20 at.% and 32 at.%) NCs with temperature. (b) Three-level fitting of long decay component of CsPbCl₃: Mn²⁺ (20 at.%) NCs decay versus temperature.

5.4 Conclusions

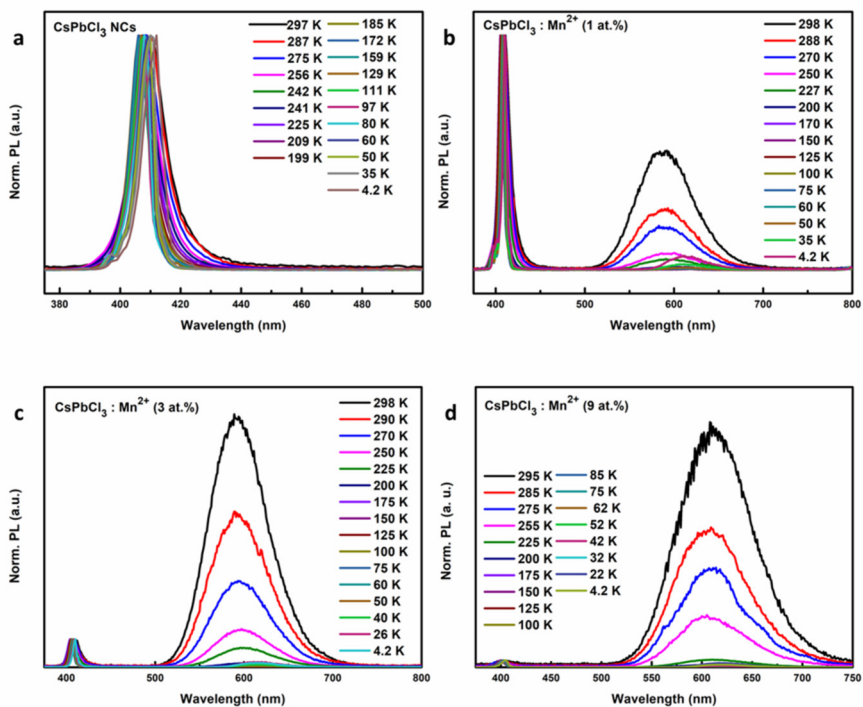
In summary, we have investigated temperature dependence of exciton decay dynamics in Mn-doped CsPbCl₃ NCs. Upon cooling initially the exciton decay time lengthens. A rise time is observed below 150 K indicating slow phonon relaxation dynamics feeding the exciton state. At temperatures below 75 K the decay becomes strongly bi-exponential with a fast decay component that is assigned to bright state emission and a weak temperature dependent slow component that is assigned to dark state emission. The results are explained by a normal exciton energy level scheme with a higher bright and lower energy dark state combined with extremely slow bright-dark state relaxation at cryogenic temperatures. In Mn-doped CsPbCl₃ NCs the relaxation is an order of magnitude faster than in undoped CsPbCl₃ which explains why the dark state emission is more easily observed in Mn-doped CsPbCl₃ NCs.

References

1. Kovalenko, M. V.; Protesescu, L.; Bodnarchuk, M. I. Properties and Potential Optoelectronic Applications of Lead Halide Perovskite Nanocrystals. *Science*, 2017, 358, 745-750.
2. Stranks, S. D.; Snaith, H. J. Metal-halide Perovskites for Photovoltaic and Light-emitting Devices. *Nat. Nanotechnol.*, 2015, 10, 391-402.
3. Akkerman, Q. A.; Rainò, G.; Kovalenko, M. V.; Manna, L. Genesis, Challenges and Opportunities for Colloidal Lead Halide Perovskite Nanocrystals. *Nat. Mater.*, 2018, 17, 394-405.
4. Veldhuis, S. A.; Boix, P. P.; Yantara, N.; Li, M.; Sum, T. C.; Mathews, N.; Mhaisalkar, S. G. Perovskite Materials for Light-Emitting Diodes and Lasers. *Adv. Mater.*, 2016, 28, 6804-6834.
5. Protesescu, L.; Yakunin, S.; Bodnarchuk, M. I.; Krieg, F.; Caputo, R.; Hendon, C. H.; Yang, R.; Walsh, A.; Kovalenko, M. V. Nanocrystals of Cesium Lead Halide Perovskites (CsPbX₃, X = Cl, Br, and I): Novel Optoelectronic Materials Showing Bright Emission with Wide Color Gamut. *Nano Lett.*, 2015, 15, 3692-3696.
6. Liu, W.; Lin, Q.; Li, H.; Wu, K.; Robel, I.; Pietryga, J. M.; Klimov, V. I. Mn²⁺-doped Lead Halide Perovskite Nanocrystals with Dual-Color Emission Controlled by Halide Content. *J. Am. Chem. Soc.*, 2016, 138, 14954-14961.
7. Xu, K.; Lin, C. C.; Xie, X.; Meijerink, A. Efficient and Stable Luminescence from Mn²⁺ in Core and Core-isocrystalline Shell CsPbCl₃ Perovskite Nanocrystals. *Chem. Mater.*, 2017, 29, 4265-4272.
8. Milstein, T. J.; Kroupa, D. M.; Gamelin, D. R. Picosecond Quantum Cutting Generates Photoluminescence Quantum Yields Over 100% in Ytterbium-Doped CsPbCl₃ Nanocrystals. *Nano Lett.*, 2018, 18, 3792-3799.
9. Pan, G.; Bai, X.; Yang, D.; Chen, X.; Jing, P.; Qu, S.; Zhang, L.; Zhou, D.; Zhu, J.; Xu, W.; Dong, B.; Song, H. Doping Lanthanide into Perovskite Nanocrystals: Highly Improved and Expanded Optical Properties. *Nano Lett.*, 2017, 17, 8005-8011.
10. Diroll, B. T.; Nedelcu, G.; Kovalenko, M. V.; Schaller, R. D. High-Temperature Photoluminescence of CsPbX₃ (X = Cl, Br, I) Nanocrystals. *Adv. Funct. Mater.*, 2017, 27, 1606750-1606756.

11. Chen, D.; Fang, G.; Chen, X. Silica-Coated Mn-doped CsPb(Cl/Br)₃ Inorganic Perovskite Quantum Dots: Exciton-to-Mn Energy Transfer and Blue-Excitable Solid-State Lighting. *ACS Appl. Mater. Interfaces*, 2017, 9, 40477-40487.
12. Becker, M. A.; Vaxenburg, R.; Nedelcu, G.; Sercel, P. C.; Shabaev, A.; Mehl, M. J.; Michopoulos, J. G.; Lambrakos, S. G.; Bernstein, N.; Lyons, J. L.; Stöferle, T.; Mahrt, R. F.; Kovalenko, M. V.; Norris, D. J.; Rainò, G.; Efros, A. L. Bright Triplet Excitons in Caesium Lead Halide Perovskites. *Nature*, 2018, 553, 189-193.
13. Rainò, Gabriele.; Nedelcu, G.; Protesescu, L.; Bodnarchuk, M. I.; Kovalenko, M. V.; Mahrt, R. F.; Stöferle, T. Single Cesium Lead Halide Perovskite Nanocrystals at Low Temperature: Fast Single-Photon Emission, Reduced Blinking, and Exciton Fine Structure. *ACS Nano*, 2016, 10, 2485-2490.
14. Sercel, P. C.; Efros, A. L. Band-Edge Exciton in CdSe and Other II–VI and III–V Compound Semiconductor Nanocrystals-Revisited. *Nano Lett.*, 2018, 18, 4061-4068.
15. Gaponenko, M. S.; Lutich, A. A.; Tolstik, N. A.; Onushchenko, A. A.; Malyarevich, A. M.; Petrov, E. P.; Yumashev, K. V. Temperature-Dependent Photoluminescence of PbS Quantum Dots in Glass: Evidence of Exciton State Splitting and Carrier Trapping. *Phys. Rev. B.*, 2010, 82, 125320.
16. Chen, L.; Li, B.; Zhang, C.; Huang, X.; Wang, X.; Xiao, M. Composition-Dependent Energy Splitting between Bright and Dark Excitons in Lead Halide Perovskite Nanocrystals. *Nano Lett.*, 2018, 18, 2074-2080.
17. Yuan, X.; Ji, S.; De Siena, M. C.; Fei, L.; Zhao, Z.; Wang, Y.; Li, H.; Zhao, J.; Gamelin, D. R. Photoluminescence Temperature Dependence, Dynamics, and Quantum Efficiencies in Mn²⁺-doped CsPbCl₃ Perovskite Nanocrystals with Varied Dopant Concentration. *Chem. Mater.*, 2017, 29, 8003-8011.
18. Xu, K.; Meijerink, A., Tuning Exciton–Mn²⁺ Energy Transfer in Mixed Halide Perovskite Nanocrystals. *Chem. Mater.*, 2018, 30, 5346-5352.

Supporting Information

Chapter 5. Long-lived Dark Exciton Emission in Mn-doped CsPbCl₃ Perovskite Nanocrystals

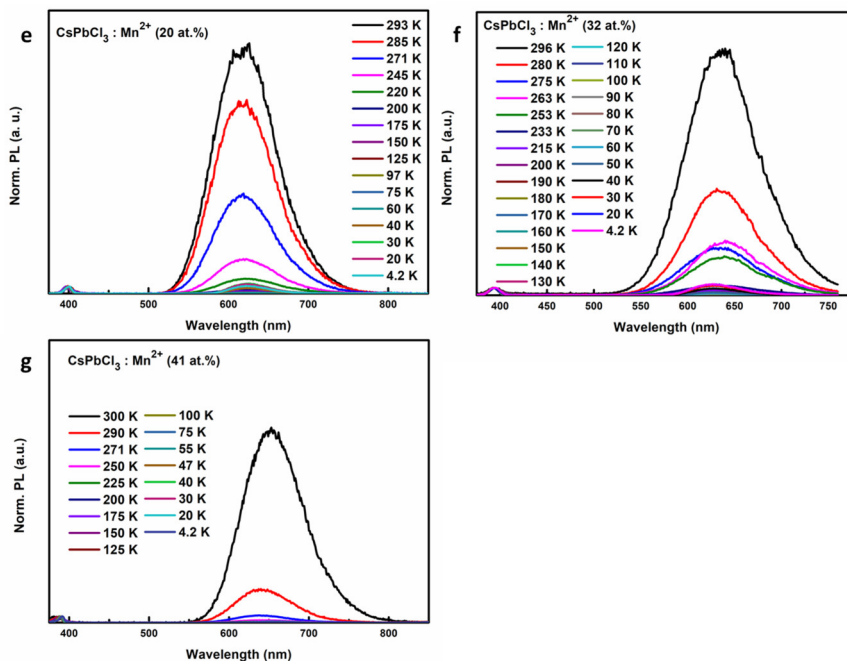


Figure S5.1. Normalized emission spectra of $\text{CsPbCl}_3: x\text{Mn}^{2+}$ ($x=0, 1 \text{ at.}\%, 3 \text{ at.}\%, 9 \text{ at.}\%, 20 \text{ at.}\%, 32 \text{ at.}\%, 41 \text{ at.}\%$) NCs at different temperatures ($\lambda_{\text{ex}}=355 \text{ nm}$)

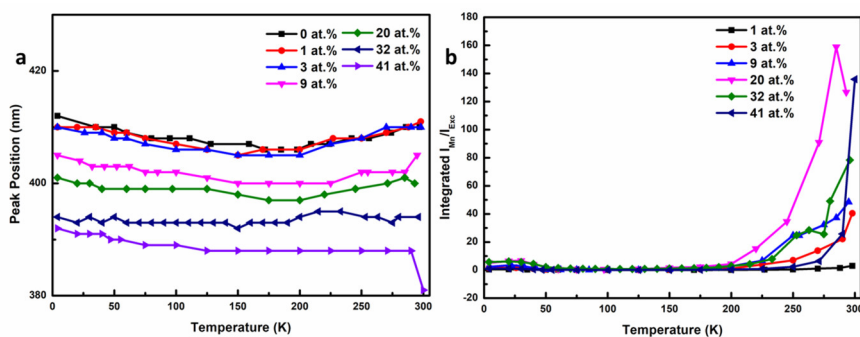


Figure S5.2. Optical properties of $\text{CsPbCl}_3: x\text{Mn}^{2+}$ ($x=0, 1 \text{ at.}\%, 3 \text{ at.}\%, 9 \text{ at.}\%, 20 \text{ at.}\%, 32 \text{ at.}\%, 41 \text{ at.}\%$). (a) Exciton peak position as a function of temperature. (b) Integrated $I_{\text{Mn}}/I_{\text{Exc}}$ at different temperatures

Chapter 5

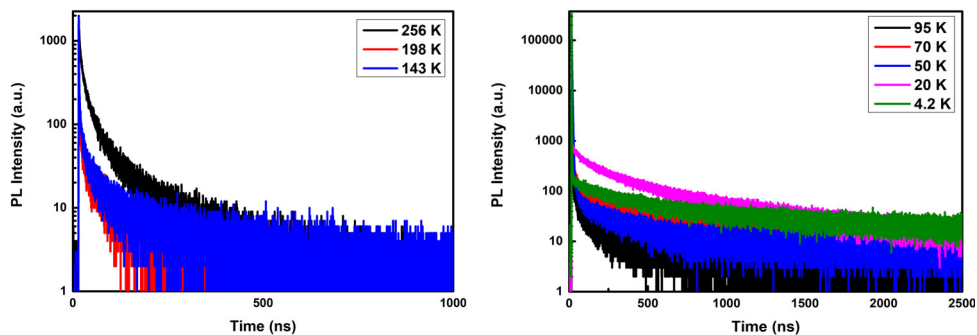


Figure S5.3. Decay curve of pure CsPbCl₃ NCs at different temperatures plotted on semi-logarithmic scale ($\lambda_{\text{ex}}=376.8$ nm, pulse width: 65 ps)

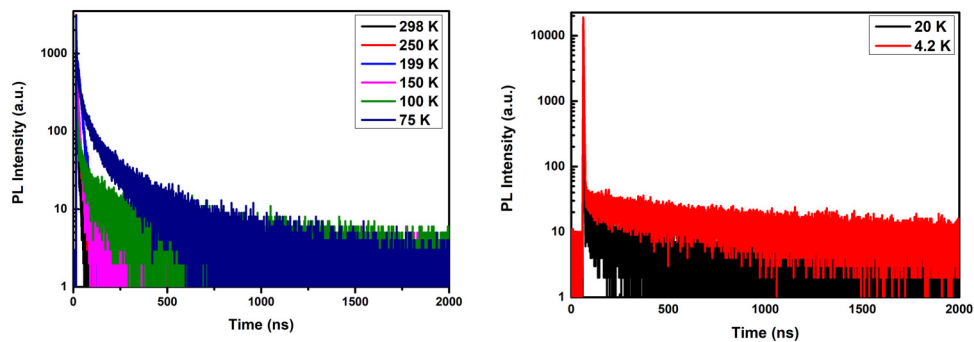


Figure S5.4. Decay of CsPbCl₃: Mn²⁺ (1 at.%) NCs at different temperatures plotted on semi-logarithmic scale ($\lambda_{\text{ex}}=376.8$ nm, pulse width: 65 ps)

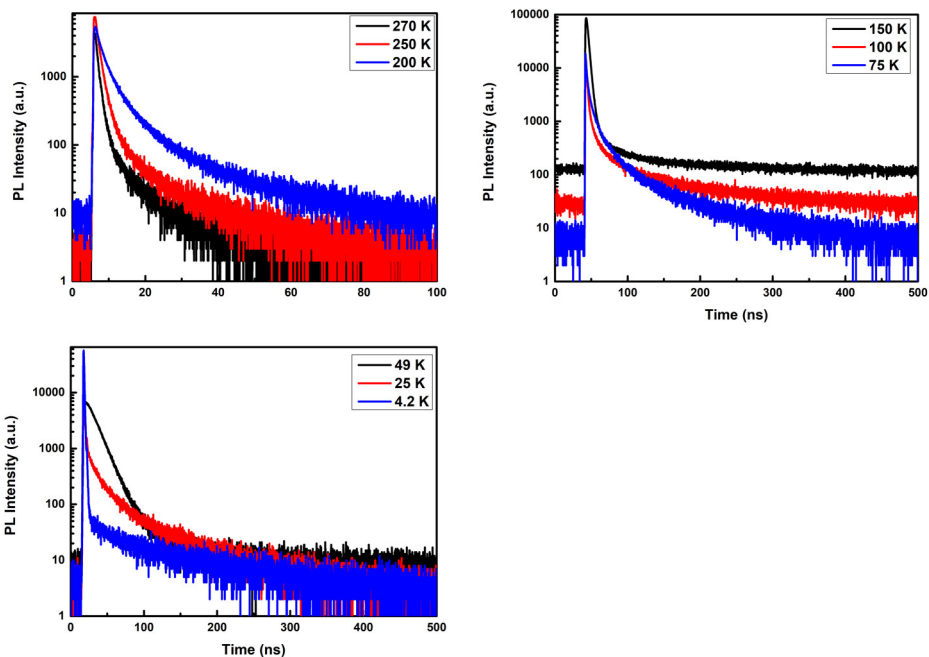


Figure S5.5. Decay curve of sample CsPbCl₃: Mn²⁺ (3 at.%) NCs at different temperatures plotted on semi-logarithmic scale ($\lambda_{\text{ex}} = 376.8$ nm, pulse width: 65 ps)

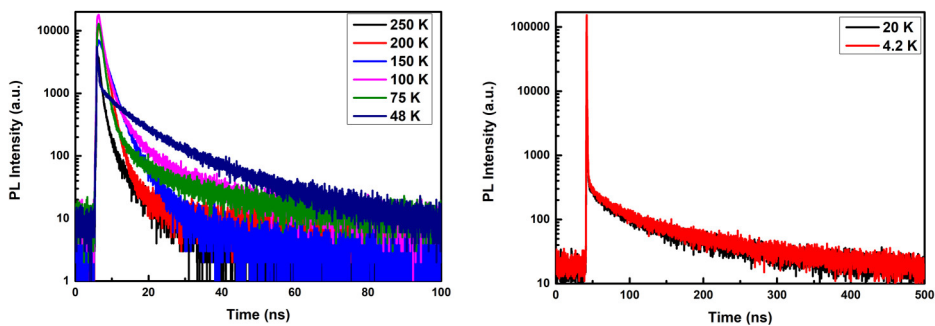


Figure S5.6. Decay curve of sample CsPbCl₃: Mn²⁺ (41 at.%) NCs at different temperatures plotted on semi-logarithmic scale ($\lambda_{\text{ex}} = 376.8$ nm, pulse width: 65 ps)

Chapter 6

Summary and Outlook

6.1 Summary

Lead halide perovskite nanocrystals (NCs) have in recent years emerged as a promising class of materials for various optoelectronic applications (LEDs, lasers, solar cells, photon detectors). Since the first publication of a new colloidal synthesis method of nanosized CsPbX_3 ($X=\text{Cl, Br, I}$) NCs the field has seen a rapidly increasing number of publications. The facile color tunability over the full visible region, high quantum yield, superior defect tolerance and versatile solution processibility, make these NCs promising candidates for achieving brighter LEDs, more efficient solar cell and low threshold lasers. The development of a facile reliable synthesis method is a prerequisite for the successful application of perovskite NCs. The large flexibility in tuning the luminescence properties of perovskite NCs through anion exchange can be extended by incorporating optical active metal ions (transition metal ions as Mn^{2+} and lanthanide ions as Eu^{3+}). Successful incorporation of luminescent ions such as Mn^{2+} ions in perovskite NCs creates an additional decay pathway which leads to an intense luminescence of these dopant (Mn^{2+}) ions. In addition, interaction of photo-generated charge carriers (excitons) in the perovskite NCs with the high magnetic moment of Mn^{2+} ($3d^5$) ions can give rise to interesting magneto-optical behavior.

In spite of the rapid increase in understanding resulting from an impressive worldwide research effort aimed at a better insight in the unique properties of perovskite nanocrystals, many fundamental issues remain which need to be solved to advance successful application and understanding of this new class of luminescent NCs. Among the issues are the limited stability of perovskite CsPbX_3 NCs, especially at elevated temperatures and under exposure to ambient atmosphere. Other fundamental questions involve the exciton fine structure and, for doped NCs, the interaction with and energy transfer to the dopant ions. The exciton fine structure has been proposed to have an inverted dark-bright state splitting in comparison to the traditional CdX or PbX ($X=\text{S, Se, Te}$) quantum dots (QDs). The energy transfer to luminescent dopant ions seems to be much less efficient than for the CdX QDs but a detailed understanding is lacking. In this thesis, both stability/synthesis issues are addressed as well as questions related to the difference in optical properties, with a strong focus on Mn^{2+} -doped CsPbX_3 NCs.

Chapter 6

In **Chapter 2** we discuss a room temperature synthesis method of bright and efficient perovskite NCs that can emit over a wide spectral region. The synthesis involves a rapid and partial aqueous approach. Fast injection of concentrated halide acid into a clear toluene solution of Pb and Cs precursors triggers the crystallization of perovskite NCs. The synthesis can be regulated by varying the concentrations of surface ligands i.e. oleylamine and oleic acid in the reaction mixture. Oleylamine and oleic acid provide control over the crystallization process and are crucial to obtain efficiently luminescing perovskite NCs with narrow size distribution. Perovskite NCs with different halide composition can be easily achieved through post-synthetic anion exchange using aqueous halide acid without sacrificing the PL efficiency. The successful synthesis of perovskite NCs in the presence of water is attributed to the fast protonation of ligands in the acid reaction mixture which leads to the formation of a tight binding ligand shell, which is also essential for the enhanced colloidal stability.

In **Chapter 3** we present a room temperature synthesis method of Mn^{2+} -doped CsPbCl_3 NCs. Analogous to the room temperature synthesis of pure perovskite NCs discussed in Chapter 2, the injection of concentrated halide acid to toluene with precursors of Pb, Cs and Mn with ligands (oleylamine and oleic acid) results in the formation of Mn^{2+} -doped CsPbCl_3 NCs. A thermodynamically controlled doping mechanism is proposed which consists of first surface adsorption of dopant ions and subsequent dopant internalization driven by the halide excess in the reaction mixture. The presence of characteristic Mn^{2+} emission (${}^4\text{T}_1 \rightarrow {}^6\text{A}_1$), the close resemblance of the excitation spectrum of Mn^{2+} emission and the absorption spectrum of CsPbCl_3 NCs host matrix provide compelling evidence for the exciton- Mn^{2+} energy transfer and successful doping of Mn^{2+} in the CsPbCl_3 NCs. Growth of an undoped isocrystalline shell on pristine Mn^{2+} -doped CsPbCl_3 NCs further internalizes dopant ions and protects Mn^{2+} ions from surface quenching processes, which enhances the photoluminescence quantum yield and thus lengthens the lifetime of Mn^{2+} emission. The core-isocrystalline shell NCs also exhibit superior thermal stability and show no thermal degradation up to at least 110 °C which is important in applications such as (high power) white light LEDs where even higher temperatures (>150 °C) are present. As will be discussed below, the temperature stability remains an important challenge for CsPbX_3 NCs.

Chapter 6

In **Chapter 4** we study dependence of the exciton-Mn²⁺ energy transfer efficiency on the halide composition (Br/Cl ratio) and temperature (4.2 K to 300 K) in Mn²⁺-doped CsPbCl_{3-x}Br_x NCs. The results reveal strong correlation between the energy transfer efficiency and Br⁻ content, which is reflected by the variation of the intensity ratio of the orange Mn²⁺ emission and the violet/blue exciton emission. Upon Br⁻ substitution, the relative emission intensity of Mn²⁺ exhibits an initial increase followed by a decrease for even higher Br⁻ contents. The results are rationalized by a slower exciton decay rate and faster exciton-to-Mn²⁺ ET at higher Br⁻ ratio. This can explain the initial increase of the Mn²⁺ emission intensity with Br⁻-content. Further increasing the Br⁻ substitution narrows the host bandgap further and gives rise to energy back energy transfer from Mn²⁺ to the CsPbCl_{3-x}Br_x host when the host bands become close to resonant with the Mn²⁺ excited state. Back transfer leads to a reduction in Mn²⁺ emission. Further evidence for the back energy transfer was provided by temperature dependent measurements as the highest Mn²⁺-to-exciton emission intensity ratio is reached at higher Br⁻ content at 4.2 K where thermally activated back transfer is suppressed. The results presented provide a new avenue to tune the exciton-Mn²⁺ energy transfer and give insight in the position of the excited state of Mn²⁺ relative to the host valence and conduction bands.

Chapter 5 reports a systematic study on the temperature dependent exciton decay behaviour for CsPbCl₃ NCs doped with 0 to 41% Mn²⁺. A fundamental understanding on the exciton fine structure is critical for both theory and application. In recent publications it has been argued that the exciton structure for CsPbX₃ NCs is fundamentally different from that of the traditional semiconductor QDs CdX and PbX (X=S, Se, Te). In these II-VI and IV-VI QDs the lowest exciton state is a so-called dark exciton. The lowest exciton state is called 'dark' because the transition to the ground state is forbidden. Emission from the dark exciton state can still be efficient and the forbidden nature of the transition is evident from a long emission life time which is observed upon cooling the QDs to cryogenic temperatures. Surprisingly, for CsPbX₃ NCs a very fast sub-ns exciton life time was reported at cryogenic temperatures which was explained by a lowest energy bright state. It was also argued that the faster decay is important for high brightness applications.

In **Chapter 5** we measured the exciton emission life time in Mn²⁺-doped CsPbCl₃ NCs. Upon cooling from 300 to 75 K, a gradual lengthening of exciton lifetime is observed. Upon further cooling, a strong bi-exponential decay curve is observed, showing a sub-ns

fast decay component and a weak slow decay component that becomes longer upon cooling and reaches ~ 50 ns at 4 K. The relative intensity of the slow component is dependent on the Mn^{2+} doping level. Through strong Mn-doping the intensity of slow component of Mn doped sample is increased. Fitting the slow component of the luminescence decay curves reveals a temperature dependence that is very similar to that for the exciton emission decay times in II-VI and IV-VI QDs with a lower energy dark exciton state. The temperature dependence indicates an activation energy of ~ 19 meV for the dark-bright state splitting, which is analogous to II-VI QDs. With the present results an alternative explanation is proposed for the fast sub-ns exciton decay time in CsPbX_3 NCs at cryogenic temperatures. The strong bright state emission at low temperatures is assigned to slow bright-dark state relaxation. Incorporation of Mn^{2+} contributes to the acceleration of bright-dark state relaxation and allows for the observation of the long-lived dark state emission at cryogenic temperatures. Support for this model comes from measurements on the exciton life time for CsPbX_3 NCs in high magnetic fields where also a weak long lived decay component is observed. Clearly, further research effort is warranted to gain further insight in the exciton fine structure of perovskite NCs and the role of exciton- Mn^{2+} interaction.

6.2 Outlook

Despite the extensive research on doped (and even more on undoped) CsPbX_3 NCs, there is a number of outstanding challenges that need to be addressed. The optical properties of perovskite NCs are intriguing and vary in many aspects from those of traditional QDs. In this outlook the focus will be on issues and challenges concerning perovskite NCs doped with luminescent ions. Doped perovskites offer increased flexibility in tuning the optical properties for a variety of applications and at the same time doping can help to give new insight in the optical properties of undoped NCs, as demonstrated in Chapter 5.

Better insight in the exciton-dopant interaction is important. Compared to e.g. CdSe:Mn^{2+} the exciton-to- Mn^{2+} energy transfer is inefficient. Even at high ($>10\%$) Mn^{2+} doping concentrations, exciton emission remains relatively strong. It is not completely clear why the energy transfer efficiency is so much lower. Qualitative arguments have been given (e.g. the ionic character of the halide host) but quantitative insight is lacking. The temperature dependence of the energy transfer efficiency is also peculiar: upon cooling to ~ 70 K the transfer efficiency decreases but then increases again upon further cooling. For II-VI QDs

Chapter 6

insight in exciton-to-Mn²⁺ energy transfer has benefitted from the size tunability and bandgap engineering as well as from controlled substitution of Mn²⁺ at different position in the QD (e.g. core or shell). For perovskite NCs size control is still an issue. The current synthesis methods usually result Mn²⁺-doped CsPbCl₃ NCs with a host size around 10 nm which is larger than the bulk exciton Bohr radius (2.5 nm). Research on the exciton-Mn²⁺ interaction is thus only conducted in the weak confinement regime and exciton-Mn²⁺ interaction in the strong confinement range remains largely unexplored. The challenge to synthesize doped CsPbCl₃ NCs in the strong confinement regime is related to the low reactivity of Mn²⁺. Hence, high synthesis temperatures or reaction conditions are required which inevitably lead to the formation of large NCs. An important direction of research is to develop new room temperature synthesis methods which allow formation of effectively doped NCs in the strong confinement regime. In addition, better controlled doping methods (e.g radial doping) will provide new insights. There is already progress in making smaller perovskite NCs and given the impressive worldwide research effort in this field, it can be expected that in the coming years synthesis methods for a wider size range (2-20 nm) of monodisperse doped perovskite NCs will become available.

Exploring the optical properties of other luminescent ions doped into perovskite NCs is another interesting direction, especially for the most prominent group of luminescent ions, the lanthanides. Lanthanide (Ln) ions have been shown to be very difficult to dope into II-VI QDs such as CdSe. The tetrahedral coordination available for cations in II-VI QDs is very unfavourable for Ln³⁺ ions which only substitute on sites with six coordination or higher. The Pb²⁺ site in CsPbX₃ NCs offers (octahedral) six-coordination and can be substituted by Ln³⁺ ions. One type of Ln dopant, Yb³⁺, is receiving increasing attention. The synthesis of Yb³⁺-doped CsPbCl₃ NCs was recently reported and a cooperative type of energy transfer mechanism between exciton and two neighboring Yb³⁺ ions has been proposed. The single photon generated exciton localizes near the charge neutral Yb[•]_{Pb}-V''_{Pb}-Yb[•]_{Pb} moiety within picoseconds and forms a trapped exciton which subsequently transfers its energy to the two nearby Yb³⁺ ions. This results in emission of two IR photons from Yb³⁺. Future research on the cooperative luminescence of Yb-doped perovskite NCs can provide more insight on the exciton-Yb³⁺ energy transfer mechanism. In addition, doping perovskite NCs with other Ln-dopants will offer the possibility to combine the efficient narrow line emission of Ln-ions with the broad, strong and tunable absorption of

Chapter 6

perovskite NCs. This is highly promising for a wide variety of applications, ranging from displays and white LEDs to solar concentrators and medical imaging. Reports on Ln-doping of perovskite NCs have appeared in the past year but have not always been reproducible. It is expected that reproducible Ln-doping protocols will become available in the near future.

Finally, it is important to address the potential of applications mentioned above. Perovskites have already shown to yield surprisingly high energy conversion efficiencies in solar cells. The high luminescence quantum yield, strong light absorption and narrow band emission tuneable over the full visible spectral region make CsPbX₃ NCs promising for application in white light LEDs and displays. The short ns emission life time is beneficial for high brightness applications. Also in luminescent solar concentrators (doped) perovskite NCs in a transparent matrix may serve as efficient light converters. Crucial for these applications will be the long term stability of perovskite NCs under the demanding operating conditions in e.g. white light LEDs and solar cells. Long term (>30 000 hours for w-LEDs, >10-30 years for solar cells) operation is crucial and is a challenge for perovskite NCs. For example in white light LEDs on chip temperatures can be as high as 150-200 °C which is similar to the synthesis temperature of perovskite NCs. It may not be possible to solve the stability issues for these harsh conditions. The challenge of stability is recognized and creative synthesis group worldwide have developed encapsulation methods that have strongly improved the stability but it is still far from what is required. The stability may turn out to be the most demanding challenge and it is expected that in the coming decade it will become clear if perovskite NCs can live up to the high expectations for applications.

Chapter 6

Samenvatting in het Nederlands

Samenvatting

Loodhalogenide perovskiet nanokristallen hebben zich in de afgelopen paar jaar ontwikkeld als een veelbelovende klasse van materialen voor diverse opto-elektronische toepassingen (LED-lampen, lasers, zonnecellen, lichtdetectoren). Sinds de eerste publicatie over een nieuwe colloïdale synthesemethode voor nanometer CsPbX_3 ($X=\text{Cl, Br, I}$) nanokristallen wordt het veld gekenmerkt door een snelle stijging van het aantal publicaties. De eenvoudige wijze waarop kleurvariatie over het volledige zichtbare spectrum gerealiseerd kan worden gekoppeld aan een hoge kwantumefficiëntie, superieure tolerantie voor defecten en veelzijdige verwerkingsmogelijkheden vanuit de oplossing maken deze nanokristallen veelbelovend voor het realiseren van helderder LED-lampen, efficiëntere zonnecellen en lasers met een lage drempel voor laserwerking. De ontwikkeling van milde en betrouwbare synthesemethodes is een vereiste voor succesvolle toepassing van perovskiet nanokristallen. De hoge flexibiliteit in het variëren van de luminescentie-eigenschappen van perovskiet nanokristallen door uitwisseling van anionen kan verder verhoogd worden door optisch actieve ionen (overgangsmetaalionen zoals Mn^{2+} of lanthanide ionen zoals Eu^{3+}) in te bouwen. Daarnaast kan wisselwerking van de optisch gecreëerde ladingsdragers (excitonen) met het hoge magnetische moment van doringen als Mn^{2+} ($3d^5$) aanleiding geven tot interessante magneto-optische eigenschappen.

Ondanks het snel toenemende begrip dankzij een indrukwekkende internationale inspanning die gericht is op het verkrijgen van beter inzicht in de unieke eigenschappen van perovskiet nanokristallen, blijven er fundamentele vragen en problemen die moeten worden opgelost om succesvolle toepassing van dit nieuwe type materiaal mogelijk te maken. Een van de belangrijke problemen is de beperkte stabiliteit van CsPbX_3 nanokristallen, vooral bij hogere temperatuur en bij blootstelling aan de lucht. Andere fundamentele vragen betreffen de exciton fijnstructuur en de interactie met en energieoverdracht naar doringen. Voor de exciton fijnstructuur is in de literatuur voorgesteld dat de splitsing voor de donkere en heldere excitontoestand omgekeerd is in vergelijking met de waargenomen splitsing in de bekende CdX of PbX ($X=\text{S, Se, Te}$) quantum dots (QDs). De energieoverdracht naar luminescerende doringen lijkt veel minder efficiënt te zijn dan voor CdX QDs maar een diep begrip hiervan ontbreekt. In dit proefschrift worden zowel de stabiliteit en synthese bestudeerd alsook vragen die verband houden met verschillen in optische eigenschappen met een sterk focus op Mn^{2+} -gedoteerde CsPbX_3 nanokristallen.

In **Hoofdstuk 2** bediscussieren we een synthesemethode uitgevoerd bij kamertemperatuur voor het maken van heldere en efficiënte perovskiet nanokristallen die licht uit kunnen zenden over een breed spectraal gebied. De synthese is snel en vindt plaats in een omgeving waarin ook water aanwezig is. Snelle injectie van een geconcentreerde zure waterstofhalogenide oplossing in een heldere toluëen oplossing van Pb- en Cs-precursors initieert de kristallisatie van perovskiet nanokristallen. De synthese kan gereguleerd worden door de concentratie van liganden zoals oleylamine en oliezuur in het reactiemengsel te variëren. Oleylamine en oliezuur geven controle over het kristallisatieproces en zijn bepalend bij het verkrijgen van efficiënt luminescerende perovskiet nanodeeltjes met een nauwe grootteverdeling. Perovskiet nanokristallen met verschillende halogeen samenstelling kunnen eenvoudig verkregen worden door uitwisseling van anionen na afloop van de synthese met behulp van halogenidezuren zonder verlies van luminescentie efficiëntie. De succesvolle synthese van perovskiet nanokristallen in aanwezigheid van water wordt toegeschreven aan de snelle protonering van liganden in het zure reactiemengsel wat leidt tot de vorming van een hecht gebonden ligandschil die ook essentieel is voor de colloïdale stabiliteit.

In **Hoofdstuk 3** beschrijven we een kamertemperatuur synthesemethode voor Mn^{2+} -gedoteerde CsPbCl_3 nanokristallen. Analoog aan de kamertemperatuur synthese van ongedoteerde perovskiet nanokristallen uit Hoofdstuk 2, resulteert de injectie van geconcentreerd halogenidezuur in een toluëen precursoroplossing met Pb, Cs en Mn met liganden (oleylamine en oliezuur) in de vorming van Mn^{2+} -gedoteerde CsPbCl_3 nanokristallen. Als mechanisme voor dotering wordt een thermodynamisch gecontroleerd proces voorgesteld waarbij eerst Mn^{2+} ionen adsorberen aan het oppervlak en vervolgens worden geïnternaliseerd onder invloed van de hoge halogenide concentratie in het reactiemengsel. De aanwezigheid van karakteristieke Mn^{2+} emissie (${}^4\text{T}_1 \rightarrow {}^6\text{A}_1$) en de sterke gelijkheid van het excitatiespectrum van de Mn^{2+} emissie met het absorptiespectrum van de CsPbCl_3 nanokristallen vormen overtuigend bewijs voor exciton- Mn^{2+} energieoverdracht en voor de inbouw van Mn^{2+} in CsPbCl_3 nanokristallen. Het groeien van een ongedoteerde isokristallijne schil rond een Mn^{2+} -gedoteerde nanokristallijne CsPbCl_3 kern helpt bij het verder internaliseren van doteringsionen en beschermt de Mn^{2+} -ionen tegen oppervlakgerelateerde dovingsprocessen waardoor de luminescentie kwantumefficiëntie toeneemt alsook de levensduur van de Mn^{2+} emissie. De

kern-isokristallijne schil nanokristallen hebben ook een superieure thermische stabiliteit en vertonen geen temperatuurdooving tot ten minste 110 °C wat belangrijk is in toepassingen als hoogvermogen LED-lampen waar nog hogere temperaturen (150 °C) bereikt worden. Zoals ook verderop besproken zal worden, blijft temperatuurstabiliteit een belangrijke uitdaging voor CsPbX₃ nanokristallen.

In **Hoofdstuk 4** bestuderen we de afhankelijkheid van de exciton-Mn²⁺ energieoverdrachtsefficiëntie van de halogenide samenstelling (Br/Cl verhouding) en temperatuur (4.2 tot 300 K). De resultaten laten een sterk verband zien tussen energieoverdrachtsefficiëntie en het Br⁻ gehalte, wat tot uiting komt in een verandering van de intensiteitsverhouding van de oranje Mn²⁺ emissie en de violet/blauwe exciton emissie. Bij toenemende Br⁻ toevoeging neemt aanvankelijk de relatieve intensiteit van de Mn²⁺ emissie toe om vervolgens af te nemen voor verdergaande Br⁻ substitutie. De resultaten worden verklaard door een langzamer exciton verval en snellere exciton-Mn²⁺ energieoverdracht bij een hoger Br⁻ gehalte. Dit kan de initiële toename van de relatieve Mn²⁺ intensiteit met Br⁻-gehalte verklaren. Bij verdergaande vervanging van Cl⁻ dor Br⁻ wordt de bandafstand van het gastrooster kleiner en dit leidt tot overdracht van Mn²⁺ terug naar het CsPbCl_{3-x}Br_x grondrooster als de banden van het grondrooster resonant worden met de aangeslagen toestand van Mn²⁺. Deze terugoverdracht leidt tot een afname van de Mn²⁺ emissie. Aanvullend bewijs voor de rol van terugoverdracht komt van temperatuursafhankelijke metingen die laten zien dat de hoogste Mn²⁺-exciton emissie intensiteitsverhouding bereikt wordt bij een hogere Br⁻ concentratie bij 4.2 K waar thermisch geactiveerde terugoverdracht onderdrukt wordt. De gerapporteerde resultaten tonen een nieuwe manier om de exciton-Mn²⁺ energieoverdrachtsefficiëntie te variëren en geven inzicht in de positie van de aangeslagen toestand van Mn²⁺ ten opzichte van de valentie- en geleidingsband van het gastrooster.

Hoofdstuk 5 beschrijft een systematische studie van het temperatuursafhankelijke exciton emissieveral voor CsPbCl₃ nanokristallen gedoteerd met 0 tot 41% Mn²⁺. Fundamenteel begrip van de exciton fijnstructuur is belangrijk vanuit zowel theoretisch als praktisch oogpunt. In recente artikelen wordt beargumenteerd dat de exciton fijnstructuur in CsPbX₃ nanokristallen fundamenteel verschilt van die voor de traditionele QDs CdX en PbX (X=S, Se, Te). In deze II-VI en IV-VI QDs is de laagste exciton toestand een zogenaamd donker exciton. De laagste exciton toestand wordt ‘donker’ genoemd omdat de overgang naar de

grondtoestand verboden is. Voor CsPbX₃ nanokristallen is echter een zeer snel sub-ns luminescentieverval waargenomen voor de exciton emissie bij cryogene temperaturen wat verklaard werd door een laagstenergetische exciton toestand die helder is. Er werd tevens geopperd dat de bijbehorende snellere exciton emissie belangrijk is in toepassingen waar een hoge helderheid vereist is.

In **Hoofdstuk 5** hebben we de exciton levensduur gemeten voor Mn²⁺-gedoteerde CsPbCl₃ nanokristallen. Bij afkoelen van 300 naar 75 K wordt een geleidelijke toename van de exciton levensduur waargenomen. Bij verder afkoelen wordt de vervalcurve sterk bi-exponentieel en toont een snelle sub-ns component en een langzame vervalcomponent die langzamer wordt bij verder afkoelen en een waarde van ~50 ns bereikt bij 4 K. De relatieve intensiteit van de snelle component hangt af van de Mn²⁺ doteringsconcentratie. Door hoog te doteren met Mn²⁺ neemt de relatieve intensiteit van de langzame component toe. De temperatuursafhankelijkheid van de langzame component laat een gedrag zien dat sterk lijkt op dat voor II-VI en IV-VI QDs met een laagstenergetisch donker exciton niveau. Op basis van een fit van de temperatuursafhankelijkheid van de exciton levensduur wordt een splitsing van 19 meV berekend tussen de donkere en heldere excitontoestand wat vergelijkbaar is met waarden die gerapporteerd zijn II-VI QDs. Op basis van de nieuwe resultaten wordt een alternatieve verklaring voorgesteld voor de snelle sub-ns exciton vervaltijd voor CsPbCl₃ bij cryogene temperaturen. De sterke emissie vanuit de heldere excitontoestand bij lage temperatuur wordt toegeschreven aan een langzame relaxatie van de heldere naar de donkere excitontoestand. Inbouwen van Mn²⁺ draagt bij aan het versnellen van de helder-donker toestand relaxatie en maakt het mogelijk de langzame emissie vanuit de donkere exciton toestand waar te nemen bij cryogene temperaturen. Ondersteuning voor dit model komt uit metingen van de exciton levensduur voor CsPbX₃ nanokristallen in hoge magneetvelden waar ook een zwakke langlevende vervalcomponent wordt waargenomen. Vervolgonderzoek is vereist om verder inzicht te krijgen in de exciton fijnstructuur van perovskiet nanokristallen en de rol van exciton-Mn²⁺ wisselwerking.

Vooruitblik

Ondanks uitvoerig onderzoek aan gedoteerde (en nog meer onderzoek aan ongedoteerde) CsPbX₃ nanokristallen is er nog een aantal onopgeloste vragen die aangepakt moeten worden. De optische eigenschappen van perovskiet nanokristallen zijn intrigerend en

verschillen in diverse aspecten van die van de traditionele quantum dots (QDs). In deze vooruitblik richten we ons vooral op vragen en uitdagingen voor perovskiet nanokristallen gedoteerd met luminescerende ionen. Gedoteerde nanokristallen bieden extra flexibiliteit in het afstemmen van de optische eigenschappen voor een breed scala aan toepassingen en tegelijkertijd kan doteren helpen om nieuwe inzichten te geven in de optische eigenschappen van ongedoteerde nanokristallen, zoals aangetoond in Hoofdstuk 5.

Beter inzicht in de exciton-dotering interactie in perovskiet nanokristallen is belangrijk. In vergelijking met bijv. CdSe:Mn²⁺ is de exciton-Mn²⁺ energieoverdracht inefficiënt. Zelfs bij hoge (>10%) Mn²⁺ doteringsconcentraties blijft de exciton emissie in CsPbX₃:Mn²⁺ relatief sterk. Het is niet volledig duidelijk waarom de energieoverdrachtsefficiëntie zo veel lager is. Kwalitatieve argumenten zijn geopperd (bijv. het ionogene karakter van het halogenide gastrooster) maar kwantitatief inzicht ontbreekt. De temperatuursafhankelijkheid van de energieoverdrachtsefficiëntie is ook opmerkelijk: bij afkoelen tot 70 K neemt de efficiëntie eerst af maar deze neemt vervolgens weer toe bij verder afkoelen. Voor II-VI QDs heeft onderzoek aan exciton-Mn²⁺ energieoverdracht veel profijt gehad van het variëren van de deeltjesgrootte waardoor de bandafstand verandert en eveneens van controle over het substitueren van Mn²⁺ op verschillende posities in de QDs (bijv. in de kern of in de schil). Met de huidige synthesemethoden voor Mn²⁺-gedoteerde CsPbCl₃ nanokristallen worden typisch ~10 nm verkregen en dit is groter dan de exciton Bohr straal in bulk CsPbCl₃ (2.5 nm). Onderzoek naar de exciton-Mn²⁺ interactie is daardoor alleen verricht in het zwakke opsluitingsregime en onderzoek naar exciton-Mn²⁺ interactie in het sterke opsluitingsregime ontbreekt. De uitdaging om veel kleinere gedoteerde CsPbCl₃ nanokristallen te maken die zich in het sterke opsluitingsregime bevinden, is gerelateerd aan de lage reactiviteit van Mn²⁺. Als gevolg daarvan zijn reactietemperaturen of condities vereist die noodzakelijkerwijs leiden tot de vorming van grote nanokristallen. Een belangrijke onderzoeksrichting is het ontwikkelen van een nieuwe kamertemperatuur syntheseroute die het mogelijk maakt om kleinere gedoteerde perovskiet nanokristallen te maken die zich in het sterke kwantumopsluitingsregime bevinden. Daarnaast kan ook een betere beheersing van doteringsmethodes (bijv. doteren in een specifieke schil) nieuwe inzichten verschaffen. Er wordt al vooruitgang geboekt bij het synthetiseren van kleinere perovskiet nanokristallen en gezien de indrukwekkende wereldwijde onderzoeksinspanning op dit gebied kan het verwacht worden dat in de komende jaren syntheseroutes ontwikkeld

zullen worden voor breed deeltjesgrootte gebied (2-20nm) voor monodisperse gedoteerde perovskiet nanokristallen.

Onderzoek naar andere luminescerende ionen gedoteerd in perovskiet nanokristallen is een andere interessante onderzoeksrichting, vooral voor de meest prominente groep van luminescerende ionen: de lanthaniden. Lanthaniden (Ln) zijn erg lastig te doteren in II-VI halfgeleiders zoals CdSe. De tetraëder coördinatie voor kationen in dit rooster is zeer ongunstig voor Ln ionen die alleen substitueren op roosterplaatsen met zes coördinatie of hoger. The Pb^{2+} plaats in $CsPbX_3$ nanokristallen heeft (octaëder) zes coordinatie en kan gebruikt worden voor substitutie met Ln^{3+} ionen. Eén type Ln dotering, Yb^{3+} , staat bijzonder in de belangstelling. De synthese van Yb^{3+} gedoteerde $CsPbCl_3$ nanokristallen is recent gerapporteerd en er is een coöperatief energieoverdrachtsmechanisme voorgesteld van het exciton naar twee naburige Yb^{3+} ionen. Het exciton dat ontstaat na absorptie van een foton lokaliseert nabij een $Yb_{Pb}^{\bullet}-V_{Pb}''-Yb_{Pb}^{\bullet}$ eenheid op een picoseconde tijdschaal en vormt een ingevangen exciton dat vervolgens de energie overdraagt naar de twee naburige Yb^{3+} ionen. Dit geeft aanleiding tot emissie van twee infrarood fotonen door de Yb^{3+} ionen. Vervolgonderzoek naar coöperatieve luminescentie van Yb-gedoteerde perovskiet nanokristallen kan beter inzicht geven in exciton- Yb^{3+} energieoverdracht. Daarnaast biedt het doteren van andere lanthanide ionen in perovskiet nanokristallen de mogelijkheid om de brede, sterke en afstembare absorptie van perovskiet nanokristallen te combineren met de efficiënte scherpe lijn emissie van Ln-ionen. Dit is veelbelovend voor een breed scala aan toepassingen, van beeldschermen en witte LED-lampen tot zonnecellen en medische beeldvorming. Verschillende publicaties over Ln-dotering van perovskiet nanokristallen zijn in het afgelopen jaar verschenen maar zijn niet altijd reproduceerbaar. Naar verwachting zullen reproduceerbare Ln-doteringsvoorschriften in de nabije toekomst beschikbaar komen.

Tenslotte is het belangrijk nader in te gaan op de kans op realisatie van de diverse toepassingen die hierboven genoemd worden. Perovskieten hebben al laten zien dat er verrassend hoge efficiënties gehaald kunnen worden in zonnecellen. De hoge luminescentie kwantumefficiëntie, sterke bandabsorptie en smalbandige afstembare emissie over het hele zichtbare spectrum maken $CsPbX_3$ nanokristallen veelbelovend voor toepassing in beeldschermen en witte LED-lampen. De korte ns levensduur van de emissie biedt voordelen in toepassingen waar een hoge helderheid vereist is. Ook in luminescente

zonneconcentratoren kunnen (gedoteerde) perovskiet nanokristallen in een transparante matrix gebruikt worden als efficiënte lichtomzetters. In al deze toepassingen speelt de lange termijn stabiliteit van perovskiet nanokristallen een cruciale rol. Lange bedrijfstijden (>30 000 uur voor witte LED-lampen, >10-30 jaar voor zonnecellen) zijn vereist voor bovengenoemde toepassingen en dit vormt een uitdaging voor perovskiet nanokristallen. Bijvoorbeeld in witte LED-lampen bereikt het luminescerende materiaal boven de chip temperaturen van 150-200 °C welke vergelijkbaar is met de temperatuur waarbij de perovskiet nanokristallen gesynthetiseerd worden. Het zal wellicht onmogelijk blijken om een oplossing te vinden voor de stabiliteitsproblemen. De uitdagingen op het gebied van stabiliteit worden (h)erkend en creatieve synthese groepen over de hele wereld hebben inkapselingsmethoden ontwikkeld die de stabiliteit sterk verbeteren maar het is nog lang niet voldoende. De stabiliteit kan de lastigste uitdaging blijken en de verwachting is dat in de komende tien jaar duidelijk zal worden of perovskiet nanokristallen kunnen voldoen aan de hooggespannen verwachtingen die er zijn op diverse toepassingsgebieden.

List of Publications

1. **Kunyuan Xu**, Chun Che Lin, Xiaobin Xie, and Andries Meijerink, Efficient and Stable Luminescence from Mn^{2+} in Core and Core-Isocrystalline Shell CsPbCl_3 Perovskite Nanocrystals, *Chem. Mater.* 2017, 29, 4265-4272.
2. Chun Che Lin, **Kunyuan Xu**, Da Wang and Andries meijerink, Luminescent manganese-doped CsPbCl_3 perovskite quantum dots, *Sci. Rep.*, 2017, 7, 45906
3. **Kunyuan Xu**, Andries Meijerink, Tuning Exciton- Mn^{2+} Energy Transfer in Mixed Halide Perovskite Nanocrystals, *Chem. Mater.*, 2018, 30, 5346-5352.
4. **Kunyuan Xu**, Jara F. Vliem, Andries Meijerink, Long-lived exciton emission in Mn-doped CsPbCl_3 perovskite nanocrystals. *Submitted*

Acknowledgement

First of all, I would like to express my heartfelt and sincere gratitude to my PhD supervisor, Prof. A. Meijerink, for giving me an opportunity to work in your group and introducing me to this exciting research area. I started as an amateur on chemistry of nanocrystals four years ago, it is your wise guidance and kind encouragement made this work possible. Your encyclopaedic knowledge on the optical spectroscopy never ceases to amaze me and motivates me to learn more. I truly appreciate your patience, for giving me time to improve myself. I will miss your great sense of humour after my graduation.

I want to express my appreciation to reading committee of my thesis, Prof. A. P. Philipse, Prof. D. A. M. Vanmaekelbergh, Prof. H. C. Gerritsen, Prof. G. Bacher and Prof. R. J. M. Klein Gebbink for all your careful reviewing of the thesis manuscript and kind suggestions.

This work has not been made in solitude. I am indebted to all the colleagues in CMI group for the nice time we share together: Celso, Ingmar, Anne, Annalisa, Annelies, Maryam, Jette, Naud, Serena, Saoirse, Thomas, Robin, Rouhollah, Elleke, Peter, Federico, Christa, Joep, Christiaan, Tim, Bas, Marlou, Maaïke, Pascal, Wenjin, Dechao, Pierre, Liudmyla, Giuseppe, Markus, Atul Dnyaneshwar and persons not specifically listed.

Finally, I want to thank my family. You are the source of my strength, supporting me through every challenge and giving me a reason to smile.

感谢我的父母，鼓励支持着我做自己喜欢的事。

感谢我的岳父岳母关爱和信任。

特别感谢爷爷奶奶对我的挂念和关心

此外，我想对外公外婆说，对于你们的记忆永远珍藏在我内心最深处。

To my ever-supportive wife, Shi Liu, words fail me to express my profound appreciation for you. You complete me and I am grateful for every day with you.

About the Author

Kunyuan Xu was born in Fushun, China on the ninth of November, 1990. He graduated from high school at Fushun No.2 Senior High School in 2007 and received the Bachelor of Engineering degree in Material Physics in Wuhan University of Technology, China in 2011. In the same year, he started his postgraduate study at the Technical Institute of Physics and Chemistry, Chinese Academy of Sciences in Beijing, China. During his master study, he worked on nitride spectral conversion materials under the supervision of Prof. Jiangtao Li. After receiving the master degree in 2014, he continued his research as a PhD researcher at Utrecht University, The Netherlands under the supervision of Prof. A. Meijerink. His research mainly focused on the optical spectroscopy of manganese-doped perovskite nanocrystals. The main results are presented in this thesis and are published in peer-reviewed journals.